Numerical simulation of mass transfer with and without first order chemical reaction in two-fluid flows

Zur Erlangung des akademischen Grades eines

Doktors der Ingenieurwissenschaften

von der Fakultät für Maschinenbau der Universität Karlsruhe (TH)

genehmigte

Dissertation

von

Dipl. - Ing. Alexandru Aurelian Onea

aus

Bukarest (Rumänien)

Abstract

This work investigates the mass transfer process with and without first order chemical reaction by direct numerical simulation of two-fluid flows within mini-channels. The large potential of two-fluid flows for mass and heat transfer processes, operated in mini- and micro-systems such as micro bubble columns and monolithic catalyst reactors, motivated the present research.

The study is based on the implementation of the species conservation equation in computer code `TURBIT-VoF`. The implementation of the equation is validated against different solutions of simplified mass transfer problems. The demanding treatment of the interfacial concentration jump described by Henry's law is examined with great concern. The diffusive term is successfully compared against one- and two-dimensional theoretical solutions of diffusion problems in two-phase systems. The numerical simulation of mass transfer during the rise of a 4mm air bubble in aqueous glycerol is performed and compared against another numerical simulation in order to test the convective term. The implementation of the source term for homogeneous and heterogeneous chemical reaction is successfully validated against theoretical solutions of mass transfer with chemical reaction in single-phase flows.

The numerical simulations are focused on bubble train-flows flowing co-currently in mini-channels. Taking advantage of the periodic flow conditions exhibited in axial direction, the analysis is restricted to a flow unit cell, which consists of one bubble and one liquid slug. As concerns the hydrodynamics of all simulations performed, good agreement is obtained for the non-dimensional bubble diameter, the ratio of bubble velocity to the total superficial velocity and for the relative velocity in comparison with experimental data. The influence of the unit cell length on mass transfer from the bubble into the liquid phase of an arbitrary species is investigated in square channels having the hydraulic diameter $D_h^\star = 2$mm. Short unit cells are found more effective than long unit cells for mass transfer, in agreement with published investigations performed for circular channels. This is related to the length of the liquid film between bubble and wall which becomes rapidly saturated due to short diffusion lengths and long contact time and leads to a decrease of the local concentration gradient. The major contribution to mass transfer occurs through the cap and the bottom of the bubbles, as reported also in experimental investigations. For mass transfer with heterogeneous chemical reaction more mass is consumed at the wall for systems having long unit cells, as a consequence of the increased lateral surface and more vigorous recirculation in the liquid slug. For species having a large solubility in the continuous phase, diffusion dominates over reaction allowing short unit cells to be more effective for mass transfer with heterogeneous reaction. A formulation of the mass transfer coefficient based on averaged concentrations is proposed for mass transfer processes and successfully compared against another approach based on the mass balance at interface. In complete agreement with experimental and theoretical studies, the study reveals that long liquid slugs and short bubbles are more efficient than short liquid slugs and long bubbles, respectively. The slower saturation of the liquid slug and the more vigorous vortex in the liquid slug exhibited by long liquid slugs and short bubbles are factors for these results. The numerical simulation of mass transfer in rectangular channels having different cross-sections revealed that square channels are more efficient than rectangular channels of the same hydraulic diameter. In rectangular channels the bubbles exhibit ellipsoidal cross-sectional shape and increased surface in close proximity to the wall as compared to square channels. Therefore, for mass transfer processes, the bubbles have large inefficient surface due to fast film saturation, while in case of mass transfer with reaction at the walls this issue constitutes an advantage, since more mass can be transported towards the walls due to short diffusion lengths.

Numerische Simulation von Stoffübertragung mit und ohne chemische Reaktion in Zwei-Fluid-Strömungen

Zusammenfassung

Gegenstand der vorliegenden Arbeit ist die Untersuchung von Stoffübertragungs-vorgängen bei Zwei-Fluid-Strömungen in Minikanälen mit und ohne chemische Reaktion erster Ordnung mittels Direkter Numerischer Simulation. Das Interesse an diesen Untersuchungen ist motiviert durch das große Potenzial, über welches Zwei-Fluid-Strömungen in Mini- und Mikrosystemen, wie z.B. Mikro-Blasensäulen und katalytischen Monolith-Reaktoren, hinsichtlich einer verbesserten Stoff- und Wärmeübertragung im Vergleich zu makroskopischen Systemen verfügen.

Die numerischen Untersuchungen basieren auf der Erweiterung des Rechenprogramms `TURBIT-VoF` um die Erhaltungsgleichung für eine chemische Spezies. Die numerische Implementierung dieser Gleichung wird anhand verschiedener Lösungen für vereinfachte prototypische Stoffübertragungsprobleme validiert. Dabei wird besonderer Wert gelegt auf die numerisch schwierige Behandlung der diskontinuierlichen Konzentrationsverteilung an der Phasengrenzfläche entsprechend dem Henry-Gesetz. Der diffusive Term wird erfolgreich validiert anhand ein- und zweidimensionaler Diffusionsprobleme in Zwei-Fluid-Systemen mit bekannter analytischer Lösung. Zur Validierung der konvektiven Terme wird eine Simulation für den Stoffübergang von einer in wässriger Glyzerin-Lösung aufsteigenden Luftblase durchgeführt und mit anderen numerischen Arbeiten verglichen. Die Implementierung des Quellterms für homogene und heterogene chemische Reaktion wird erfolgreich validiert anhand von analytischen Lösungen für Stoffübertragungsprobleme mit chemischer Reaktion in einphasiger Strömung.

Die Anwendungen des erweiterten Rechenprogramms konzentrieren sich auf die gleich-gerichtete regelmäßige Blasenströmung in Mini-Kanälen. Die Periodizität der Strömung in axialer Richtung erlaubt es, die numerische Simulation auf eine Einheitszelle zu beschränken, die aus einer Blase und einem Flüssigkeitspfropfen besteht. Hinsichtlich der Hydrodynamik wird für alle Simulationen eine gute Übereinstimmung von Blasendurchmesser, Verhältnis von Blasengeschwindigkeit zu Zweiphasen-Leerrohrgeschwindigkeit und relativer Blasengeschwindigkeit mit experimentellen Daten erzielt. Zur Untersuchung des Einflusses der Länge der Einheitszelle auf die Stoffübertragung einer Spezies von der Blase in die Flüssigkeit werden Simulationen in einem quadratischen Kanal mit hydraulischem Durchmesser $D_h^\star = 2\text{mm}$ durchgeführt. Dabei zeigt sich, dass für die Stoffübertragung kurze Einheitszellen effektiver sind als lange. Dieses Ergebnis ist in Übereinstimmung mit ähnlichen Untersuchungen aus der Literatur für kreisförmige Kanäle und steht im Zusammenhang mit der Länge des Flüssigkeitsfilms zwischen Blase und Wand. Aufgrund der kurzen Diffusionslänge und langen Kontaktzeit ist der Flüssigkeitsfilm schnell gesättigt, was einen reduzierten treibenden Konzentrationsgradienten mit sich bringt. Als Zonen, die den Hauptbeitrag zum Stoffübergang liefern, werden die Spitze und das Ende der Blase identifiziert, in Übereinstimmung mit experimentellen Ergebnissen. Für den Fall von Stoffübergang mit heterogener chemischer Reaktion zeigt sich, dass in längeren Einheit-

szellen mehr Spezies an der Wand konsumiert wird als in kürzeren. Dies ist eine Folge des größeren Filmbereichs und der stärkeren Zirkulation im Flüssigkeitspfropfen. Für Spezies mit einer großen Löslichkeit in der Flüssigkeit dominieren diffusive über reaktive Vorgänge und Systeme mit kurzer Einheitszelle erweisen sich als effektiver für Stoffübergang mit heterogener chemische Reaktion. Für den Stoffübergangskoeffizienten wird eine Formulierung eingeführt, die auf den mittleren Konzentrationen in den beiden Phasen basiert, und mit einer Formulierung verglichen, die auf der Massenbilanz an der Grenzfläche basiert. In Übereinstimmung mit experimentellen und theoretischen Untersuchungen zeigt sich, dass längere Flüssigkeitspfropfen und kürzere Blasen effizienter sind als kürzere Flüssigkeitspfropfen und längere Blasen. Dies ist bedingt durch die geringere Sättigung im Flüssigkeitspfropfen und die stärkere Zirkulation im Flüssigkeitspfropfen bei langen Flüssigkeitspfropfen und kurzen Blasen. Die numerische Simulation des Stoffübergangs in rechteckigen Kanälen mit unterschiedlichen Aspekt-Verhältnissen zeigt, dass quadratische Kanäle effektiver sind als nicht-quadratische Rechteckkanäle mit demselben hydraulischen Durchmesser. In rechteckigen Kanälen ist der Blasenquerschnitt ellipsoid und ein größerer Bereich des Umfangs ist näher an der Wand als im quadratischen Kanal. Als Folge dessen ist ein grösserer Bereich der Blasenoberfläche infolge der schnellen Sättigung des entsprechenden Flüssigkeitsfilms relativ ineffizient für den Stofftransport. Für den Fall von Stoffübergang mit heterogener chemischer Reaktion an der Wand stellt dies jedoch einen Vorteil dar, da aufgrund der kurzen Diffusionswege mehr Spezies zur Wand transportiert wird.

Contents

List of Figures

List of Tables

Nomenclature

a	$\left[\frac{\text{m}}{\text{s}}\right]$	Velocity
c	$\left[\frac{\text{mol}}{\text{m}^3}\right]$	Molar concentration
c_p	$\left[\frac{\text{J}}{\text{kg}\times\text{K}}\right]$	Specific heat capacity at constant pressure
d_B	$[\text{m}]$	Bubble diameter
D_{h}	$[\text{m}]$	Hydraulic diameter
D_{AB}	$\left[\frac{\text{m}^2}{\text{s}}\right]$	Molecular diffusion coefficient (diffusivity) of component A in B
$\mathbf{e}$	$[-]$	Unit vector
f	$[-]$	Gas volumetric function
$g, \mathbf{g}$	$\left[\frac{\text{m}}{\text{s}^2}\right]$	Gravitational acceleration
H	$[-]$	Dimensionless Henry's law coefficient
H_{cp}	$\left[\frac{\text{mol}}{\text{m}^3\times\text{Pa}}\right]$	Henry's law coefficient defined via species partial pressure
I	$[-]$	Unit tensor
J	$\left[\frac{\text{m}}{\text{s}}\right]$	Total superficial velocity
$\mathbf{j}_A$	$\left[\frac{\text{mol}}{\text{s}\times\text{m}^2}\right]$	Molar flux relative to the molar average velocity
$k^{(n)}$	$\left[\frac{\text{mol}^{1-n}}{\text{m}^{2-3n}\times\text{s}}\right]$	Constant of the rate of n-th order heterogeneous chemical reaction
	$\left[\frac{\text{mol}^{1-n}}{\text{m}^{3-3n}\times\text{s}}\right]$	Constant of the rate of n-th order homogeneous chemical reaction
k_c	$\left[\frac{\text{m}}{\text{s}}\right]$	Mass transfer coefficient
l, L	$[\text{m}]$	Characteristic length
M	$\left[\frac{\text{kg}}{\text{mol}}\right]$	Molecular weight
n	$[-]$	Number of species contained in a mixture
$\mathbf{n}$	$[-]$	Unit normal vector
N	$[-]$	Number of moles
p_A	$\left[\frac{\text{N}}{\text{m}^2}\right]$	Partial pressure of component A
P	$\left[\frac{\text{N}}{\text{m}^2}\right]$	Total pressure of mixture
r	$\left[\frac{\text{mol}}{\text{s}\times\text{m}^3}\right]$	Rate of chemical mass production inside a control volume
R	$\left[\frac{\text{J}}{\text{mol}\times\text{K}}\right]$	Universal gas constant

s	$\left[\frac{1}{\text{s}}\right]$	Fractional rate of renewal of surface of liquid
t	$[\text{s}]$	Time
T	$[\text{K}]$	Temperature
U	$\left[\frac{\text{m}}{\text{s}}\right]$	Velocity
$\mathbf{v}$	$\left[\frac{\text{m}}{\text{s}}\right]$	Mass-average velocity vector
$\mathbf{v}^0$	$\left[\frac{\text{m}}{\text{s}}\right]$	Volume-average velocity vector
$\mathbf{V}$	$\left[\frac{\text{m}}{\text{s}}\right]$	Molar-average velocity vector
V_A	$\left[\frac{\text{m3}}{\text{kg}}\right]$	Partial specific volume of species A
v_r	$\left[\frac{\text{m}}{\text{s}}\right]$	Relative velocity of the bubble
x_B	$[-]$	Molar fraction of component B in liquid phase
y_A	$[-]$	Molar fraction of component A in gas phase
Z	$[-]$	Non-dimensional relative bubble velocity

Greek notations

α	$[-]$	Species
λ	$\left[\frac{\text{W}}{\text{m}\times\text{K}}\right]$	Heat conductivity
ε	$[-]$	Void fraction
ϵ	$\left[\frac{\text{m2}}{\text{s3}}\right]$	Rate of specific energy dissipation by turbulence per unit mass
μ	$\left[\frac{\text{kg}}{\text{m}\times\text{s}}\right]$	Dynamic viscosity
ν	$\left[\frac{\text{m2}}{\text{s}}\right]$	Kinematic viscosity
ρ	$\left[\frac{\text{kg}}{\text{m3}}\right]$	Total mass concentration (density) of mixture
σ	$\left[\frac{\text{N}}{\text{m}}\right]$	Surface tension
κ	$[\text{m}]$	Interface curvature

Superscripts

$\star$	Dimensional quantity
av	Averaged
m	Mixture

Subscripts

1, 2	Continuous and dispersed phase
B	Bubble
e	Equilibrium
G	Gas phase
Hmg	Homogeneous
Htg	Heterogeneous
i	Index of cell along x axis
	Interface
in	Inlet
j	Index of cell along y axis
k	Index of cell along z axis
	Index of the phase
L	Liquid phase
out	Outlet
ref	Reference
sq	Square
S	Surface
r	Rectangular
UC	Unit cell
x, y, z	Directions of the Cartesian reference system

Non-dimensional numbers

Ca	Capillary number	$\mathrm{Ca} = \frac{\mu_L^\star U_B^\star}{\sigma^\star}$
Da	Damköhler number	$\mathrm{Da} = \frac{k_{\mathrm{Hmg}}^\star l^{\star\,2}}{D^\star}$ $\qquad$ $\mathrm{Da} = \frac{k_{\mathrm{Htg}}^\star l^\star}{D^\star}$
Eö	Eötvös number	$\mathrm{E\ddot{o}} = \frac{\left(\rho_1^\star - \rho_2^\star\right) g\, l^{\star\,2}}{\sigma^\star}$
Eu	Euler number	$\mathrm{Eu} = \frac{|\nabla p^\star|}{\rho^\star\, v^{\star\,2}}$
Fo	Fourier number	$\mathrm{Fo} = \frac{D^\star\, t^\star}{l^{\star\,2}}$
Mo	Morton number	$\mathrm{Mo} = \frac{g^\star\, \Delta\rho^\star\, \mu_L^{\star\,4}}{\rho_L^{\star\,2}\, \sigma^{\star\,3}}$
Pe	Péclet number	$\mathrm{Pe} = \frac{\rho^\star\, c_p^\star\, l^\star\, v^\star}{\lambda^\star}$
Re	Reynolds number	$\mathrm{Re} = \frac{\rho^\star\, v^\star\, l^\star}{\mu^\star}$
Sc	Schmidt number	$\mathrm{Sc} = \frac{\mu^\star}{\rho^\star\, D^\star}$
Sh	Sherwood number	$\mathrm{Sh} = \frac{k_L^\star\, l^\star}{D^\star}$
We	Weber number	$\mathrm{We} = \frac{\rho^\star\, l^\star\, v^{\star\,2}}{\sigma^\star}$

Chapter 1

Introduction

Mass transfer phenomena, defined as the molecular motion of constituents caused by a "driving force", is very often encountered in nature and engineering systems. The most common "driving force" for mass transfer processes is the concentration gradient. Temperature, pressure or any external force gradient can constitute the "driving force" for mass transfer. Accordingly, mass transfer occurs by thermal diffusion, also referred to as Soret effect, pressure diffusion, by differences in the forces created by external fields (e.g. gravity, magnetic or electrical fields) or by Knudsen diffusion. Mass transfer occurs also in all environments that exhibit a chemical reaction. The process of mass transfer occurs mainly through two possibilities:

1. Mass transfer by molecular diffusion, which represents the macroscopic transport of components within a multi-component system in which concentration varies. The source of the molecular diffusion transfer, which occurs by random molecular motion, is the natural tendency to reduce the concentration difference existing within the mixture.

2. Convective mass transfer, which represents the transport of components between a moving fluid and a surface or between two immiscible moving fluids.

The most common equipments used in industry for mass transfer processes are sparged vessels (bubble columns), mechanically agitated vessels, tray towers, wetted-wall, spray and packed towers. Most of these devices share the same goal of achieving large surfaces for the contact between the gas and the liquid. The mass transfer processes to be realized within these units include gas absorption, liquid extraction, adsorption, distillation and condensation [75, 76, 84]

The economical and industrial needs for large production output gave birth to the concept of "scaling-up". This procedure is based on the replacement of the reaction vessel from the laboratory scale to macroscopic dimensions that allow a massive production. Within the last decades, the concept of "numbering-up" has received special attention, due to the promising advantages over the "scaling-up" procedure [29]. A large production obtained by multiple laboratory-scaled devices represents the main task of the "numbering-up" concept.

Fluid flow in small devices differ from those in conventional devices [21]. Surface tension effects, viscosity and diffusion dominate the micro-scale environment, while gravity and inertia are dominating the macro-scale processes. The recent advances reported in the micro-fabrication techniques allowed the production of mini- and micro-devices that exhibit capabilities exceeding those of conventional devices [29, 72]. Therefore, extensive research has been devoted to these micro-fabricated instruments and increased usage has been reported in different fields, ranging from chemistry, biology and electronics to propulsion systems.

Micro-bubble columns and monolithic catalyst flow reactors represent micro-fabricated designs for efficient gas-liquid contacting [29]. Micro-bubble columns exhibit large surface to volume ratio, allowing large transfer rates for heat and mass. Integrating a heat exchanger allows performing highly exothermic reactions, like the fluorination of aromatic compounds. Monolithic catalyst flow reactor present an excellent pressure drop to mass transfer ratio. Chemical reactions can be performed at the wall, taking advantage of the presence of the catalysts. Very often slug flow regime is encountered, as for a micro-bubble column. It is considered that the recirculation within the liquid slug and the very thin liquid film between the bubble and the wall (in which no resistance to mass transfer occurs) are the causes for these large mass transfer rates [36].

Most of the chemical reactions performed within micro-devices take advantage of the increased mass transfer rates and the large interfacial area per unit volume (i.e. 4-5 times larger than in conventional reactor) [40]. As a consequence of the high surface to volume ratio, the heat can be highly efficiently removed from the system, leading to a fast homogenization of the temperature gradients and elimination of the hot spots. The almost isothermal conditions at which the micro-fabricated systems operate allow performing highly exothermic reactions, at increased yield and selectivity, as it is the case of the direct fluorination of toluene [39].

The flow pattern usually encountered in these small devices is laminar. Therefore, investigations based on computational fluid dynamics (CFD) techniques are expected to provide accurate information regarding the flow. On the other hand, in conventional devices, turbulent flow conditions tend to appear, requesting therefore turbulence models, which increase the complexity of the flow simulation.

Another favorable feature of the flow inside micro-devices is its regularity, i.e. internal flow structures repeat themselves. As a consequence, for developed flow that exhibit symmetric conditions in stream-line direction, there is no necessity to consider the flow throughout the entire structure, but one can regard only a small part, defined as unit cell. The flow in all channels of a micro-device, such as a micro-bubble column, is the same. Therefore, the investigation of the flow within one channel provides the entire information needed to characterize the entire system. In this study the concept of unit cell is used to characterize the mass transfer in a narrow single channel.

Micro-reactors systems allow rapid screening of heterogeneously catalysed gas-phase reactions. The small amounts of chemicals that are usually used in micro-systems confer an increased operational safety, since in the case of micro-reactor failure, the accidently released fluids can be easily isolated and neutralized. The effort made in miniaturization

can allow also new reaction mechanisms to be created.

The measurement techniques available have restricted capabilities in exploring the flow within micro-devices. The information provided is limited to the visualization of the dispersed phase, measurement of the axial pressure drop and (mass) flow rate. The microscopic particle image velocimetry μPIV was recently employed to obtain the velocity field within the continuous phase in gas-liquid flows [28]. At Forschungszentrum Karlsruhe, the thermal anemometry method was employed to characterize the flow distribution within micro-reactors [62]. For experimental mass transfer investigations, the laser-induced fluorescence (LIF) was recently developed for visualization of the concentration field near the interface [4, 52, 53, 65, 66]. At the moment no measurement techniques that can provide a complete three-dimensional velocity field of two-fluid flow within micro-channel are available. This issue motivated also the investigation of mass transfer with chemical reaction in two-phase flows by means of a CFD technique.

Within the Institute of Reactor Safety of Forschungszentrum Karlsruhe, where this study has been performed, the computer code `TURBIT-VoF` has been developed for direct numerical simulation (DNS) of laminar and turbulent single-phase flows in channels and pipes [26, 73, 100]. By integrating the volume-of-fluid method to account for the interface tracking, the code was extended to account for DNS of two incompressible and immiscible fluids [68]. Extensive research was focused also on the numerical simulation of heat transfer in bubble train flow within narrow channels [23] and of the investigation of the mechanism governing the liquid turbulence kinetic energy in bubble flows [35].

This study is focused on the investigation of mass transfer in a system containing two incompressible and immiscible fluids separated by an interface. A phase interface is defined by Slattery [79] as a region separating two phases, in which the properties differ from those of the separated phases. It can be regarded as a three-dimensional region having a thickness of several molecular diameters. Both density and concentration are appreciably different in the interface region. The concentration field in two-fluid systems can be discontinuous at interface. Therefore, one of the main challenging tasks regarding the numerical simulation of mass transfer is the handling of the interfacial concentration jump. Another demanding task is the definition of a mass transfer coefficient that has an applicability beyond the context of the employed flow structure.

The presence of the interface in multi-phase or multi-component flows produces important difficulties in the mathematical and physical formulation of the equations. Two classes of methods have been developed to identify the interface for two-phase flows, namely the *two-fluid* approach, discussed by Ishii [38] and the *one-fluid* formulation that employs interface tracking methods (ITM). In the context of the first formulation, each phase occupies at the same time and in a variable proportion the same point. Separate conservation equations are considered for each phase. The method is employed when the shape of the interface is not known or irrelevant to the problem investigated. The interface tracking methods are used when the physical problem requires the precise knowledge of the interface. The volume-of-fluid method, the front tracking and the level set method represent examples of these class that shares the same strategy of interface tracking by means of a phase indicator function [48]. The volume-of-fluid approach relies on the definition of

the volumetric proportion, α, occupied by one of the phases within a volume [32]. The interface is determined for $0 < \alpha < 1$. Line-segment reconstructions schemes are generally employed despite the fact that it can produce interfaces with oscillatory curvature. This drawback can be avoided if curved interface reconstructions are used. The front tracking method uses a set of connected discrete marker points to track the moving boundary [85]. The level set approach is based on the construction of a function, defined everywhere in the computational domain, which refers to the shortest distance to the interface [56, 74]. The exact position of the interface corresponds to the null value of this function. The approach can be easily extended to three dimensions and unstructured grids. The formulation drawbacks are interface smearing and non-conservation of mass. The interface tracking methods use a single set of conservation equations obtained after a volume averaging procedure and account for the interface motion by means of an transport equation of the phase indicator function.

Although in the last decade important progress has been made in numerical investigations of mass transfer, the process of mass transfer accompanied by chemical reactions has not received so much attention. Therefore, within the present work, the mass transfer process is optionally accompanied by first order chemical reactions. Both homogeneous and heterogeneous chemical reactions have been considered. In case of a homogeneous chemical reaction both reactants have the same phase, while in case of a heterogeneous reaction the reactants have different phases. The homogeneous reactions considered in this paper occur only in the liquid slug, while the heterogeneous reactions occur at the walls.

The increasing interest in the investigation of mini-devices that have large potential advantages over conventional devices and the importance of developing further the computer code `TURBIT-VoF` motivated this research. The main goals of the study are:

1. Extension of the computer code `TURBIT-VoF` to allow for the simulation of two-fluid flows with interfacial mass transfer accompanied by first order homogeneous and heterogeneous chemical reaction

2. Validation of the numerical implementation of the species conservation equation against solutions published in literature

3. Investigation of the mass transfer mechanism with an increased interest in the region close to the interface and in enclosed systems having a small characteristic length

4. Identification of strategies to optimize the mass transfer process in bubble train flows within state-of-the art mini- and micro-reactors

The present study is organized as follows.

The second chapter presents the mathematical description of the mass transfer process. In this context, the species conservation equation, Henry's law and the adequate relations valid at interface are presented. The most important contributions concerning mass transfer studies are further reviewed.

Chapter 3 deals with the numerical implementation of the species conservation equation in the computer code `TURBIT-VoF`. Firstly, the volume averaging of the non-dimensional

species conservation equation is outlined. This mathematical procedure couples the species conservation equations of both phases. In this way the equations once valid only in one phase will be employed further as one equation that is valid throughout the entire two-phase system. Secondly, the discretization of each term from the species conservation equation is in great detail discussed.

The validation of the numerical method is represented in chapter 4. The diffusive term in the species conservation equation is validated against one-dimensional and two-dimensional analytical solutions of unsteady mass transfer. An overall mass transfer coefficient is proposed to quantify the mass transfer in enclosed systems. The implementation of the convective and diffusive terms is compared against steady-state analytical solution of mass transfer in single phase flow and against another numerical simulation of mass transfer from a single bubble rising in a stagnant fluid. The implementation of the source term is validated against steady-state analytical solutions of mass transport with homogeneous and heterogeneous first order chemical reaction in single phase flow.

In chapter 5 are discussed the numerical simulations of mass transfer with and without first order chemical reaction that have been performed. The interest is focused on the influence of the unit cell length, liquid slug length and bubble length on the mass transfer process. Mass transfer in channels having square and rectangular cross-sections is also investigated.

The conclusions are presented in chapter 6.

Chapter 2

Physics and mathematical description of mass transfer processes in two-fluid flows

This chapter presents the mathematical description of the mass transfer process. The chapter is organized as follows. Section 2.1 outlines the species conservation equation which describes the mass transfer process. The interfacial conditions, Henry's law and the boundary conditions are presented also within this section. An overview of the current studies of mass transfer problems is made in section 2.2.

2.1 Local equations

2.1.1 Species conservation equation

Let us consider two isothermal, incompressible fluids having different phases. The fluids flow with different velocities $\mathbf{v}_k(\mathbf{x}, t)$ and occupy separate domains Ω_k, where

$$k = \begin{cases} 1, & \text{for the liquid phase} \\ 2, & \text{for the gas phase} \end{cases} \tag{2.1}$$

The species conservation equation for species α and phase k, describing unsteady mass transfer by convection, diffusion and chemical reaction, is defined in conservation form as follows [6]:

$$\frac{\partial c_k^{\alpha \star}}{\partial t^\star} + \nabla^\star \cdot (c_k^{\alpha \star} \mathbf{v}_k^{\alpha \star}) = -\nabla^\star \cdot \mathbf{j}_k^{\alpha \star} + r_k^{\alpha \star}, \tag{2.2}$$

where superscript $\star$ designates a dimensional quantity and $\mathrm{r}_k^{\alpha \star}$ represents the reaction rate for a homogeneous chemical reaction. If the species α will be created by reaction, the source term will be positive. The reaction rate represents the amount of moles of species α that are produced/consumed due to the reaction in the entire flow volume and in time:

$$r_k^{\alpha \star} = \frac{1}{V^\star} \frac{\mathrm{d}N_i}{\mathrm{d}t^\star} = \frac{\text{No. moles}}{\text{Volume of fluid} \times \text{Time}} \tag{2.3}$$

For a first order chemical reaction, the source term is expressed as:

$$r_k^{\alpha\star} = k_k^{(1)\alpha\star} c_k^{\alpha\star}, \tag{2.4}$$

where $k^{(1)\alpha\star}$ represents the constant of the first order homogeneous chemical reaction.

The molar diffusive flux expressed by Fick's law relative to the molar average velocity and for isothermal and isobaric conditions is:

$$\mathbf{j}_k^{\alpha\star} = -D_k^{\alpha\star}\nabla^\star c_k^{\alpha\star}, \tag{2.5}$$

where $\nabla^\star c_k^{\alpha\star}$ represents the driving force, i.e. the difference between the concentration of species at two different space positions as long as equilibrium is not reached throughout the system. The diffusion coefficient $D_k^{\alpha\star}$ is in general a function of pressure, temperature and composition [6]. The diffusivity in liquids is several orders of magnitude smaller than diffusion coefficients in gases, as a result of smaller mean free path [51, 91]. Treybal [83, 84] considers that the true "driving force" of diffusion is not concentration, but rather the activity. Nevertheless, the concentration field is usually employed to define the molar diffusive flux.

A more general relation for the diffusive flux, not restricted to isothermal and isobaric conditions, is proposed by de Groot [15]:

$$\mathbf{j}_k^{\alpha\star} = -c_k^\star D_k^{\alpha\star}\nabla^\star x_k^\alpha, \tag{2.6}$$

where $x_k^\alpha = c_k^{\alpha\star}/c_k^\star$ represents the phase mole fraction for gases and $c_k^\star = \sum_{\alpha=1}^n c_k^{\alpha\star}$ represents the concentration of all species within phase k.

The phase molar average velocity for a n-component mixture, which is contained in the convective term, is defined as follows:

$$\mathbf{v}_k^\star = \frac{\sum_{\alpha=1}^n c_k^{\alpha\star}\mathbf{v}_k^{\alpha\star}}{c_k^\star} \tag{2.7}$$

where $\mathbf{v}_k^{\alpha\star}$ is the absolute velocity of species α relative to stationary coordinate axes.

2.1.2 Henry's law

Mass transfer is caused by the departure from the equilibrium state of the concentration profile throughout the phases. The classical mass transfer theory considers that, at equilibrium, the concentrations at the interface between phases may not be equal [76, 84].

Local equilibrium is assumed to be instantaneously established at interface [71]. For dilute concentrations of many fluids the equilibrium relationship at interface is given by Henry's law, which relates the partial pressure of a species α in the gas phase 2, under

equilibrium conditions, to the concentration of the dissolved species in the liquid solvent 1 [60]:

$$p_2^{\alpha \star} = H_{cp}^{\alpha \star} c_1^{\alpha \star}, \tag{2.8}$$

In this work Henry number has been considered as the dimensionless ratio between concentration of species α in the liquid phase and in the gas phase:

$$c_{1i}^{\alpha \star} = H^{\alpha} c_{2i}^{\alpha \star}, \tag{2.9}$$

where subscript i is used to identify the quantities at interface. Defined in this way Henry number H^{α} represents the solubility of species α.

Henry's law is valid if species α is weakly soluble in the liquid phase. The criteria for determining such a system is proportional to the molality of the system and the species molar mass. If the chemical species reacts at the interface, one cannot apply Henry's law to the total concentration of the species, but only to that amount of species that did not react [12].

Henry number is temperature dependent and pressure dependent (for $P > 20$atm). Nevertheless, since the flows simulated are assumed isothermal and have a small pressure gradient, Henry number is considered constant.

A review of the different formulations used for Henry's law is given by Sander [69], who presents also data for the Henry number of different species relative to water.
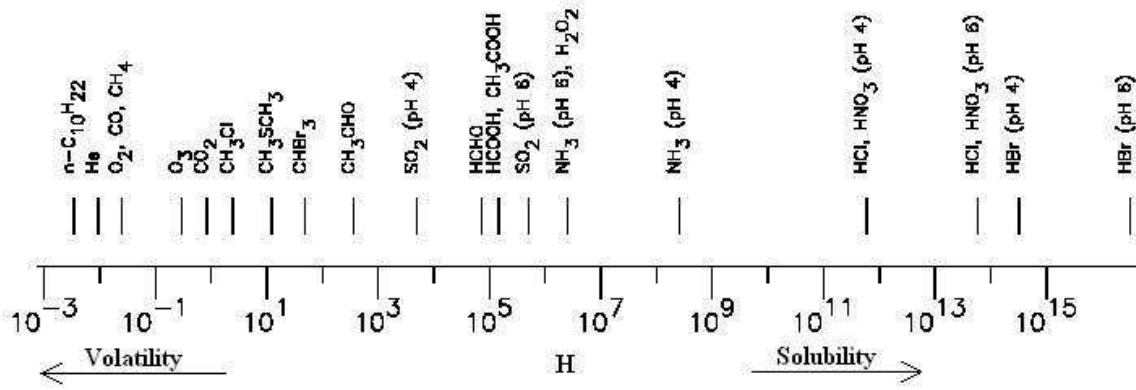
Figure 2.1: Range of Henry number for different species relative to water [69]

2.1.3 Interfacial conditions

The interfacial species balance can be written as follows [79, 97]:

$$\frac{\partial c_S^{\alpha \star}}{\partial t^\star} + \nabla_S^\star \cdot (c_S^{\alpha \star} \mathbf{v}_S^{\alpha \star}) + c_S^{\alpha \star} (\nabla_S^\star \cdot \mathbf{n}_1)(\mathbf{v}_i^\star \cdot \mathbf{n}_1) = \\ [\mathbf{j}_{1i}^{\alpha \star} + c_{1i}^{\alpha \star}(\mathbf{v}_{1i}^{\alpha \star} - \mathbf{v}_i^\star)] \cdot \mathbf{n}_1 + [\mathbf{j}_{2i}^{\alpha \star} + c_{2i}^{\alpha \star}(\mathbf{v}_{2i}^{\alpha \star} - \mathbf{v}_i^\star)] \cdot \mathbf{n}_2 + r_i^{\alpha \star}, \tag{2.10}$$

where $c_S^{\alpha\star}$ represents the concentration at the surface, having units of moles per unit area. The first term in the left hand side represents the species accumulation at the interface. The second term represents the species surface transport, where $\mathbf{v}_S^{\alpha\star}$ is the surface velocity vector of species α [54, 79]:

$$\mathbf{v}_S^{\alpha\star} = \mathbf{P} \cdot \mathbf{v}^{\alpha\star}, \tag{2.11}$$

and $\mathbf{P}$ is the projection tensor and $\mathbf{I}$ is the unit tensor:

$$\mathbf{P} = \mathbf{I} - \mathbf{n}_1 \, \mathbf{n}_1 \tag{2.12}$$

The third term in equation (2.10) denotes the rate of change of surface area per unit volume, where the surface gradient operator is defined as in [54]:

$$\nabla_S^\star = \mathbf{P} \cdot \nabla^\star \tag{2.13}$$

and $\mathbf{v}_i^\star \cdot \mathbf{n}_1$ represents the velocity of displacement of the surface. The first and the second term in the right hand side of equation (2.10) represent the species convective and diffusive fluxes across the interface. The unit vector $\mathbf{n}_1$ is directed toward phase 1, while the unit vector $\mathbf{n}_2$ is directed toward phase 2. The source term $r_i^{\alpha\star}$ is attributable to a heterogeneous chemical reaction.

Taking in consideration the possibilities of the `TURBIT-VoF` computer code and the tasks of the present work the following assumptions are made at the interface:

1. The species can not accumulate

2. The mass transfer does not affect the volume of the bubble

3. No chemical reaction occurs

4. The surface transport is neglected

5. No phase change occurs

Based on these assumptions, the species balance at interface (2.10) becomes:

$$\left[\mathbf{j}_{1i}^{\alpha\star} + c_{1i}^{\alpha\star}(\mathbf{v}_{1i}^{\alpha\star} - \mathbf{v}_i^\star)\right] \cdot \mathbf{n} = \left[\mathbf{j}_{2i}^{\alpha\star} + c_{2i}^{\alpha\star}(\mathbf{v}_{2i}^{\alpha\star} - \mathbf{v}_i^\star)\right] \cdot \mathbf{n}, \tag{2.14}$$

where $\mathbf{n}$ represents the unit normal vector at interface pointing in phase 1 ($\mathbf{n} = \mathbf{n}_1 = -\mathbf{n}_2$).

Since phase change is not considered, the kinematic condition relating the interfacial velocity to the phase velocities is given by [38]:

$$\mathbf{v}_{1i}^{\alpha\star} = \mathbf{v}_{2i}^{\alpha\star} = \mathbf{v}_i^\star \tag{2.15}$$

At the interface, the physical concentration field can be discontinuous, as displayed in Figure 2.2. This interfacial concentration discontinuity is difficult to handle from the computational point of view. In order to avoid the numerical difficulties associated to the
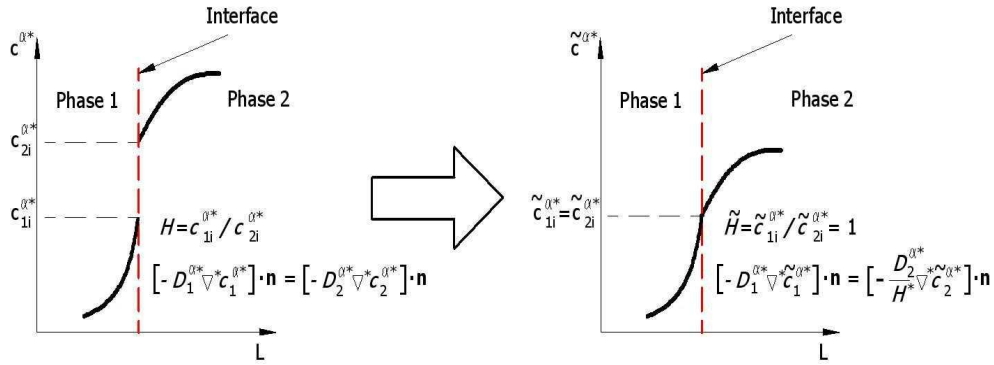
Figure 2.2: Transformation of the discontinuous interfacial concentration field

concentration jump, the concentration field is transformed to ensure continuity at interface. Inserting the definition:

$$\tilde{c}^{\alpha\star} = \begin{cases} c_1^{\alpha\star}, & \text{for the liquid phase} \\ H^{\alpha} c_2^{\alpha\star}, & \text{for the gas phase} \end{cases} \tag{2.16}$$

will provide the advantage of continuous concentrations at the interface, as presented in Figure 2.2:

$$\tilde{c}_{1i}^{\alpha\star} = \tilde{c}_{2i}^{\alpha\star} \tag{2.17}$$

Such a transformation of the concentration field has recently become popular in the numerical simulations of interphase mass transfer [8, 14, 61, 105]. The choice of the transformed phase, i.e. in the present study only the gas phase, is arbitrary [105].

As a consequence of the concentration field transformation, the interfacial jump of the species concentration is transformed to a normal derivative jump. The continuity of the normal molar diffusive fluxes at interface (2.14) can be expressed as follows:

$$\tilde{\mathbf{j}}_{1i}^{\alpha\star} \cdot \mathbf{n} = \frac{1}{H^{\alpha}} \tilde{\mathbf{j}}_{2i}^{\alpha\star} \cdot \mathbf{n} \quad \rightarrow \quad [-D_1^{\alpha\star}\nabla^{\star}\tilde{c}_1^{\alpha\star}]_i \cdot \mathbf{n} = \left[-\frac{D_2^{\alpha\star}}{H^{\alpha}}\nabla^{\star}\tilde{c}_2^{\alpha\star}\right]_i \cdot \mathbf{n} \tag{2.18}$$

2.1.4 Boundary conditions

Dirichlet and Neumann boundary conditions can be specified at the walls:

Boundary condition	Mathematical formulation
Dirichlet	$c_{1w}^{\alpha\star} = \text{ct.}$
Neumann	$D_{1w}^{\alpha\star}\nabla^{\star}c_{1w}^{\alpha\star} \cdot \mathbf{n}_{1w} = \text{ct.}$

Table 2.1: Boundary conditions at the walls

In case of species consumption at the wall by first order heterogeneous chemical reaction, the boundary condition becomes:

$$D_{1w}^{\alpha\star}\nabla^{\star}c_{1w}^{\alpha\star} \cdot \mathbf{n}_{1w} = k_1^{(1)\,\alpha\star}c_1^{\alpha\star}, \qquad (2.19)$$

where $k_1^{(1)\,\alpha\star}$ represents the constant of the first order reaction.

2.2 Literature review of mass transfer processes in two-phase flows

Several models have been proposed during the last century to describe the interfacial mass transfer. The analysis of absorption process was firstly described by the two-resistance theory proposed by Whitman [98]. Two hypothetical layers of constant thickness are assumed to exist on each side of the interface. The model considers that the entire resistance to diffusion occurs within these films. The rate of absorption is determined by two driving potentials. The "driving force" for the gas film is proportional to the difference between the partial pressure of the solute inside the bulk gas phase and the partial pressure of solute inside the film, which is in equilibrium with the liquid. The "driving force" for the liquid film is proportional to the difference between the concentration inside the liquid film, in equilibrium with the gas phase, and the concentration in the bulk liquid. Higbie [30] proposed later the penetration theory for mass transfer. The model considers that the time of exposure of the fluid to the dispersed phase is short, so that the steady-state concentration gradient, characteristic of the two-resistance theory, has no time to develop. Therefore, at interface, mass is considered to be transferred by unsteady state molecular transport at a constant time of exposure. The latter model was extended by Danckwerts [13], who considered that the elements situated at interface have different exposure-time histories. Surface age distribution functions were proposed to predict the random time of exposure of an element situated at interface until it is replaced by fresh elements arising from the bulk liquid.

2.2.1 Theoretical solutions for mass transfer studies

Due to difficulties in analytical solution of complete two-phase flow equations, the theoretical investigation of mass transfer has been limited to creeping and potential flow and simplified geometries.

Several analytical solutions have been developed for the mass transfer problem from circulating drops in continuous fluid.

Ruckenstein [67] used boundary-layer simplifications to solve the differential equation of the concentration field. The study is based on the assumption that variations in the local concentrations are restricted to the immediate vicinity of the interface. The results obtained are restricted to large values of the parameter ReSc and to short times. The

study was later extended to intermediate Reynolds number, i.e. $10 \leq \text{Re} \leq 250$, by Uribe-Ramírez and Korchinsky [86]. The Galerkin method was used to obtain the velocity field, while the diffusion equation was solved based on the similarity transformation method.

Kronig and Brink [47] derived a theoretical solution to determine the mass transfer from circulating droplets, based on the flow pattern encountered in the creeping flow regime. The resistance to mass transfer was considered in the dispersed phase only. The results obtained are useful for long time processes.

Mass transfer between drops and gases is qualitatively similar to the case when the continuous phase is a liquid. Increased mass transfer is achieved in the gas due to the high diffusivity. In the dispersed phase, the circulation is strongly reduced as a consequence of the large viscosity ratio. Therefore, the mass recirculation within the drop decreases.

The mass transfer between a fluid and a solid sphere has been analyzed by Levich [49] under the assumption of creeping flow. The same author solves the problem of mass transfer from a spherical bubble in potential flow and the problem of mass transfer during the free rise of moderate size bubbles in liquids with and without surfactants. The mass flux in the latter study is reported to be direct proportional to the square root of the diffusivity and terminal velocity and inverse proportional to the square root of the diameter of the bubble. The surface-active agents tend to rigid the interface and decrease the internal circulation leading to a sharp decrease of the mass transfer.

Elperin and Fominykh [18] investigated theoretically the mass transfer at the trailing edge of a modelled gas slug for small and large Reynolds numbers. It is reported that the coefficient of mass transfer at the trailing edge, leading edge and at the cylindrical part of the gas slug have the the same order of magnitude. The contribution of the bottom part of the bubble to the total mass flux is found significant for short bubbles ($L_B^\star / L_x^\star \simeq 1.5 \div 3$) and negligible small for large bubbles ($L_B^\star / L_x^\star \geq 10$), where $L_x^\star$ represents the width of the channel. The same authors developed a theoretical model for absorption in Taylor flow with small bubbles in liquid plugs [19]. It is reported that the mass flux decreases with increasing number of the unit cells. The volumetric mass transfer coefficient $k_L^\star a^\star$ is found direct proportional to the gas and liquid superficial velocities, as predicted also by Berčič and Pintar [5]. An interesting observation is that the contribution of the small spherical bubbles in the liquid slug is considerable higher than the contribution of the Taylor bubble.

2.2.2 Experimental investigations of mass transfer

Investigation of mass transfer in two-phase system has been recently performed by means of laser-induced fluorescence (LIF) technique. Since this optical technique is non-intrusive, it presents the advantage of not disturbing mechanically the process investigated.

Significant progress has been reported by Roy and Duke [65, 66], who employed LIF for visualization of two-dimensional dissolved oxygen concentration field in water. The measurements are restricted to the area close to the bubble surface and refer only to half of the bubble. A significant variation in the concentration boundary layer thickness is found. The upper portion of the bubble presents thin boundary layer and high concentration gradients. From the middle to the lower part of the bubble, the contour lines for

concentration are spaced more widely, showing an increasing boundary thickness which correspond to a decrease in the local concentration gradient.

Mühlfriedel and Baumann [4, 52] reported concentration measurements during mass transfer of a fluorescent dye (rhodamine B) across an interface between two partial immiscible stagnant liquids (1-butanol and water), by means of LIF technique. It has been observed that no equilibrium concentration of the tracer occurs at interface, as the classical theory of mass transfer predicts. A concentration gradient is formed at the phase boundary, which acts against the mass transfer direction. It is considered that this gradient is caused by the different solubility of the transferred species in the two phases.

Recently, Hotokezaka et al. [34] investigated the extraction of uranium ions from nitric acid aqueous solution into aqueous tri-buthylphosphate solutions within a micro-channel by means of thermal lens microscopy (TLM). It is considered that the method provides some advantages for investigation of extraction at micro-scale. The most important advantages are considered to be the high-sensitivity, the wide dynamic range and the possibility of *in-situ* analysis within microscopic range by focusing irradiation of laser beam. Compared to conventional techniques, increased extraction efficiency, reduced amount of waste solutions and increased selectivity are reported.

2.2.3   Numerical simulations of mass transfer in two-phase flows

Numerical simulations of mass transfer can be investigated in two separate ways. The first approach considers the numerical computation of the species conservation equation. The flow field is generated by solving the Navier-Stokes equations. The interface motion is taken into account by means of an interface "tracking" or "capturing" method [70].

The second approach considers the development of a model which quantifies the mass transfer by means of a certain mass transfer coefficient. Usually several assumptions for the flow conditions and for the geometry configurations are made restricting the applicability of the models to idealized flows.

Both approaches have their own advantages and disadvantage. Probably the most important aspect of the first method is that it can be applied to any geometrical configuration and flow type, while the second approach is restricted to particular geometrical configurations and limited flow conditions. A disadvantage of the numerical computation of the species conservation equation is the relatively high computational time. In order to solve the species conservation equation, firstly one has to solve the discretized Navier-Stokes equations, and secondly to evaluate the interface motion by means of an interface "tracking" or "capturing" method. Therefore, another disadvantage of the first method is represented by the actual limitations in resolving the Navier-Stokes equations, especially for the turbulent regime. Demanding requirements for the computational mesh must be fulfilled when the concentration boundary layer is much smaller than the viscous boundary layer. This is the case for mass transfer problems having large values of the Schmidt number Sc or of the Reynolds and Schmidt number product ReSc. Mass transfer of very soluble species within the solvent, for which Henry number H has a large value, requires also a refined grid to capture the thin concentration boundary layer that develops on both

sides of the interface.

To the author's knowledge, the first numerical simulation of mass transfer coupled with the volume-of-fluid method to track the interface was presented by Ohta and Suzuki [55]. It is reported that the mass transfer depends significantly on the physical properties of the phases and that the formation of the concentration field is strongly connected to the fluid flow field. The study investigates the mass transfer of an arbitrary species for small variations in the ratio of the diffusivities and it is restricted to the simplest case of continuous interfacial concentration field, i.e. $H = 1$.

Due to the discretization of the diffusive term, the diffusivity needs to be calculated at the cell face. For cells containing only one phase the cell face diffusivity is the diffusivity of that phase. For evaluating numerically the diffusivity in cells containing the interface several formulations are found in literature, as presented in Table 2.2. The arithmetic mean of the phase diffusivities is rarely used due to its inability to handle the discontinuity of the diffusion coefficient [59]. The most used formulation for evaluation of the cell face diffusivity is the method proposed by Patankar [59]. It was developed for one-dimensional heat/mass transfer problems, assuming that the transferred quantity is continuous at interface and that the heat/mass interfacial fluxes are equal. Davidson and Rudman [14] proposed also a cell face diffusivity formulation, which is based on the same assumptions as Patankar's approach. These two formulations were implemented in `TURBIT-VoF`, after taking into account the interfacial concentration jump. A detailed discussion of the cell face diffusivity implementation is given in section 3.5. Recently, two new formulations for the cell diffusivity were proposed by Liu and Ma [50] and Voller and Swaminathan [89, 90]. Both of them are based on the dependency of the diffusivity on the concentration field. Improved accuracy and effectiveness in comparison with the harmonic mean formulated by Patankar is reported. These methods were not implemented in `TURBIT-VoF` since the diffusivity was not considered to be concentration dependent.

Method	Cell face diffusivity
Arithmetic mean	$D_{k+1/2} = D_k + (D_{k+1} - D_k) \dfrac{z_{k+1/2} - z_k}{z_{k+1} - z_k}$
Patankar [59]	$D_{k+1/2} = \dfrac{2D_{k+1}D_k}{D_k + D_{k+1}}$
Davidson & Rudman [14]	$D_{k+1/2} = \dfrac{D_{k+1}D_k}{D_k(1.5 - \lambda) + D_{k+1}(\lambda - 0.5)}$
Liu & Ma [50]	$D_{k+1/2} = D(c_{k+1/2})$
Voller & Swaminathan [90, 89]	$D_{k+1/2} = \dfrac{1}{c_{k+1} - c_k} \displaystyle\int_{c_k}^{c_{k+1}} D(c)dc$

Table 2.2: Methods for evaluating the diffusivity at cell face

The concentration field can be discontinuous at the interface. Based on the largely

used assumption of instantaneous established interfacial equilibrium, the interfacial jump is described by means of Henry's law [8, 45]. Petera and Weatherley [61] and Bothe et al. [8] used a similar transformation of the concentration field, that ensures the continuity of the concentration at interface. Two arguments fundament the choice of such a concentration field transformation. The first one is the avoidance of the inherent numerical difficulties in handling the interfacial concentration jump. The second one is the need to fulfil the assumption of a continuous field, in order to correctly employ the formulas for the cell face diffusivity proposed by Patankar [59] and Davidson and Rudman [14].

Petera and Weatherley [61] compared successfully the numerical solution of ethanol extraction from ethanol-water mixture into n-decanol solution against experimental results. It was found that the internal circulation within the drop, the development of a recirculation zone in the suspending liquid and the increased surface area as a result of droplet deformation are the key factors that control the mass transfer process. The concentration wake developed presents the same characteristics of smoothness, symmetry and regularity also reported by Bothe et al. [8] and Koynov et al. [45] for bubble Reynolds number ranging between 8 and 30.

Adekojo et al. [1] studied unsteady-state mass transfer of a suspended liquid droplet in a continuous phase, for a conjugate problem. The simulation was limited to Re $\leq$ 20 since the effect of free convection is significant only in this regime. A Boussinesq-approximation was used to account for the change in density due to concentration changes as:

$$\rho = \rho_\infty - \rho_\infty \beta_k (c - c_\infty), \tag{2.20}$$

where β_k is the mass expansion coefficient. It is reported that free convection enhances mass transfer over pure diffusion and mass transfer by forced convection is greater than by the combined free and forced convection for a rising drop.

For industrial systems such as a bubble column that contains a large number of bubbles the exact tracking and measuring of each bubble interface is impossible. Therefore, for mass transfer studies the employment of a mass transfer coefficient $k_L^\star$ is found irrelevant. Mass transfer is quantified by means of a volumetric mass transfer coefficient, $k_L^\star a^\star$, which is more convenient to be estimated. Irandoust and Andersson [36], Kreutzer et al. [46] and van Baten and Krishna [87] considered the separate contributions of the hemispherical caps and lateral sides of Taylor bubbles on mass transfer in order to define a volumetric mass transfer coefficient. The models proposed indicate a dependence of the volumetric mass transfer coefficient on the channel diameter. It is interesting to notice that Berčič and Pintar [5] proposed an empirical correlation of the volumetric mass transfer coefficient, which is independent of the channel diameter.

Paschedag et al. [58] and Yang and Mao [105] derived a mass transfer coefficient in which the concentration gradient was formed using the concentration in the bulk phase and the mean concentration in the dispersed phase. Another formulation of the mass transfer coefficient that was proposed by Paschedag et al. [57] was based on a concentration gradient formed with the concentration at the interface and a mean concentration in the dispersed phase. When considering mass transfer in enclosed mini-systems, the definition of the

concentration in the bulk phase proves to be a difficult task as a consequence of the reduced characteristic length scale. Similar, the employment of the concentration at the interface in the definition of a mass transfer coefficient in enclosed systems represent an arduous task attributable to the three-dimensional character of the interface. A new definition of the concentration gradient contained in the mass transfer coefficient is proposed and discussed in section 4.2.

Van Baten and Krishna [87, 88] developed a model for the mass transfer simulation in Taylor flows. The contributions of the cap, bottom and lateral side of the bubble were considered separately. The influence of the unit cell length, bubble rise velocity, film thickness and length and liquid diffusivity on mass transfer were investigated. The model is based on an ideal Taylor bubble, held at constant concentration. As a consequence of the ideal model, the thickness of the liquid film and the velocity field is independent of the unit cell length.

2.2.4   Investigations of mass transfer with chemical reactions

Juncu [43] extended his study, [42], regarding the influence of the Henry number on the conjugate isothermal mass transfer from a sphere, by taking into account a first order chemical reaction occurring either in the continuous phase or in the dispersed phase. It is considered that the system of equations used to model the process depends on four dimensionless parameters: Damköhler number Da, Henry number H, Péclet number Pe and diffusivity ratio, $D_G^\star/D_L^\star$.

For the chemical reaction occurring in the continuous phase, the Damköhler number was varied so that slow (Da = 1), intermediate (Da = 100) and fast (Da = 1000) chemical reaction should be modelled. For all three cases the overall asymptotic Sherwood number increases with increasing Henry number if $D_G^\star/D_L^\star < 1$, and decreases with increasing Henry number if $D_G^\star/D_L^\star \geq 1$. Keeping constant the Henry number and the diffusivity ratio, the Sherwood number increases with increasing Damköhler number.

Irandoust and Andersson [36, 37] investigated the mass transfer with heterogeneous chemical reaction in Taylor flow operated in a monolithic catalyst reactor. The high performance of the reactor was reported to be caused by the following reasons. The gas-liquid and the liquid-solid phases exhibit a large interfacial area per unit volume that enhances the mass transfer. The liquid film that separates the bubble from the wall provides a short diffusion length which results in a small transfer resistance. The recirculation within the liquid slug provided fresh amounts of species at the wall, increasing therefore the effectiveness of the reaction in the region of the liquid slug.

The influence of the bubble length for fixed liquid slug length and the influence of the liquid slug length for constant bubble length on mass transfer with chemical reaction has been studied by Berčič and Pintar [5] in capillaries of circular cross-section. It is found that the most important parameters for the determination of mass transfer in Taylor flow regime are the average unit cell velocity and the liquid slug length. It is reported that the major part of mass transfer between the gas and the liquid occurs through the spherical-ended surfaces exposed to the liquid slugs. The major part of the reaction is performed

on the surface of the catalytic wall that is covered by the liquid slug. The volumetric liquid-solid mass transfer coefficient is found to be inverse proportional to the length of the unit cell length. A drawback of the proposed model for the volumetric mass transfer coefficient is the fact that the influence of the diffusivity ratio and of the solubility of the solute on the correlation is not known since they were not varied in the experiment.

Numerical simulations of mass transfer with homogeneous chemical reaction for an arbitrary species are reported recently by Koynov et al. [45]. The conservation equations are computed using a 2D fixed uniform grid, while the interface is tracked using a 1D deformable and moving grid. The species concentration in the gas phase is kept constant at the equilibrium value of $c_g = P^\star/H^\star_{cp}$, where $P^\star$ designates the pressure and $H^\star_{cp}$ the Henry's constant. The simulations are performed at two values of the bubble Reynolds number, i.e. $\text{Re}_B = 8$ and $\text{Re}_B = 68$. For small Re_B, the dissolved gas is contained entirely in a closed concentration wake, similar qualitatively in shape with the one obtained by Bothe et al. [8] and with `TURBIT-VoF`, as described in section 4.3.2. At larger Re_B, a vortex-shedding regime is observed. Vortices are forming alternately on each side of bubble bottom and while growing and drifting away they transport entrapped dissolved gas down the wake. The transition from to the vortex-shedding regime is considered to occur at Reynolds number between 30 and 50 and is found dependable also on Morton and Weber numbers. It is found that the selectivity is continuously decreasing in time in case of a single rising bubble. A larger selectivity is obtained for small Re_B, due to the slow transport of reactant in the concentration wake, leading to a limited production of by-product. For larger Re_B, the rapid disperse of the gas by vortex motion leads to enhanced rate of by-product formation.

Chapter 3

Numerical implementation of the species conservation equation in computer code `TURBIT-VoF`

This chapter describes the numerical implementation of the species conservation equation in computer code `TURBIT-VoF`. The chapter is organized as follows. In section 3.1 the computer code `TURBIT-VoF` is briefly presented. In section 3.2 the species conservation equation is considered in a non-dimensional form. The volume averaging of the species conservation equations is presented in section 3.3. The main problem encountered by the finite volume methods is the evaluation of the numerical flux at a cell face. One can compute the numeric flux at a cell face in a *centered* or *upwind* way [17]. The discretization of each term from the volume averaged species conservation equation is further described in sections 3.4, 3.5 and 3.6. For the time integration, an explicit TVD Runge-Kutta third order scheme is employed, the same used for the time integration of the momentum [68] and energy equations [23]. The determination of the maximal time step is presented in section 3.7. Last section focuses on the implementation of the boundary conditions.

3.1   `TURBIT-VoF` computer code

The computer code TURBIT has been developed at the Institute of Reactor Safety, within the Research Center Karlsruhe, for direct numerical simulations (DNS) of laminar and turbulent single-phase flows in channels and pipes [26, 73, 100]. The code was later largely extended by Sabisch [68] to account for the DNS of bubbly flows in plane channels. A volume-of-fluid method was used to account for the interface tracking leading to the new `TURBIT-VoF` designation. Further extensions allowed the simulation of heat transfer process in slug flow within small channels with rectangular cross-section [23] and the determination of the liquid turbulence kinetic energy in bubble-driven liquid flows [35].

The `TURBIT-VoF` code considers the mass, momentum and energy equations for two incompressible immiscible Newtonian fluids. The volume averaged single-field formulation

of the mass and momentum equations were derived by Sabisch [68] and Wörner et al. [104], while the derivation of the volume averaged energy equation was performed by Ghidersa [23]. For two-phase flows with high bubble Reynolds number, a refined grid is needed to resolve the viscous boundary layer and to obtain a null drift velocity necessary for the local equations employed in volume-of-fluid methods. Employing such a refined grid is not always practical due to large computational costs and large complexity of the interface reconstruction. Therefore, a local volume averaging procedure[1] that uses a model for the relative velocity v_r between the phases is performed, allowing a reasonable grid resolution [104].

The non-dimensional single-field volume averaged system of equations considered in TURBIT-VoF is:

Mass conservation

$$\nabla \cdot \mathbf{v}^{\mathrm{m}} = 0 \tag{3.1}$$

Momentum conservation

$$\begin{aligned}
\frac{\partial \rho^{\mathrm{m}} \mathbf{v}^{\mathrm{m}}}{\partial t} + \nabla \cdot (\rho^{\mathrm{m}} \mathbf{v}^{\mathrm{m}} \mathbf{v}^{\mathrm{m}}) =\ & -\nabla P + \frac{1}{\mathrm{Re}_{\mathrm{ref}}} \nabla \cdot \mu^{\mathrm{m}} \left[\nabla \mathbf{v}^{\mathrm{m}} + (\nabla \mathbf{v}^{\mathrm{m}})^T \right] \\
& -(1-f) \frac{\mathrm{Eo}_{\mathrm{ref}}}{\mathrm{We}_{\mathrm{ref}}} \frac{\mathbf{g}^{\star}}{g^{\star}} + \mathrm{Eu}_{\mathrm{ref}} \mathbf{e}_p + \frac{\kappa A_{\mathrm{int}}}{\mathrm{We}_{\mathrm{ref}}} \mathbf{n}
\end{aligned} \tag{3.2}$$

Energy conservation

$$\frac{\partial \rho^{\mathrm{m}} h^{\mathrm{m}}}{\partial t} + \nabla \cdot (\rho^{\mathrm{m}} h^{\mathrm{m}} \mathbf{v}^{\mathrm{m}}) = -\frac{1}{\mathrm{Pe}_{\mathrm{ref}}} \nabla \cdot \mathbf{q}^{\mathrm{m}} \tag{3.3}$$

where the mixture quantities $\mathbf{v}^{\mathrm{m}}, \rho^{\mathrm{m}}, \mu^{\mathrm{m}}$ are defined in (3.25), $\mathbf{q}^{\mathrm{m}}$ represents the conductive flux and the following scaling has been considered:

$$\begin{aligned}
x &= \frac{x^{\star}}{l_{\mathrm{ref}}^{\star}} & \nabla &= l_{\mathrm{ref}}^{\star} \nabla^{\star} & \mathbf{v} &= \frac{\mathbf{v}^{\star}}{v_{\mathrm{ref}}^{\star}} \\
\rho &= \frac{\rho^{\star}}{\rho_{\mathrm{ref}}^{\star}} & t &= \frac{t^{\star}}{t_{\mathrm{ref}}^{\star}} = \frac{t^{\star} v_{\mathrm{ref}}^{\star}}{l_{\mathrm{ref}}^{\star}} & \frac{\partial}{\partial t} &= \frac{l_{\mathrm{ref}}^{\star}}{v_{\mathrm{ref}}^{\star}} \frac{\partial}{\partial t^{\star}} \\
P &= \frac{p^{\star}}{\rho_{\mathrm{ref}}^{\star} v_{\mathrm{ref}}^{\star 2}} & A_{\mathrm{int}} &= \frac{A_{\mathrm{int}}^{\star}}{l_{\mathrm{ref}}^{\star 2}} & h &= \frac{h^{\star}}{h_{\mathrm{ref}}^{\star}}
\end{aligned} \tag{3.4}$$

The reference non-dimensional Reynolds, Eötvos, Weber and Peclet number based

---

[1]Since the volume averaging of the species conservation equation presented in chapter 3.3 is similar to the one performed by Sabisch [68], Wörner et al. [104] and Ghidersa [23], no details are given here for the volume averaging of mass, momentum and energy equation.

on this scaling are:

$$
\text{Re}_{\text{ref}} = \frac{\rho_{\text{ref}}^{\star} v_{\text{ref}}^{\star} l_{\text{ref}}^{\star}}{\mu_{\text{ref}}^{\star}} \qquad \text{E\"o}_{\text{ref}} = \frac{(\rho_1^{\star} - \rho_2^{\star})\, g\, l_{\text{ref}}^{\star\,2}}{\sigma^{\star}} \qquad \text{Eu}_{\text{ref}} = \frac{|\nabla p^{\star}|}{\rho_{\text{ref}}^{\star} v_{\text{ref}}^{\star\,2}}
$$

$$
\text{We}_{\text{ref}} = \frac{\rho_{\text{ref}}^{\star} l_{\text{ref}}^{\star} v_{\text{ref}}^{\star\,2}}{\sigma^{\star}} \qquad \text{Pe}_{\text{ref}} = \frac{\rho_{\text{ref}}^{\star} c_p^{\star} l_{\text{ref}}^{\star} v_{\text{ref}}^{\star}}{\lambda^{\star}},
$$

$$(3.5)$$

where $\sigma^{\star}$ is the surface tension, $\lambda^{\star}$ is the heat conductivity and $|\nabla p^{\star}|$ represents the pressure drop per unit length.

The interface is tracked by means of the Volume-of-Fluid (VoF) method. The basics of the method is the definition of a scalar quantity f, which takes the values $f = 1$ for cells containing only liquid, $f = 0$ for cells containing only gas and $0 < f < 1$ for cells containing the interface. To account for the phase-interface motion, the transport equation of the liquid volumetric fraction is considered:

$$
\frac{\partial f}{\partial t} + \mathbf{v}^{\text{m}} \cdot \nabla f = 0 \tag{3.6}
$$

For cells containing the interface, the homogeneous mixture model is used, i.e. the fluids share the same velocity and pressure.

The computer code `TURBIT-VoF` uses the geometrical method EPIRA (Exact Plane Interface Reconstruction Algorithm), which yields a linearly-accurate interface reconstruction on a three-dimensional structured orthogonal non-equidistant fixed grid [68]. The algorithm belongs to the PLIC (Piecewise Linear Interface Calculation) methods. The interface is reconstructed as a three-dimensional plane, regardless of its orientation and is second order accurate. Secondly, the EPIRA algorithm computes the liquid fluxes across the faces of the mesh cells.

The code is based on a finite volume method and employs a regular staggered grid. The spatial derivatives are discretized using a second order central difference scheme. The unsteady term is discretized by an explicit third order Runge-Kutta method. No phase change is considered and at the walls the no-slip condition is assumed.

3.2 Non-dimensional form of the species conservation equation

In order to solve the governing equations for an entire class of similar problems, and not just for a single case, the non-dimensional form of the equations will be employed, by means of the following scaling:

$$
c_k^{\alpha} = \frac{\tilde{c}_k^{\alpha\,\star}}{c_{\text{ref}}^{\alpha\,\star}} \qquad k_k^{\alpha} = \frac{l_{\text{ref}}^{\star}}{v_{\text{ref}}^{\star}} k_{\text{ref}}^{\alpha\,\star} \qquad D_k^{\alpha} = \frac{D_k^{\alpha\,\star}}{D_{\text{ref}}^{\alpha\,\star}} \qquad \mathbf{j}_k^{\alpha} = \frac{\tilde{\mathbf{j}}_{\text{ref}}^{\alpha\,\star} l_{\text{ref}}^{\star}}{D_{\text{ref}}^{\alpha\,\star} c_{\text{ref}}^{\alpha\,\star}} \tag{3.7}
$$

The reference Schmidt number can therefore be defined as follows:

$$\text{Sc}_{\text{ref}}^{\alpha} = \frac{\mu_{\text{ref}}^{\star}}{\rho_{\text{ref}}^{\star} D_{\text{ref}}^{\alpha \star}} \tag{3.8}$$

Considering the scaling (3.4, 3.5, 3.7 and 3.8) the non-dimensional form of the species conservation equation (2.2) can be written as:

$$\frac{\partial c_k^{\alpha}}{\partial t} + \nabla \cdot (c_k^{\alpha} \mathbf{v}_k) = -\frac{1}{\text{Re}_{\text{ref}} \cdot \text{Sc}_{\text{ref}}^{\alpha}} \nabla \cdot \mathbf{j}_k^{\alpha} + k_k^{(1)\alpha} c_k^{\alpha} \tag{3.9}$$

The thermodynamic condition (2.17) expressed in dimensionless form is:

$$c_{1i}^{\alpha} = c_{2i}^{\alpha} \tag{3.10}$$

while the equal normal molar fluxes condition (2.18) becomes:

$$\mathbf{j}_{1i}^{\alpha} \cdot \mathbf{n} = \frac{1}{H^{\alpha}} \mathbf{j}_{2i}^{\alpha} \cdot \mathbf{n} \quad \rightarrow \quad [-D_1^{\alpha} \nabla c_1^{\alpha}]_i \cdot \mathbf{n} = \left[-\frac{D_2^{\alpha}}{H^{\alpha}} \nabla c_2^{\alpha} \right]_i \cdot \mathbf{n} \tag{3.11}$$

3.3 Volume averaging of species conservation equation

3.3.1 Volume averaging of species conservation equation for individual phases

In order to obtain a species conservation equation valid for the entire flow domain, containing both phases, a phase indicator function is introduced:

$$X_k(\mathbf{x}, t) = \begin{cases} 1, & \mathbf{x} \in \Omega_k(t) \\ 0, & \text{otherwise.} \end{cases} \qquad k = 1, 2 \tag{3.12}$$

Multiplying equations (3.9) with their respective phase indicator function, and considering the average over volume V, one obtains:

$$\overline{X_k \frac{\partial c_k^{\alpha}}{\partial t}}^V + \overline{X_k \nabla \cdot (c_k^{\alpha} \mathbf{v}_k)}^V = -\overline{\frac{1}{\text{Re}_{\text{ref}} \cdot \text{Sc}_{\text{ref}}^{\alpha}} X_k \nabla \cdot \mathbf{j}_k^{\alpha}}^V + \overline{X_k k_k^{(1)\alpha} c_k^{\alpha}}^V \tag{3.13}$$

Following the Leibniz rule [16] the first term in equation (3.13) can be expressed as:

$$\overline{X_k \frac{\partial c_k^{\alpha}}{\partial t}}^V = \frac{\partial}{\partial t} \overline{X_k c_k^{\alpha}}^V + \overline{c_k^{\alpha} \mathbf{v}_i \cdot \nabla X_k}^V \tag{3.14}$$

The second term from equation (3.13) can be expressed following the Gauss rule [16]:

$$\overline{X_k \nabla \cdot (c_k^{\alpha} \mathbf{v}_k)}^V = \nabla \cdot \left(\overline{X_k c_k^{\alpha} \mathbf{v}_k}^V \right) - \overline{c_k^{\alpha} \mathbf{v}_{ki} \cdot \nabla X_k}^V \tag{3.15}$$

The volume averaging of the diffusive flux in equation (3.13) can be further extended as:

$$\overline{\frac{1}{\text{Re}_{\text{ref}} \cdot \text{Sc}_{\text{ref}}^{\alpha}} X_k \nabla \cdot \mathbf{j}_k^{\alpha}}^V = \frac{1}{\text{Re}_{\text{ref}} \cdot \text{Sc}_{\text{ref}}^{\alpha}} \left[\nabla \cdot \left(\overline{X_k \mathbf{j}_k^{\alpha}}^V \right) - \overline{\mathbf{j}_{ki}^{\alpha} \cdot \nabla X_k}^V \right], \qquad (3.16)$$

Introducing the terms developed above in equation (3.13), the volume averaging of a general species conservation equation yields:

$$\begin{aligned} \frac{\partial}{\partial t} \overline{X_k c_k^{\alpha}}^V + \nabla \cdot \left(\overline{X_k c_k^{\alpha} \mathbf{v}_k}^V \right) &= \overline{c_k^{\alpha}(\mathbf{v}_{ki} - \mathbf{v}_i) \cdot \nabla X_k}^V \\ &- \frac{1}{\text{Re}_{\text{ref}} \cdot \text{Sc}_{\text{ref}}^{\alpha}} \left[\nabla \cdot \left(\overline{X_k \mathbf{j}_k^{\alpha}}^V \right) - \overline{\mathbf{j}_{ki}^{\alpha} \cdot \nabla X_k}^V \right] + k_k^{(1)\alpha} \overline{X_k c_k^{\alpha}}^V \end{aligned}$$

$$(3.17)$$

In equation (3.17) the term $\overline{c_k^{\alpha}(\mathbf{v}_{ki} - \mathbf{v}_i) \cdot \nabla X_k}^V$ represents the transfer of mass across the interface due to phase change. Since phase change is not considered in this study, the kinematic boundary condition stating that the velocity at the interface is continuous can be employed. Therefore, it can be considered that $\mathbf{v}_{ki} = \mathbf{v}_i$, which yields:

$$\overline{c_k^{\alpha}(\mathbf{v}_{ki} - \mathbf{v}_i) \cdot \nabla X_k}^V = 0 \qquad (3.18)$$

Accordingly, the volume averaged species conservation equation (3.17) for individual phases becomes:

$$\frac{\partial}{\partial t} \overline{X_k c_k^{\alpha}}^V + \nabla \cdot \left(\overline{X_k c_k^{\alpha} \mathbf{v}_k}^V \right) = -\frac{1}{\text{Re}_{\text{ref}} \cdot \text{Sc}_{\text{ref}}^{\alpha}} \left[\nabla \cdot \left(\overline{X_k \mathbf{j}_k^{\alpha}}^V \right) - \overline{\mathbf{j}_{ki}^{\alpha} \cdot \nabla X_k}^V \right] + k_k^{(1)\alpha} \overline{X_k c_k^{\alpha}}^V$$

$$(3.19)$$

3.3.2 Volume averaging of species conservation equation for two-phase mixture

Summing up the species conservation equations (3.19) leads to an equation for transport of species α that is valid throughout the entire two-phase mixture:

$$\begin{aligned} \sum_{k=1}^{2} \left[\frac{\partial}{\partial t} \overline{X_k c_k^{\alpha}}^V + \nabla \cdot \left(\overline{X_k c_k^{\alpha} \mathbf{v}_k}^V \right) \right] &= -\frac{1}{\text{Re}_{\text{ref}} \cdot \text{Sc}_{\text{ref}}^{\alpha}} \sum_{k=1}^{2} \left[\nabla \cdot \left(\overline{X_k \mathbf{j}_k^{\alpha}}^V \right) - \overline{\mathbf{j}_{ki}^{\alpha} \cdot \nabla X_k}^V \right] \\ &+ \sum_{k=1}^{2} k_k^{(1)\alpha} \overline{X_k c_k^{\alpha}}^V \end{aligned}$$

$$(3.20)$$

The volume averaging procedure and the fact that the diffusive flux presents a jump at interface lead to the appearance of the interfacial term $\overline{\mathbf{j}_k^{\alpha} \cdot \nabla X_k}^V$. This term is considered further in Appendix B.

Applying equation (B.4) will lead to the volume averaged species conservation equation for two-phase systems:

$$\sum_{k=1}^{2}\left[\frac{\partial}{\partial t}\overline{X_k c_k^\alpha}^V + \nabla\cdot\left(\overline{X_k c_k^\alpha \mathbf{v}_k}^V\right)\right] = -\frac{1}{\mathrm{Re}_{\mathrm{ref}}\cdot\mathrm{Sc}_{\mathrm{ref}}^\alpha}\left\{\sum_{k=1}^{2}\left[\nabla\cdot\left(\overline{X_k \mathbf{j}_k^\alpha}^V\right)\right]\right.$$
$$\left.+\frac{H^\alpha-1}{H^\alpha}\frac{1}{V}\int_{S_i}\mathbf{j}_{2i}^\alpha\cdot\mathbf{n}_2\mathrm{d}S\right\}+\sum_{k=1}^{2}k_k^{(1)\alpha}\overline{X_k c_k^\alpha}^V \tag{3.21}$$

For the analysis of mass transfer and chemical reaction in multi-phase systems it is more convenient to consider the intrinsic phase averaging [92, 96] (i.e. integrating over the volume of phase k). Therefore, the following "conserved" variables are considered:

$$\begin{aligned}
\overline{\rho_k}^k &= \frac{\overline{X_k \rho_k}^V}{\alpha_k} & \overline{c_k^\alpha}^k &= \frac{\overline{X_k c_k^\alpha}^V}{\alpha_k} \\
\overline{\mathbf{v}_k}^k &= \frac{\overline{X_k \rho_k \mathbf{v}_k}^V}{\alpha_k \overline{\rho_k}^k} & \overline{\mathbf{j}_k^\alpha}^k &= \frac{\overline{X_k \mathbf{j}_k^\alpha}^V}{\alpha_k},
\end{aligned} \tag{3.22}$$

where

$$\alpha_k = \overline{X_k}^V \tag{3.23}$$

In this study it is assumed that the concentration of species α is so low that it does not change the phase density ρ_k, which remains therefore constant.

Introducing the conserved variables (3.22) in equation (3.21) one obtains:

$$\sum_{k=1}^{2}\left[\frac{\partial}{\partial t}\alpha_k\overline{c_k^\alpha}^k + \nabla\cdot\overline{X_k c_k^\alpha \mathbf{v}_k}^V\right] = -\frac{1}{\mathrm{Re}_{\mathrm{ref}}\cdot\mathrm{Sc}_{\mathrm{ref}}^\alpha}\left\{\sum_{k=1}^{2}\left[\nabla\cdot\left(\alpha_k\overline{\mathbf{j}_k^\alpha}^k\right)\right]\right.$$
$$\left.+\frac{H^\alpha-1}{H^\alpha}\frac{1}{V}\int_{S_i}\mathbf{j}_{2i}^\alpha\cdot\mathbf{n}_2\mathrm{d}S\right\}+\sum_{k=1}^{2}k_k^{(1)\alpha}\alpha_k\overline{c_k^\alpha}^k \tag{3.24}$$

By means of the phase indicator function (3.12) one can express two-phase mixture quantities as follows:

$$\begin{aligned}
\rho^{\mathrm{m}} &\equiv \sum_{k=1}^{2}\alpha_k\overline{\rho_k}^k &&= f\overline{\rho_1}^1+(1-f)\overline{\rho_2}^2 \\[2ex]
\mathbf{v}^{\mathrm{m}} &\equiv \frac{1}{\rho^{\mathrm{m}}}\sum_{k=1}^{2}\alpha_k\overline{\rho_k}^k\overline{\mathbf{v}_k}^k &&= \frac{f\overline{\rho_1}^1\overline{\mathbf{v}_1}^1+(1-f)\overline{\rho_2}^2\overline{\mathbf{v}_2}^2}{f\overline{\rho_1}^1+(1-f)\overline{\rho_2}^2} \\[2ex]
\mu^{\mathrm{m}} &\equiv \sum_{k=1}^{2}\alpha_k\overline{\mu_k}^k &&= f\overline{\mu_1}^1+(1-f)\overline{\mu_2}^2 \\[2ex]
\mathbf{j}^{\alpha\,\mathrm{m}} &\equiv \sum_{k=1}^{2}\alpha_k\overline{\mathbf{j}_k^\alpha}^k &&= f\overline{\mathbf{j}_1^\alpha}^1+(1-f)\overline{\mathbf{j}_2^\alpha}^2,
\end{aligned} \tag{3.25}$$

where $\alpha_1 = f$ represents the liquid volume fraction and $\alpha_2 = 1 - f$ represents the gas volume fraction.

Considering the mass conservation for species α and the assumption that no mass is stored at the interface, one can write the mixture density for species α:

$$\rho^{\alpha\,\mathrm{m}} = \sum_{k=1}^{2} \alpha_k \overline{\rho_k^\alpha}^k \tag{3.26}$$

Dividing relation (3.26) with species α molecular weight M^α one obtains a two-phase mixture concentration of species α:

$$c^{\alpha\,\mathrm{m}} = \frac{\rho^{\alpha\,\mathrm{m}}}{M^\alpha} \equiv \sum_{k=1}^{2} \alpha_k \overline{c_k^\alpha}^k = f\overline{c_1^\alpha}^1 + (1-f)\overline{c_2^\alpha}^2 \tag{3.27}$$

The "conserved" concentrations, $\overline{c_k^\alpha}^k, k = 1, 2$, are introduced as initial data. The initial concentration field is transformed also, according to relation (2.16).

The mixture concentration equation will be assigned to the computational mesh cell center ($c_{i,j,k}^{\alpha\,\mathrm{m}} \equiv c^{\alpha\,\mathrm{m}}$).

Introducing relations (3.25), (3.27) and (A.21) in equation (3.24), the volume averaged single-field species conservation equation can be written in the following compact form:

$$\frac{\partial}{\partial t}c^{\alpha\,\mathrm{m}} + \nabla \cdot (c^{\alpha\,\mathrm{m}}\mathbf{v}^{\mathrm{m}}) = -\frac{1}{\mathrm{Re}_{\mathrm{ref}} \cdot \mathrm{Sc}_{\mathrm{ref}}^\alpha} \left(\nabla \cdot \mathbf{j}^{\alpha\,\mathrm{m}} + \frac{H^\alpha - 1}{H^\alpha}\frac{1}{V} \int_{S_i} \mathbf{j}_{2i}^\alpha \cdot \mathbf{n}_2 \mathrm{d}S \right)$$
$$+ \sum_{k=1}^{2} k_k^{(1)\alpha} \alpha_k \overline{c_k^\alpha}^k \tag{3.28}$$

The derivation of the volume averaged convective term is presented in Appendix A.

In the present study, the consumption of species by homogeneous chemical reaction is considered only in the continuous phase. Therefore, the species balance equation (3.28) simplifies to:

$$\frac{\partial}{\partial t}c^{\alpha\,\mathrm{m}} + \nabla \cdot (c^{\alpha\,\mathrm{m}}\mathbf{v}^{\mathrm{m}}) = -\frac{1}{\mathrm{Re}_{\mathrm{ref}} \cdot \mathrm{Sc}_{\mathrm{ref}}^\alpha} \left(\nabla \cdot \mathbf{j}^{\alpha\,\mathrm{m}} + \frac{H^\alpha - 1}{H^\alpha}\frac{1}{V} \int_{S_i} \mathbf{j}_{2i}^\alpha \cdot \mathbf{n}_2 \mathrm{d}S \right) + k_1^{(1)\alpha} c^{\alpha\,\mathrm{m}}, \tag{3.29}$$

where, for the last term, the following relation holds:

$$c^{\alpha\,\mathrm{m}} = \alpha_1 \overline{c_1^\alpha}^1 \tag{3.30}$$

Based on the proposal of Whitaker [96], the interfacial diffusive flux that has to be evaluated on the gas side of the interface is further neglected.

3.4   Discretization of the convective term

Computer code `TURBIT-VoF` uses a rectilinear Cartesian grid so that each mesh cell is a parallelepiped having six faces denoted by $S_{i\pm1/2,j,k}$, $S_{i,j\pm1/2,k}$ and $S_{i,j,k\pm1/2}$.

Using relation (3.27) the non-dimensional volume averaged single-field species conservation equation (3.29), for the case when no chemical reaction occurs, can be written for a computational cell (i, j, k) as follows:

$$\frac{\partial c_{i,j,k}^{\alpha\,\mathrm{m}}}{\partial t} + \left[\nabla \cdot (c^{\alpha\,\mathrm{m}}\mathbf{v}^{\mathrm{m}})\right]_{i,j,k} = -\frac{1}{\mathrm{Re}_{\mathrm{ref}} \cdot \mathrm{Sc}_{\mathrm{ref}}^{\alpha}}\left[\nabla \cdot \mathbf{j}^{\alpha\,\mathrm{m}}\right]_{i,j,k} \tag{3.31}$$

The convective term from the volume averaged single-field species conservation equation represents the sum of all convective fluxes over control volume faces:

$$\left[\nabla \cdot (c^{\alpha\,\mathrm{m}}\mathbf{v}^{\mathrm{m}})\right]_{i,j,k} = \sum_{l=1}^{6} \frac{S_l}{V_{i,j,k}} \frac{1}{S_l} \int_{S_l} c^{\alpha}\mathbf{v} \cdot \mathbf{n}_l \,\mathrm{d}S, \tag{3.32}$$

where $V_{i,j,k}$ is a computational cell, S_l represents the faces of control volume $V_{i,j,k}$ and $\mathbf{n}_l$ represents the unit normal vector of the mesh cell faces pointing outside of the mesh cell. The velocity field is supposed known from the numerical integration of the momentum equation.

The convective flux of a species through the face $S_{i,j,k+\frac{1}{2}}$ of a control volume is:

$$\frac{1}{S_{i,j,k+\frac{1}{2}}} \int_{S_{i,j,k+\frac{1}{2}}} c^{\alpha}w_z \,\mathrm{d}S = \frac{f_{i,j,k+\frac{1}{2}}^{1}}{S_{i,j,k+\frac{1}{2}}^{1}} \int_{S_{i,j,k+\frac{1}{2}}^{1}} c^{\alpha}w_z \,\mathrm{d}S + \frac{1 - f_{i,j,k+\frac{1}{2}}^{1}}{S_{i,j,k+\frac{1}{2}}^{2}} \int_{S_{i,j,k+\frac{1}{2}}^{2}} c^{\alpha}w_z \,\mathrm{d}S, \tag{3.33}$$

where w_z represents the velocity component along the z axis and $f_{i,j,k+\frac{1}{2}}^{1}$ represents fraction of face $S_{i,j,k+\frac{1}{2}}$ occupied by liquid:

$$f_{i,j,k+\frac{1}{2}}^{1} = \frac{S_{i,j,k+\frac{1}{2}}^{1}}{S_{i,j,k+\frac{1}{2}}} \tag{3.34}$$

while $f_{i,j,k+\frac{1}{2}}^{2}$ represents fraction of face $S_{i,j,k+\frac{1}{2}}$ occupied by gas. The surface fractions satisfy the condition $f_{i,j,k+\frac{1}{2}}^{1} + f_{i,j,k+\frac{1}{2}}^{2} = 1$.

The surface averaged velocity field is considered as follows:

$$\frac{1}{S_{i,j,k+\frac{1}{2}}^{k}} \int_{S_{i,j,k+\frac{1}{2}}^{k}} w_z \,\mathrm{d}S = w_{i,j,k+\frac{1}{2}}^{k} \qquad k = 1, 2 \tag{3.35}$$

At the face $S_{i,j,k+\frac{1}{2}}$ the thermodynamic condition (3.10) implies:

$$\int_{S_{i,j,k+\frac{1}{2}}^{1}} c^{\alpha} \,\mathrm{d}S = \int_{S_{i,j,k+\frac{1}{2}}^{2}} c^{\alpha} \,\mathrm{d}S = c_{i,j,k+\frac{1}{2}}^{\alpha} \tag{3.36}$$

and therefore the convective flux becomes:

$$\frac{1}{S_{i,j,k+\frac{1}{2}}} \int_{S_{i,j,k+\frac{1}{2}}} c^\alpha w_z \, \mathrm{d}S = f^1_{i,j,k+\frac{1}{2}} c^{\alpha\,1}_{i,j,k+\frac{1}{2}} w^1_{i,j,k+\frac{1}{2}} + \left(1 - f^1_{i,j,k+\frac{1}{2}}\right) c^{\alpha\,2}_{i,j,k+\frac{1}{2}} w^2_{i,j,k+\frac{1}{2}} \quad (3.37)$$

In computer code `TURBIT-VoF` the homogeneous model is used to relate the velocities of the phases at the interface:

$$w^1_{i,j,k+\frac{1}{2}} = w^2_{i,j,k+\frac{1}{2}} \equiv w_{i,j,k+\frac{1}{2}} \quad (3.38)$$

As relation (3.36) suggests, the concentration of species α at the interface between phases is continuous. Therefore, using (3.38), equation (3.37) can be further developed:

$$\frac{1}{S_{i,j,k+\frac{1}{2}}} \int_{S_{i,j,k+\frac{1}{2}}} c^\alpha w_z \, \mathrm{d}S = c^\alpha_{i,j,k+\frac{1}{2}} \, w_{i,j,k+\frac{1}{2}} \quad (3.39)$$

Two numerical schemes have been implemented in `TURBIT-VoF` for the evaluation of the convective flux, i.e. a centered and an upwind approach. As discussed by Ghidersa [23], the centered difference scheme proves more suitable for the bulk region of each fluid, while the upwind scheme avoids the oscillations of the transported quantity, i.e. concentration, at the interface between phases.

For the centered scheme, the cell face concentration $c^\alpha_{i,j,k+\frac{1}{2}}$ can be evaluated by a linear interpolation between the values in neighboring cells (i,j,k) and $(i,j,k+1)$:

$$
\begin{aligned}
c^\alpha_{i,j,k+\frac{1}{2}} &\simeq c^{\alpha\,\mathrm{m}}_{i,j,k} + \frac{c^{\alpha\,\mathrm{m}}_{i,j,k+1} - c^{\alpha\,\mathrm{m}}_{i,j,k}}{z_{i,j,k+\frac{3}{2}} - z_{i,j,k-\frac{1}{2}}} \left(z_{i,j,k+\frac{1}{2}} - z_{i,j,k-\frac{1}{2}}\right) \\
&= \frac{c^{\alpha\,\mathrm{m}}_{i,j,k} \Delta z_{k+1} + c^{\alpha\,\mathrm{m}}_{i,j,k+1} \Delta z_k}{\Delta z_k + \Delta z_{k+1}} + O\left(\Delta^2 z_k\right),
\end{aligned}
\quad (3.40)
$$

where $\Delta z_k = z_{i,j,k+\frac{1}{2}} - z_{i,j,k-\frac{1}{2}}$. Since `TURBIT-VoF` uses an equidistant grid along y and x axis, equation (3.40) can be further extended for these directions as:

$$
\begin{aligned}
c^\alpha_{i,j+\frac{1}{2},k} &\simeq \frac{c^{\alpha\,\mathrm{m}}_{i,j,k} + c^{\alpha\,\mathrm{m}}_{i,j+1,k}}{2} \\
c^\alpha_{i+\frac{1}{2},j,k} &\simeq \frac{c^{\alpha\,\mathrm{m}}_{i,j,k} + c^{\alpha\,\mathrm{m}}_{i+1,j,k}}{2}
\end{aligned}
\quad (3.41)
$$

The mean concentrations $c^{\alpha\,\mathrm{m}}_{i,j,k}$ are known from previous time step, respectively from initial conditions. Using the centered difference scheme of the cell face concentration (3.40) and

(3.41), the convective flux defined by equation (3.32) becomes:

$$
\left[\nabla \cdot (c^{\alpha\,\mathrm{m}} \mathbf{v}^{\mathrm{m}})\right]_{i,j,k} \simeq \frac{1}{\Delta z_k}\left(w_{i,j,k+\frac{1}{2}} \frac{c_{i,j,k}^{\alpha\,\mathrm{m}} \Delta z_{k+1} + c_{i,j,k+1}^{\alpha\,\mathrm{m}} \Delta z_k}{\Delta z_k + \Delta z_{k+1}} - w_{i,j,k-\frac{1}{2}} \frac{c_{i,j,k-1}^{\alpha\,\mathrm{m}} \Delta z_k + c_{i,j,k}^{\alpha\,\mathrm{m}} \Delta z_{k-1}}{\Delta z_k + \Delta z_{k-1}}\right)
$$

$$
+\frac{1}{\Delta y_j}\left(v_{i,j+\frac{1}{2},k} \frac{c_{i,j,k}^{\alpha\,\mathrm{m}} + c_{i,j+1,k}^{\alpha\,\mathrm{m}}}{2} - v_{i,j-\frac{1}{2},k} \frac{c_{i,j-1,k}^{\alpha\,\mathrm{m}} + c_{i,j,k}^{\alpha\,\mathrm{m}}}{2}\right)
$$

$$
+\frac{1}{\Delta x_i}\left(u_{i+\frac{1}{2},j,k} \frac{c_{i,j,k}^{\alpha\,\mathrm{m}} + c_{i+1,j,k}^{\alpha\,\mathrm{m}}}{2} - u_{i-\frac{1}{2},j,k} \frac{c_{i-1,j,k}^{\alpha\,\mathrm{m}} + c_{i,j,k}^{\alpha\,\mathrm{m}}}{2}\right),
$$

$$(3.42)$$

where $\Delta y_j = y_{i,j+\frac{1}{2},k} - y_{i,j-\frac{1}{2},k}$ and $\Delta x_i = x_{i+\frac{1}{2},j,k} - x_{i-\frac{1}{2},j,k}$. For equidistant grids, the scheme is second order accurate.

The concentration at one control volume face, $c_{i,j,k+\frac{1}{2}}^{\alpha}$ can also be estimated using a first order upwind scheme:

$$
w_{i,j,k+\frac{1}{2}} c_{i,j,k+\frac{1}{2}}^{\alpha} \simeq w_{i,j,k+\frac{1}{2}}\left[\frac{1 + \mathrm{sgn}\left(w_{i,j,k+\frac{1}{2}}\right)}{2} c_{i,j,k}^{\alpha\,\mathrm{m}} + \frac{1 - \mathrm{sgn}\left(w_{i,j,k+\frac{1}{2}}\right)}{2} c_{i,j,k+1}^{\alpha\,\mathrm{m}}\right], \qquad (3.43)
$$

where the sign function is:

$$
\mathrm{sgn}(x) = \begin{cases} 1, & \text{if } x > 0 \\ 0, & \text{if } x = 0 \\ -1, & \text{if } x < 0 \end{cases} \qquad (3.44)
$$

Using the upwind formulation of the face concentration (3.43), the convective flux defined by equation (3.32) becomes:

$$
\left[\nabla \cdot (c^{\alpha\,\mathrm{m}} \mathbf{v}^{\mathrm{m}})\right]_{i,j,k} \simeq \frac{1}{\Delta z_k}\left\{w_{i,j,k+\frac{1}{2}}\left[\frac{1 + \mathrm{sgn}\left(w_{i,j,k+\frac{1}{2}}\right)}{2} c_{i,j,k}^{\alpha\,\mathrm{m}} + \frac{1 - \mathrm{sgn}\left(w_{i,j,k+\frac{1}{2}}\right)}{2} c_{i,j,k+1}^{\alpha\,\mathrm{m}}\right]\right.
$$

$$
\left.-w_{i,j,k-\frac{1}{2}}\left[\frac{1 + \mathrm{sgn}\left(w_{i,j,k-\frac{1}{2}}\right)}{2} c_{i,j,k-1}^{\alpha\,\mathrm{m}} + \frac{1 - \mathrm{sgn}\left(w_{i,j,k-\frac{1}{2}}\right)}{2} c_{i,j,k}^{\alpha\,\mathrm{m}}\right]\right\}
$$

$$
+\frac{1}{\Delta y_j}\left\{v_{i,j+\frac{1}{2},k}\left[\frac{1 + \mathrm{sgn}\left(v_{i,j+\frac{1}{2},k}\right)}{2} c_{i,j,k}^{\alpha\,\mathrm{m}} + \frac{1 - \mathrm{sgn}\left(v_{i,j+\frac{1}{2},k}\right)}{2} c_{i,j+1,k}^{\alpha\,\mathrm{m}}\right]\right.
$$

$$
\left.-v_{i,j-\frac{1}{2},k}\left[\frac{1 + \mathrm{sgn}\left(v_{i,j-\frac{1}{2},k}\right)}{2} c_{i,j-1,k}^{\alpha\,\mathrm{m}} + \frac{1 - \mathrm{sgn}\left(v_{i,j-\frac{1}{2},k}\right)}{2} c_{i,j,k}^{\alpha\,\mathrm{m}}\right]\right\}
$$

$$
+\frac{1}{\Delta x_i}\left\{u_{i+\frac{1}{2},j,k}\left[\frac{1 + \mathrm{sgn}\left(u_{i+\frac{1}{2},j,k}\right)}{2} c_{i,j,k}^{\alpha\,\mathrm{m}} + \frac{1 - \mathrm{sgn}\left(u_{i+\frac{1}{2},j,k}\right)}{2} c_{i+1,j,k}^{\alpha\,\mathrm{m}}\right]\right.
$$

$$
\left.-u_{i-\frac{1}{2},j,k}\left[\frac{1 + \mathrm{sgn}\left(u_{i-\frac{1}{2},j,k}\right)}{2} c_{i-1,j,k}^{\alpha\,\mathrm{m}} + \frac{1 - \mathrm{sgn}\left(u_{i-\frac{1}{2},j,k}\right)}{2} c_{i,j,k}^{\alpha\,\mathrm{m}}\right]\right\}
$$

$$(3.45)$$

The upwind method offers the advantage of handling very sharp discontinuities without occurrence of the Gibbs phenomena, i.e. the computed solution presents no oscillations in the vicinity of the discontinuity. The disadvantages are that it is only first order accurate and highly diffusive [2]. A second-order upwind scheme can diminish the diffusive character of the first order method at the cost of oscillatory behavior in the vicinity of the discontinuity. Still, a second order upwind scheme can satisfy a total variation diminishing (TVD) condition, restricting therefore the amplitude of the gradients at the discontinuity, if flux limiters are considered.

3.5   Discretization of the diffusive term

Using Gauss theorem one can evaluate numerically the divergence of the diffusive flux as the sum of all normal molar fluxes over control volume faces:

$$
-\frac{1}{\mathrm{Re_{ref} \cdot Sc_{ref}^{\alpha}}}\left[\nabla \cdot \mathbf{j}^{\alpha\,\mathrm{m}}\right]_{i,j,k} = -\frac{1}{\mathrm{Re_{ref} \cdot Sc_{ref}^{\alpha}}}\sum_{l=1}^{6}\frac{S_l}{V_{i,j,k}}\frac{1}{S_l}\int_{S_l}\mathbf{j}^{\alpha\,\mathrm{m}}\cdot\mathbf{n}_l\,\mathrm{d}S
$$
$$
= \frac{1}{\mathrm{Re_{ref} \cdot Sc_{ref}^{\alpha}}}\sum_{l=1}^{6}\frac{S_l}{V_{i,j,k}}\frac{1}{S_l}\int_{S_l}D^{\alpha\,\mathrm{m}}\frac{\partial c^{\alpha\,\mathrm{m}}}{\partial n}\,\mathrm{d}S,
$$
(3.46)

For a control volume surface $S_{i,j,k+\frac{1}{2}}$, the integral of the molar flux is:

$$
\frac{1}{S_{i,j,k+\frac{1}{2}}}\int_{S_{i,j,k+\frac{1}{2}}}D^{\alpha}\frac{\partial c^{\alpha}}{\partial z}\,\mathrm{d}S = \frac{f^1_{i,j,k+\frac{1}{2}}}{S^1_{i,j,k+\frac{1}{2}}}\int_{S^1_{i,j,k+\frac{1}{2}}}D^{\alpha}\frac{\partial c^{\alpha}}{\partial z}\,\mathrm{d}S + \frac{1-f^1_{i,j,k+\frac{1}{2}}}{S^2_{i,j,k+\frac{1}{2}}}\int_{S^2_{i,j,k+\frac{1}{2}}}D^{\alpha}\frac{\partial c^{\alpha}}{\partial z}\,\mathrm{d}S
$$
$$
= \frac{1}{S_{i,j,k+\frac{1}{2}}}\left(\int_{S^1_{i,j,k+\frac{1}{2}}}D^{\alpha}\frac{\partial c^{\alpha}}{\partial z}\,\mathrm{d}S + \int_{S^2_{i,j,k+\frac{1}{2}}}D^{\alpha}\frac{\partial c^{\alpha}}{\partial z}\,\mathrm{d}S\right)
$$
(3.47)

where $D^{\alpha\,\mathrm{m}}$, is the mean diffusivity of species α. As can be seen in equation above, the mean diffusivity has be be evaluated at the cell faces. Two formulations for the cell face diffusivity, presented by Patankar [59] and Davidson and Rudman [14] have been implemented in `TURBIT-VoF` after appropriate modification that allowed handling of discontinuous concentration fields.

Patankar [59] developed a one-dimensional method to express the thermal conductivity at the interface. Taking into account the analogy between mass and heat transfer, this approach leads to a similar formula for mass diffusivity at interface. His approach is based on the continuity of physical parameters (i.e. concentration in this case) and equal interfacial diffusive fluxes. This approach was adapted to account for the jump conditions that characterizes the mass transfer process.

Still, this local value of the diffusivity does not represent a major concern, but rather the representation of the molar flux at the interface. Patankar's approach considers two
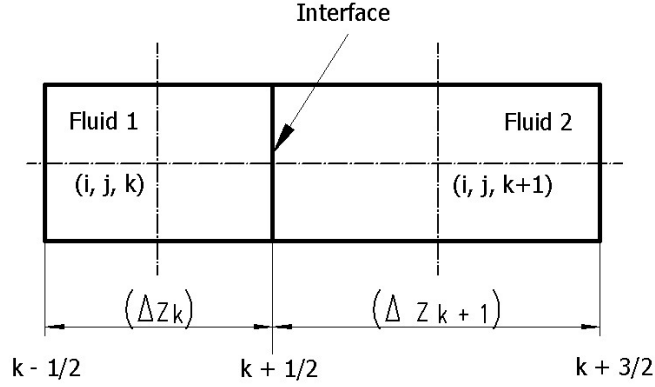
Figure 3.1: Illustration for the evaluation of the diffusive flux at face $S_{i,j,k+\frac{1}{2}}$ using Patankar's approach [59]

separate computational cells, as displayed in Figure 3.1, filled with different fluids. It will be assumed that the diffusivity varies in a stepwise fashion from a control volume to the next one.

Taking into account the concentration transformation (2.16), the interfacial jump of the concentration field is shifted into a jump of the normal molar flux. Therefore, the interfacial diffusion fluxes can be written as:

$$j^{\alpha\,1}_{i,j,k+\frac{1}{2}} \;=\; D^{\alpha\,\mathrm{m}}_{i,j,k}\frac{c^{\alpha\,\mathrm{m}}_{i,j,k+\frac{1}{2}} - c^{\alpha\,\mathrm{m}}_{i,j,k}}{\Delta z_k/2} \tag{3.48}$$

$$j^{\alpha\,2}_{i,j,k+\frac{1}{2}} \;=\; \frac{D^{\alpha\,\mathrm{m}}_{i,j,k+1}}{H^{\alpha}_{i,j,k+\frac{1}{2}}}\frac{c^{\alpha\,\mathrm{m}}_{i,j,k+1} - c^{\alpha\,\mathrm{m}}_{i,j,k+\frac{1}{2}}}{\Delta z_{k+1}/2}, \tag{3.49}$$

where $D^{\alpha\,\mathrm{m}}_{i,j,k}$ is the cell mixture diffusivity:

$$D^{\alpha\,\mathrm{m}}_{i,j,k} = f_{i,j,k}D^{\alpha}_1 + (1 - f_{i,j,k})D^{\alpha}_2 \tag{3.50}$$

and $H^{\alpha}_{i,j,k+\frac{1}{2}}$ represents the cell Henry number. For complicated geometries the interface can be contained in several neighboring cells, as presented in Figure 3.2. The input Henry number H^{α} is applied to the mass flux evaluated at the cell face k $+ \frac{1}{2}$ if one of the conditions in Table 3.1 is fulfilled. For all other cell faces the cell Henry number $H^{\alpha}_{i,j,k+\frac{1}{2}}$ is considered unity, as displayed in Figure 3.2.

The interfacial cells contain mean values for concentration and have therefore a smaller concentration than the one in the dispersed phase. Allocating the physical Henry number H^{α} into one of these interfacial cells will lead to a smaller mass flux and will underestimate the diffusion.

Since the molar fluxes (3.48) and (3.49) are equal, as assumed by the interfacial

f_k	f_{k+1}
$0 < f_k < 1$	$f_{k+1}=0$ or $f_{k+1}=1$
$f_{k+1}=0$ or $f_{k+1}=1$	$0 < f_k < 1$
$f_k = 1$	$f_{k+1}=0$
$f_k = 0$	$f_{k+1}=1$

Table 3.1: Conditions for allocating the physical Henry number H^α as cell Henry number $H^\alpha_{i,j,k}$
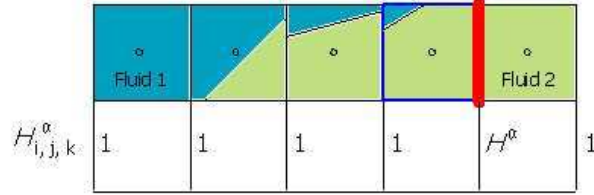
Figure 3.2: Cell face for which the jump in the mass flux is allocated. Cell Henry number $H^\alpha_{i,j,k}$.

condition (2.18), one can obtain the species concentration at the cell face:

$$c^{\alpha\,\mathrm{m}}_{i,j,k+\frac{1}{2}} = \frac{H^\alpha_{i,j,k+\frac{1}{2}} D^{\alpha\,\mathrm{m}}_{i,j,k} c^{\alpha\,\mathrm{m}}_{i,j,k} \Delta z_{k+1} + D^{\alpha\,\mathrm{m}}_{i,j,k+1} c^{\alpha\,\mathrm{m}}_{i,j,k+1} \Delta z_k}{D^{\alpha\,\mathrm{m}}_{i,j,k} H^\alpha_{i,j,k+\frac{1}{2}} \Delta z_{k+1} + D^{\alpha\,\mathrm{m}}_{i,j,k+1} \Delta z_k}, \tag{3.51}$$

which, in case of y and x directions, becomes:

$$c^\alpha_{i,j+\frac{1}{2},k} = \frac{H^\alpha_{i,j+\frac{1}{2},k} D^{\alpha\,\mathrm{m}}_{i,j,k} c^{\alpha\,\mathrm{m}}_{i,j,k} + D^{\alpha\,\mathrm{m}}_{i,j+1,k} c^{\alpha\,\mathrm{m}}_{i,j+1,k}}{D^{\alpha\,\mathrm{m}}_{i,j,k} H^\alpha_{i,j+\frac{1}{2},k} + D^{\alpha\,\mathrm{m}}_{i,j+1,k}}, \tag{3.52}$$

$$c^\alpha_{i+\frac{1}{2},j,k} = \frac{H^\alpha_{i+\frac{1}{2},j,k} D^{\alpha\,\mathrm{m}}_{i,j,k} c^{\alpha\,\mathrm{m}}_{i,j,k} + D^{\alpha\,\mathrm{m}}_{i+1,j,k} c^{\alpha\,\mathrm{m}}_{i+1,j,k}}{D^{\alpha\,\mathrm{m}}_{i,j,k} H^\alpha_{i+\frac{1}{2},j,k} + D^{\alpha\,\mathrm{m}}_{i+1,j,k}}, \tag{3.53}$$

If the interfacial concentration (3.51) is inserted in equation (3.48) or (3.49) one can obtain the flux at the interface:

$$j^\alpha_{i,j,k+\frac{1}{2}} = 2 \frac{c^{\alpha\,\mathrm{m}}_{i,j,k+1} - c^{\alpha\,\mathrm{m}}_{i,j,k}}{\frac{\Delta z_k}{D^{\alpha\,\mathrm{m}}_{i,j,k}} + \frac{H^\alpha_{i,j,k+\frac{1}{2}} \Delta z_{k+1}}{D^{\alpha\,\mathrm{m}}_{i,j,k+1}}} \tag{3.54}$$

Equating relation (3.54) with the interfacial molar flux:

$$D^\alpha_{i,j,k+\frac{1}{2}} \frac{c^{\alpha\,\mathrm{m}}_{i,j,k+1} - c^{\alpha\,\mathrm{m}}_{i,j,k}}{z_{i,j,k+1} - z_{i,j,k}} = 2 \frac{c^{\alpha\,\mathrm{m}}_{i,j,k+1} - c^{\alpha\,\mathrm{m}}_{i,j,k}}{\frac{\Delta z_k}{D^{\alpha\,\mathrm{m}}_{i,j,k}} + \frac{H^\alpha_{i,j,k+\frac{1}{2}} \Delta z_{k+1}}{D^{\alpha\,\mathrm{m}}_{i,j,k+1}}} \tag{3.55}$$

one can obtain the molar diffusivity at the interface:

$$D^\alpha_{i,j,k+\frac{1}{2}} = 2\frac{D^{\alpha\,\mathrm{m}}_{i,j,k}D^{\alpha\,\mathrm{m}}_{i,j,k+1}(z_{i,j,k+1} - z_{i,j,k})}{D^{\alpha\,\mathrm{m}}_{i,j,k}H^\alpha_{i,j,k+\frac{1}{2}}\Delta z_{k+1} + D^{\alpha\,\mathrm{m}}_{i,j,k+1}\Delta z_k}, \tag{3.56}$$

which reduces to the harmonic mean of $D^{\alpha\,\mathrm{m}}_{i,j,k}$ and $D^{\alpha\,\mathrm{m}}_{i,j,k+1}$ in case of interface placed between cells (i.e. $z_{i,j,k+1} - z_{i,j,k} = \Delta z_k = \Delta z_{k+1}$):

$$D^\alpha_{i,j,k+\frac{1}{2}} = 2\frac{D^{\alpha\,\mathrm{m}}_{i,j,k}D^{\alpha\,\mathrm{m}}_{i,j,k+1}}{D^{\alpha\,\mathrm{m}}_{i,j,k}H^\alpha_{i,j,k+\frac{1}{2}} + D^{\alpha\,\mathrm{m}}_{i,j,k+1}} \tag{3.57}$$

In case of y and x directions the interfacial molar diffusivity becomes:

$$D^\alpha_{i,j+\frac{1}{2},k} = 2\frac{D^{\alpha\,\mathrm{m}}_{i,j,k}D^{\alpha\,\mathrm{m}}_{i,j+1,k}}{D^{\alpha\,\mathrm{m}}_{i,j,k}H^\alpha_{i,j,k+\frac{1}{2}} + D^{\alpha\,\mathrm{m}}_{i,j+1,k}} \tag{3.58}$$

$$D^\alpha_{i+\frac{1}{2},j,k} = 2\frac{D^{\alpha\,\mathrm{m}}_{i,j,k}D^{\alpha\,\mathrm{m}}_{i+1,j,k}}{D^{\alpha\,\mathrm{m}}_{i,j,k}H^\alpha_{i,j,k+\frac{1}{2}} + D^{\alpha\,\mathrm{m}}_{i+1,j,k}} \tag{3.59}$$

In analogy with the interfacial heat transfer problem, treated by Patankar, for a computational grid having a constant mesh size Δz, it can be considered that the harmonic mean of the cell diffusivities is a more appropriate expression of the control volume face diffusivity $D^\alpha_{i,j,k+\frac{1}{2}}$ than the arithmetic mean. Sharp changes of the diffusivity are expected to be handled more accurately following this approach.

Davidson and Rudman [14] proposed an empirical formula for the computation of the heat conductivity coefficient taking into account the volume fraction instead of mesh cell lengths. The same assumptions considered by Patankar, i.e. continuous interfacial concentration and equal interfacial mass fluxes, have been deemed. Therefore, similar to the treatment of the previous approach, the formula presented in [14] can be extended to account for mass transfer studies:

$$D^\alpha_{i,j,k+\frac{1}{2}} = \frac{D^{\alpha\,\mathrm{m}}_{i,j,k}D^{\alpha\,\mathrm{m}}_{i,j,k+1}}{H^\alpha_{i,j,k+\frac{1}{2}}D^{\alpha\,\mathrm{m}}_{i,j,k}(1.5 - \lambda_k) + D^{\alpha\,\mathrm{m}}_{i,j,k+1}(\lambda_k - 0.5)}, \tag{3.60}$$

where

$$\lambda_k = \max\big[\min(f_{i,j,k} + f_{i,j,k+1}, 1.5), 0.5\big] \tag{3.61}$$

For the cell face diffusivity along y and x axis the formulae have equivalent expression.

Patankar's formulas (3.56), (3.58) and (3.59) would require the assumption of interface placed between cells. The formula of Davidson and Rudman avoids this restriction by incorporating the volume fraction, and therefore a random placed interface inside a cell is allowed. Nevertheless, in case of interface placed between cells, the formula (3.60) reduces to Patankar's harmonic mean formula (3.57).

Evaluating the molar fluxes by second order centered difference scheme, one can express the diffusive term (3.46) as follows:

$$-\frac{1}{\mathrm{Re_{ref}} \cdot \mathrm{Sc_{ref}^\alpha}} \left[\nabla \cdot \mathbf{j}^{\alpha\,m} \right]_{i,j,k} \simeq$$

$$-\frac{1}{\mathrm{Re_{ref}} \cdot \mathrm{Sc_{ref}^\alpha}} \left(\frac{j^\alpha_{i,j,k+\frac{1}{2}} - j^\alpha_{i,j,k-\frac{1}{2}}}{z_{i,j,k+\frac{1}{2}} - z_{i,j,k-\frac{1}{2}}} + \frac{j^\alpha_{i,j+\frac{1}{2},k} - j^\alpha_{i,j-\frac{1}{2},k}}{y_{i,j+\frac{1}{2},k} - y_{i,j-\frac{1}{2},k}} + \frac{j^\alpha_{i+\frac{1}{2},j,k} - j^\alpha_{i-\frac{1}{2},j,k}}{x_{i+\frac{1}{2},j,k} - x_{i-\frac{1}{2},j,k}} \right)$$

$$= \frac{1}{\mathrm{Re_{ref}} \cdot \mathrm{Sc_{ref}^\alpha}} \left[\left(D^\alpha_{i,j,k+\frac{1}{2}} \frac{c^{\alpha\,m}_{i,j,k+1} - c^{\alpha\,m}_{i,j,k}}{z_{i,j,k+1} - z_{i,j,k}} - D^\alpha_{i,j,k-\frac{1}{2}} \frac{c^{\alpha\,m}_{i,j,k} - c^{\alpha\,m}_{i,j,k-1}}{z_{i,j,k} - z_{i,j,k-1}} \right) \frac{1}{z_{i,j,k+\frac{1}{2}} - z_{i,j,k-\frac{1}{2}}} \right.$$

$$+ \left(D^\alpha_{i,j+\frac{1}{2},k} \frac{c^{\alpha\,m}_{i,j+1,k} - c^{\alpha\,m}_{i,j,k}}{y_{i,j+1,k} - y_{i,j,k}} - D^\alpha_{i,j-\frac{1}{2},k} \frac{c^{\alpha\,m}_{i,j,k} - c^{\alpha\,m}_{i,j-1,k}}{y_{i,j,k} - y_{i,j-1,k}} \right) \frac{1}{y_{i,j+\frac{1}{2},k} - y_{i,j-\frac{1}{2},k}}$$

$$\left. + \left(D^\alpha_{i+\frac{1}{2},j,k} \frac{c^{\alpha\,m}_{i+1,j,k} - c^{\alpha\,m}_{i,j,k}}{x_{i+1,j,k} - x_{i,j,k}} - D^\alpha_{i-\frac{1}{2},j,k} \frac{c^{\alpha\,m}_{i,j,k} - c^{\alpha\,m}_{i-1,j,k}}{x_{i,j,k} - x_{i-1,j,k}} \right) \frac{1}{x_{i+\frac{1}{2},j,k} - x_{i-\frac{1}{2},j,k}} \right],$$

$$(3.62)$$

where the cell face diffusivity is computed using one of the approaches (3.57-3.59) and (3.60).

The flow is treated as one dimensional for every spatial direction. This approach can lead to false diffusion. It is important only if the transport velocity is inclined relative to the computational grid and if there is a non-null gradient of the unknown parameter on the direction normal to the current line [17].

3.6   Discretization of the unsteady term

Generally, the time derivative can be discretized using a Lax-Wendroff scheme or a Runge-Kutta method. The first class of methods combines the discretization in time with the discretization in space. The method proves to be difficult to implement for multi-dimensional problems. The latter class of schemes are widely used due to their accuracy and easy implementation. Their inconvenience is related only to the storage requirements, which is direct proportional to the order of the method.

In the present study, the time derivative in equation (3.31) is approximated with a third order explicit Runge-Kutta scheme. The method belongs to the TVD (Total Variation Diminishing) high-order Runge-Kutta schemes, developed by Shu and Osher [77, 78] and Jiang and Shu [41].

The unsteady term has the total variation:

$$TV = \int \left| \frac{\partial c}{\partial t} \right| dt \tag{3.63}$$

Using an Euler forward first order scheme to discretize the derivative, the total vari-

ation condition in t of the numerical scheme is:

$$TV(c) = \sum_i |c_{i+1} - c_i| \tag{3.64}$$

The numerical scheme is TVD if:

$$TV(c^{n+1}) \leq TV(c^n) \tag{3.65}$$

The general Runge-Kutta schemes derived by Shu and Osher [77] are:

$$c^{(i)} = \sum_{k=0}^{i-1} \left[\alpha_{ik} c^{(k)} + \beta_{ik} \Delta t \, \text{CDT} \right], i = 1, 2, ..., m$$

$$c^{(0)} = c^{(n)}, \qquad\qquad c^{(m)} = c^{(n+1)}, \tag{3.66}$$

where CDT represents the convective and diffusive terms previously computed and α_{ik} and β_{ik} are constants. The schemes are TVD according to condition (3.65) under the CFL condition:

$$\lambda \leq \lambda_0 \min_{i,k} \frac{\alpha_{ik}}{|\beta_{ik}|} \tag{3.67}$$

For the third order TVD Runge-Kutta scheme, the CFL restriction is $\lambda = 1$ [77]. According to Shu and Osher, the "classical" third order Runge-Kutta scheme has a smaller CFL condition when considered in the form (3.66).

Considering the value of the concentration of species α at time level n, $c_{i,j,k}^{\alpha\,\text{m}\,(\text{n})}$, the value at the next time step is computed as follows:

$$c_{i,j,k}^{\alpha\,\text{m}\,(\text{n},1)} = c_{i,j,k}^{\alpha\,\text{m}\,(\text{n})} + \Delta t \, \text{CDT}(c_{i,j,k}^{\alpha\,\text{m}\,(\text{n})}, \mathbf{v}_{i,j,k}^{\text{m}\,(\text{n})})$$

$$c_{i,j,k}^{\alpha\,\text{m}\,(\text{n},2)} = \frac{3}{4} c_{i,j,k}^{\alpha\,\text{m}\,(\text{n})} + \frac{1}{4} c_{i,j,k}^{\alpha\,\text{m}\,(\text{n},1)} + \frac{1}{4} \Delta t \, \text{CDT}(c_{i,j,k}^{\alpha\,\text{m}\,(\text{n},1)}, \mathbf{v}_{i,j,k}^{(\text{n},1)}) \tag{3.68}$$

$$c_{i,j,k}^{\alpha\,\text{m}\,(\text{n}+1)} = \frac{1}{3} c_{i,j,k}^{\alpha\,\text{m}\,(\text{n})} + \frac{2}{3} c_{i,j,k}^{\alpha\,\text{m}\,(\text{n},2)} + \frac{2}{3} \Delta t \, \text{CDT}(c_{i,j,k}^{\alpha\,\text{m}\,(\text{n},2)}, \mathbf{v}_{i,j,k}^{(\text{n},2)}),$$

where $c_{i,j,k}^{\alpha\,\text{m}\,(\text{n},1)}$ and $c_{i,j,k}^{\alpha\,\text{m}\,(\text{n},2)}$ represent the intermediate values of the concentration.

The time step Δt is evaluated first from the stability criteria to ensure that no fluctuations will appear during the simulation.

3.7   Determination of the time step criteria

In order to ensure the stability of the numerical scheme, one can employ the von Neumann method, the method of the equivalent differential equation or the matrix method [17, 31].

For the time step size calculation `TURBIT-VoF` uses the minimum of four time step criteria, derived considering alone the convective, viscous, buoyancy and capillary forces [99].

Since the calculation of a time restriction is more difficult when both convection and diffusion are considered, one can obtain a time condition for each process considered separately. This imposes a more severe restriction for the time step, but increases the safety.

3.7.1 Maximum time step size for centered difference scheme

The unsteady convection-diffusion equation for an species having constant physical properties is:

$$\frac{\partial c_k^\alpha}{\partial t} + u_k \frac{\partial c_k^\alpha}{\partial x} + v_k \frac{\partial c_k^\alpha}{\partial y} + w_k \frac{\partial c_k^\alpha}{\partial z} = -\frac{D_k^\alpha}{\mathrm{Re}_{\mathrm{ref}} \cdot \mathrm{Sc}_{\mathrm{ref}}^\alpha} \left(\frac{\partial^2 c_k^\alpha}{\partial x^2} + \frac{\partial^2 c_k^\alpha}{\partial y^2} + \frac{\partial^2 c_k^\alpha}{\partial z^2} \right) \qquad (3.69)$$

Using the centered difference scheme to discretize the convective and diffusive terms and an Euler forward scheme for the unsteady term one obtains the concentration value at time step $n + 1$:

$$
\begin{aligned}
c_{i,j,k}^{\alpha\,(n+1)} = {}& c_{i,j,k}^{\alpha\,(n)} \\
& + \Delta t^\alpha \left\{ \left(u_{i,j,k}^{(n)} \frac{c_{i+1,j,k}^{\alpha\,(n)} - c_{i-1,j,k}^{\alpha\,(n)}}{2\Delta x} + v_{i,j,k}^{(n)} \frac{c_{i,j+1,k}^{\alpha\,(n)} - c_{i,j-1,k}^{\alpha\,(n)}}{2\Delta y} + w_{i,j,k}^{(n)} \frac{c_{i,j,k+1}^{\alpha\,(n)} - c_{i,j,k-1}^{\alpha\,(n)}}{2\Delta z} \right) \right. \\
& + \frac{D_{i,j,k}^\alpha}{\mathrm{Re}_{\mathrm{ref}} \cdot \mathrm{Sc}_{\mathrm{ref}}^\alpha} \left[\frac{c_{i+1,j,k}^{\alpha\,(n)} - 2c_{i,j,k}^{\alpha\,(n)} + c_{i-1,j,k}^{\alpha\,(n)}}{(\Delta x)^2} \right. \\
& \left. \left. + \frac{c_{i,j+1,k}^{\alpha\,(n)} - 2c_{i,j,k}^{\alpha\,(n)} + c_{i,j-1,k}^{\alpha\,(n)}}{(\Delta y)^2} + \frac{c_{i,j,k+1}^{\alpha\,(n)} - 2c_{i,j,k}^{\alpha\,(n)} + c_{i,j,k-1}^{\alpha\,(n)}}{(\Delta z)^2} \right] \right\}
\end{aligned}
$$
$$(3.70)$$

Applying the von Neumann method (see for more details [17, 20, 31]) for equation (3.70) one obtains the stability requirements:

$$\frac{D_{i,j,k}^\alpha}{\mathrm{Re}_{\mathrm{ref}} \cdot \mathrm{Sc}_{\mathrm{ref}}^\alpha} \Delta t^\alpha \left[\frac{1}{(\Delta x)^2} + \frac{1}{(\Delta y)^2} + \frac{1}{(\Delta z)^2} \right] \leq \frac{1}{2} \qquad (3.71)$$

$$\frac{\Delta t^\alpha}{D_{i,j,k}^\alpha} \left(u_{i,j,k}^2 + v_{i,j,k}^2 + w_{i,j,k}^2 \right) \leq 2 \qquad (3.72)$$

Hence the maximum time step that can be used for species α, under the assumption of uniform computational grid, is:

$$\Delta t^\alpha \leq \min \left[\frac{1}{6} \frac{(\Delta x)^2 \mathrm{Re}_{\mathrm{ref}} \mathrm{Sc}_{\mathrm{ref}}^\alpha}{\max\left(D_1^\alpha, D_2^\alpha\right)}, \frac{2 \min\left(D_1^\alpha, D_2^\alpha\right)}{u_{i,j,k}^2 + v_{i,j,k}^2 + w_{i,j,k}^2} \right] \qquad (3.73)$$

For this numerical discretization the correct stability condition can be written in terms of the grid ReSc^α product, which imposes the following limit [31]:

$$\mathrm{ReSc}^{\alpha}{}_{\mathrm{grid}} = \frac{a_{i,j,k}\Delta x}{\max\left(D_k^{\alpha}\right)} \leq \frac{2\,\Delta x}{a_{i,j,k}\,\Delta t}, \tag{3.74}$$

where the velocity $\mathrm{a}_{i,j,k} = \sqrt{u_{i,j,k}^2 + v_{i,j,k}^2 + w_{i,j,k}^2}$.

3.7.2   Maximum time step size for upwind scheme

Using a first order upwind scheme to discretize the convective term and the forward Euler scheme for the unsteady term, the concentration at time level $n + 1$ for an unsteady convection equation can be written for nonnegative $u_{i,j,k}^{\alpha\,(n)}$, $v_{i,j,k}^{\alpha\,(n)}$ and $w_{i,j,k}^{\alpha\,(n)}$ as follows:

$$
\begin{aligned}
c_{i,j,k}^{\alpha\,(n+1)} \;=\; & c_{i,j,k}^{\alpha\,(n)} \\
& - \Delta t^{\alpha}\left(u_{i,j,k}^{\alpha\,(n)}\frac{c_{i,j,k}^{\alpha\,(n)} - c_{i-1,j,k}^{\alpha\,(n)}}{\Delta x} + v_{i,j,k}^{\alpha\,(n)}\frac{c_{i,j,k}^{\alpha\,(n)} - c_{i,j-1,k}^{\alpha\,(n)}}{\Delta y} + w_{i,j,k}^{\alpha\,(n)}\frac{c_{i,j,k}^{\alpha\,(n)} - c_{i,j,k-1}^{\alpha\,(n)}}{\Delta z}\right)
\end{aligned}
\tag{3.75}
$$

Considering the von Neumann stability method one obtains the restriction for the time step:

$$\Delta t^{\alpha} < \frac{\mathrm{CFL}}{\dfrac{|u_{i,j,k}^{\alpha\,(n)}|}{\Delta x} + \dfrac{|v_{i,j,k}^{\alpha\,(n)}|}{\Delta y} + \dfrac{|w_{i,j,k}^{\alpha\,(n)}|}{\Delta z}} \tag{3.76}$$

where CFL represents the Courant-Friedrichs-Lewy condition. The numerical scheme is stable provided that $0 < \mathrm{CFL} \leq 1$.

3.8   Implementation of the boundary conditions

The molar mass flux at the wall is:

$$\mathrm{j}_{\mathrm{wall}} = \frac{\mathrm{D}^{\alpha}}{\mathrm{Re}_{\mathrm{ref}}\mathrm{Sc}_{\mathrm{ref}}^{\alpha}}\frac{\partial c^{\alpha}}{\partial z} = \frac{2D^{\alpha}}{\mathrm{Re}_{\mathrm{ref}}\mathrm{Sc}_{\mathrm{ref}}^{\alpha}}\frac{c_1^{\alpha} - c_{\mathrm{wall}}^{\alpha}}{\Delta z}, \tag{3.77}$$

where $c_{\mathrm{wall}}^{\alpha}$ represents the unknown concentration at the wall.

In `TURBIT-VoF` one can impose Dirichlet or Neumann boundary conditions. These conditions are grouped in one equation having the concentration and the mass flux weighted by appropriate coefficients.

$$\mathrm{a}_{\mathrm{wi}}\,c^{\alpha} - \mathrm{b}_{\mathrm{wi}}\frac{D^{\alpha}}{\mathrm{Re}_{\mathrm{ref}}\mathrm{Sc}_{\mathrm{ref}}}\frac{\partial c^{\alpha}}{\partial z} = \mathrm{c}_{\mathrm{wi}}, \tag{3.78}$$

where $\mathrm{i} = 1, 4$ represents the index of the walls. The weighting coefficients that have to be specified as input data are a_{wi}, b_{wi} and c_{wi}. Their significance is displayed in Table 3.2.

a_{wi}	b_{wi}	$c_{wi}(k)$	**Physical meaning**	**Mass flux**
0	1	0	Null mass flux	$j_{wall} = 0$
0	1	IF_{wi}	Imposed mass flux	$j_{wall} = IF_{wi}$
1	0	c_{wi}^α	Imposed concentration	$j_{wall} = \dfrac{2D^\alpha}{Re_{ref}Sc_{ref}^\alpha}\dfrac{c_1^\alpha - c_{wi}^\alpha}{\Delta z}$
$\neq 0$	$\neq 0$	c_{wi}	Mixed boundary condition	$j_{wall} = \dfrac{2D^\alpha a_{wi}}{Re_{ref}Sc_{ref}^\alpha}\dfrac{c_1^\alpha - c_{wi}^\alpha}{\Delta z} - b_{wi}c_{wi}^\alpha$

Table 3.2: Weighting coefficients for mass transfer boundary conditions

Using the above weighting coefficients, the mass transfer boundary condition (3.77) that is implemented in `TURBIT-VoF` is:

$$j_{wall} = \frac{2D^\alpha a_{wi}}{Re_{ref}Sc_{ref}^\alpha}\frac{c^\alpha - c_{wi}}{\Delta z} - b_{wi}c_{wi}, \qquad (3.79)$$

where c^α represents the concentration in the first cell for the left wall and the concentration in the last cell for the right wall.

Periodic boundary conditions have been implemented in axial direction for the concentration field. Since in the applications considered in section 5 the bubbles rise only a short distance, the choice for periodicity in stream-line direction is justified.

In case of first order heterogeneous chemical reaction, the mass flux at the wall is evaluated as follows:

$$j_{wall} = k_s^\alpha c_{wall}^\alpha, \qquad (3.80)$$

that is, the rate of species consumption at the wall is proportional to the species concentration at the wall. For an species that is consumed at the wall by an instantaneous chemical reaction, the concentration is assumed to be null, i.e. $c_{wall}^\alpha = 0$.

Chapter 4

Validation of the numerical method by test problems

This chapter considers the comparison between the diffusive, convective and source term from the species conservation equation (2.2) and appropriate analytical solutions published in literature. In the first section, the implementation of the diffusive term is validated against analytical solutions for simple one-dimensional and two-dimensional problems. In section 4.2 is presented the determination of the mass transfer coefficient. In the third section, the numerical simulation of mass transfer for a 4mm air bubble rising in a mixture of water and glycerol is compared against another numerical simulation that is available in literature. The fourth section presents comparisons between numerically and analytically obtained solutions for simple single phase problems of mass transfer with and without first order homogeneous and heterogeneous chemical reactions.

4.1 Validation of the diffusion term

4.1.1 One dimensional case

Analytical solution

In order to verify the implementation of the diffusive term, a simple one-dimensional problem of mass transfer has been considered, for which an analytical solution is proposed by Crank [10]. A system consisting of two stagnant media separated by an immobile interface is considered, as sketched in Figure 4.1. Since `TURBIT-VoF` is a three-dimensional code, the geometry of the study has to be also three-dimensional. Nevertheless, the mass transfer, which occurs only by diffusion, is computed only in one direction, namely along x axis. Fluid 1, situated in the left side of the interface has null initial concentration, while fluid 2, situated in the right side of the interface, has an initial non-dimensional concentration $c_0 = 1$. Local equilibrium is assumed to be established instantaneously at the interface.

(a)
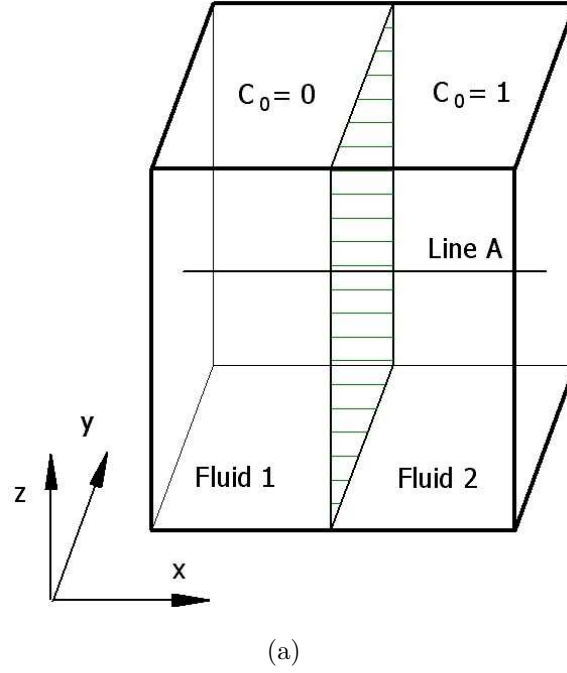
Figure 4.1:   Geometry for diffusion study in one-dimensional case

The concentration distribution is described by the analytical solution:

$$
\begin{aligned}
c_G^\star &= \frac{c_0^\star}{1 + H\sqrt{D_L^\star/D_G^\star}} \left[1 + H\sqrt{D_L^\star/D_G^\star}\, \mathrm{erf}\left(\frac{x^\star}{2\sqrt{D_G^\star t^\star}} \right) \right] \\
c_L^\star &= \frac{Hc_0^\star}{1 + H\sqrt{D_L^\star/D_G^\star}} \left[1 - H\sqrt{D_L^\star/D_G^\star}\, \mathrm{erfc}\left(\frac{|x^\star|}{2\sqrt{D_L^\star t^\star}} \right) \right]
\end{aligned} \tag{4.1}
$$

where $H = c_L^\star/c_G^\star$ represents the local equilibrium expression similar to Henry's law (2.9).

As diffusion proceeds in time, the interfacial concentrations remain constant on both sides of the interface, i.e. for $x \to 0$:

$$
\begin{aligned}
c_G^\star &= \frac{c_0^\star}{1 + H\sqrt{D_L^\star/D_G^\star}} \\
c_L^\star &= \frac{Hc_0^\star}{1 + H\sqrt{D_L^\star/D_G^\star}}
\end{aligned} \tag{4.2}
$$

Since `TURBIT-VoF` uses dimensionless parameters, relations (4.1) have to be employed in a dimensionless form. Introducing relations (3.5) and (3.7) in (4.1) will lead to the non-

dimensional analytical concentration distribution:

$$
\begin{aligned}
\frac{c_G^\star}{c_0^\star} &= \frac{1}{1 + H\sqrt{D_L/D_G}} \left[1 + H\sqrt{D_L/D_G}\, \mathrm{erf}\left(\frac{x}{2\sqrt{D_G t}} \sqrt{\mathrm{Re}_{\mathrm{ref}}\,\mathrm{Sc}_{\mathrm{ref}}} \right) \right] \\
\frac{c_L^\star}{c_0^\star} &= \frac{H}{1 + H\sqrt{D_L/D_G}} \left[1 - H\sqrt{D_L/D_G}\, \mathrm{erfc}\left(\frac{|x|}{2\sqrt{D_L t}} \sqrt{\mathrm{Re}_{\mathrm{ref}}\,\mathrm{Sc}_{\mathrm{ref}}} \right) \right]
\end{aligned}
\tag{4.3}
$$

A stand alone program has been made to evaluate the analytical solution. Appendix C presents the influence of the number of nodes used for the discrete representation of the concentration distribution on the accuracy of the interfacial concentration jump representation. In order to obtain constant interfacial concentrations, as described by equations (4.2), a large number of nodes is required. Otherwise, at the beginning of the computation, when the mass fluxes are large, the interfacial concentration jump is not sufficiently accurate captured. The analytical solution is displayed using 100 equally displaced nodes, except where explicitly mentioned (i.e. 50 000 nodes). The error function appearing in the analytical solution (4.1) has been adapted to the program using subroutines available online at http://iris-lee3.ece.uiuc.edu/~jjin/routines/routines.html.

Results

In order to visualize the concentration profile obtained with `TURBIT-VoF`, the concentration field is transformed back to the physical field using the inverse of the transformation (2.16).

The numerical tests performed evaluate the influence of diffusivities ratio, Henry number, grid resolution and the interface position relative to a grid cell on the analytical and numerical solution.

For the numerical solution computed with `TURBIT-VoF` the grid employed is discretized by 100 cells in the direction of mass transfer and 10 cells in the other directions. For case 8b a finer grid, i.e. 10 x 10 x 200, has been employed. The reference and input parameters used for the numerical simulation are displayed in Table 4.1.

$\rho_2^\star/\rho_1^\star$	$\mu_2^\star/\mu_1^\star$	$l_{\mathrm{ref}}^\star$ [m]	$v_{\mathrm{ref}}^\star$ [m/s]	$g_{\mathrm{ref}}^\star$ [m^2/s]	$\mathrm{Re}_{\mathrm{ref}}$	$\mathrm{We}_{\mathrm{ref}}$	$\mathrm{Sc}_{\mathrm{ref}}^\alpha$	$\Delta t^\star$ / $t_{\mathrm{ref}}^\star$
0.5	1	3.2	1	0	20	10^{-5}	1	10^{-5}

Table 4.1: Reference parameters for the numerical simulation

The numerical tests performed are presented in Table 4.2. All tests are performed for grids containing the interface between cells as displayed in Figure 4.2a and in a certain cell as presented in Figure 4.2b. The concentration profiles obtained analytically and numerically are presented in Appendix D. The analytic solution has been displayed with a red continuous curve while the numerical solution obtained with `TURBIT-VoF` is displayed by a curve consisting of black dots. As expected, the agreement between the numerical and analytical solutions decreases for the cases of interface inside cells. This is a consequence of
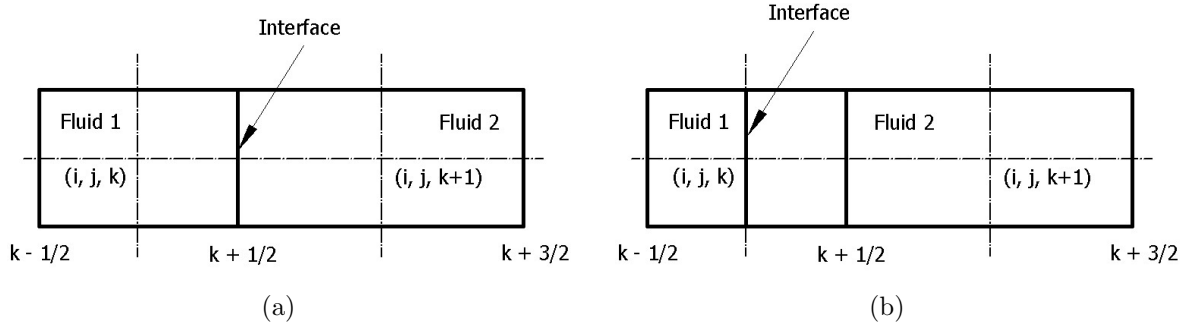
Figure 4.2: a) Interface placed at the border of the cell b) Interface placed in the center of the cell

Test	D_2/D_1	H	Interface position	Figure
1	1	1	At cell border / Inside cell	D.1
2	10	1	At cell border / Inside cell	D.2
3	1	5	At cell border / Inside cell	D.3
4	10	15	Inside cell	D.4
5	10	0.5	Inside cell	D.5
6	10	5	Inside cell	D.6
7	30	5	Inside cell	D.7

Table 4.2: Numerical tests for diffusion term

the approximations introduced when considering the geometrical position of the interface by means of the liquid volumetric fraction.

For the very simple first test very good agreement is obtained. The numerical solution is independent of the interface position within the cell. Test 2 and 7 are designated to verify the influence of the ratio of the diffusivities on the concentration profile. Increasing the ratio of the diffusivities leads to an increase of the molecular motion in the fluid. Therefore more amounts of mass can arrive at the interface enhancing the mass transfer. It can be observed that, for case 2, the concentrations at the interface can be evaluated using the analytical solution (4.2):

$$c_G^\star = c_L^\star \simeq 0.76 \, \text{mol/m}^3, \tag{4.4}$$

The agreement with the interfacial concentrations obtained numerically and displayed in Figure D.2 is very good.

Tests 3, 4 and 5 are considered to study the influence of the Henry number on the mass transfer. For the systems having $H > 1$, the interface position within a mesh cell becomes important for discontinuous concentration fields, as can be seen in Figure D.3. Very good agreement is found for the particular case of interface placed between cells, while for the case of interface placed within the cell, the numerical solution overestimates the in-

terfacial concentration field. From the tests performed it is found that this overestimation is proportional to the Henry number H^α. The overestimation of the concentration field on both sides of the interface is a consequence of unavoidable numerical errors encountered in evaluating the mass flux at the interface. The concentration in cells containing interfaces is computed as a mean between the concentration in the liquid and gas phase, as described by equation (3.27). Therefore, at interface, the concentration gradient evaluated numerically is always smaller then the real concentration gradient. This leads to a decrease in the amount of mass which is transferred from the dispersed phase to the continuous one in comparison with the real system. As a consequence, on the dispersed side of the interface, the concentration field evaluated numerically has a larger value than the analytical solution. The overestimation of the concentration field in the dispersed phase leads to an overestimation of the analytical solution also in the continuous phase, even if the transferred amount of mass is smaller than in real systems.

Henry number H^α is direct proportional to the mass flux towards the solvent. For large values of H^α significant differences between the maximum and the minimum concentrations within the concentration boundary layer on each side of the interface are encountered. For such systems, a fine grid is needed to capture the concentration gradient within the concentration boundary layer. As mass transfer proceeds, the differences between the analytical and numerical solution tend to decrease as a consequence of the decreasing mass flux. This tendency can be observed in test 4, i.e. Figure D.4.

In case of $H < 1$, only a small amount of mass has to be transferred in the continuous phase, for the system to reach equilibrium. Therefore, the mass flux at the interface is also small and can be accurately evaluated. As a result, the analytical and numerical solutions agree very well, as can be seen in Figure D.5.

In test 6, the same mass transfer problem is computed on a coarse grid consisting of 100 cells in mass transfer direction (Figure D.6 a, c, e) and a grid consisting of 200 cells (Figure D.6 b, d, f). Examining the numerical profiles obtained one can observe that the concentration boundary layer produced by the interfacial concentration jump is better captured numerically with the fine grid. A smaller time step, i.e. $\Delta t^\star / t_{\text{ref}}^\star = 10^{-6}$, has been used for simulations employing a fine grid, due to the time step restrain (3.73).

Theoretical and numerical solution agree very well for all cases when the interface is placed at the border of the cell. For this reason the simulations performed for these cases employed coarse grids for both solutions (i.e. grid 10 x 10 x 100).

As the ratio of the diffusivities increases for systems with $H > 1$, the numerical solution underestimates the concentration field in the continuous phase, as can be seen in Figure D.7. For such a system, the mass flux across the interface is fostered by the increase of the ratio of diffusivities. Examining the formulas for the cell face diffusivity, one can conclude that the increase in the diffusive flux is underestimated by the mean diffusivity computed. Table 4.3 displays the cell face mean diffusivity D^{m}, between two neighboring cells containing different phases. One can observe that increasing the ratio of the diffusivities $D_2^\star/D_1^\star$ by a factor of 10, leads to a much smaller increase in the cell face mean diffusivity that is used at interface. The calculations for the interfacial diffusivity D^{m} have been performed with equation (3.57), considering the geometry in Figure 4.2a

Henry number	$D^{\mathrm{m}}[-]$ $(D_2^\star/D_1^\star=100)$	$D^{\mathrm{m}}[-]$ $(D_2^\star/D_1^\star = 1000)$	$D^{\mathrm{m}}_{D_2^\star/D_1^\star=1000}/D^{\mathrm{m}}_{D_2^\star/D_1^\star=100}[-]$
0.5	9.95 x 10^{-9}	9.99 x 10^{-9}	1.004
20	8.33 x 10^{-9}	9.80 x 10^{-9}	1.176
100	5.00 x 10^{-9}	9.09 x 10^{-9}	1.818

Table 4.3: Test of the cell face mean diffusivity D^{m}

(a)   (b)
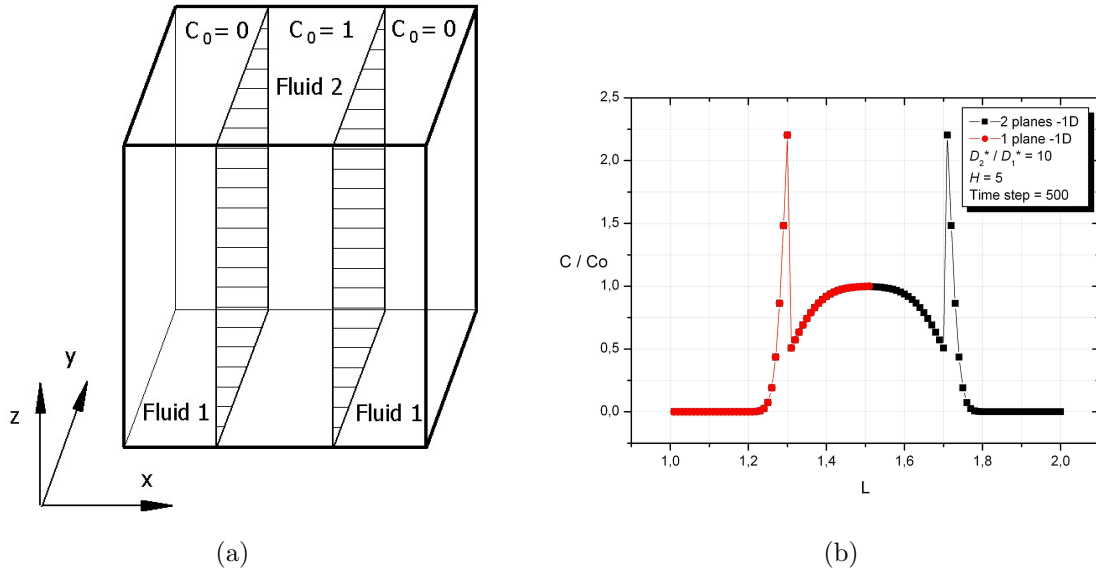
Figure 4.3: a) Two parallel planes test geometry b) Numerical concentration profiles for one and two parallel planes ($D_2^\star/D_1^\star = 10$, $H = 5$)

and $D_1^\star = 5 \times 10^{-9}\,\mathrm{m^2/s}$.

Before considering two-dimensional diffusion, another test, employing two parallel planes as displayed in Figure 4.3a, has been performed. The gas phase is considered between planes, surrounded by liquid phase. Since the planes are placed symmetrical with respect to domain's center, a symmetrical concentration profile is also obtained. Figure 4.3b represents the concentration profile plotted against the numerical profile obtained for single plane.

Two formulas have been implemented for evaluating the diffusivity at the cell face. The first one is expressed by equation (3.57), which is the modified approach of Patankar [59], while the second equation (3.60) is the modified formula proposed by Davidson and Rudman [14]. A comparison of the concentration field obtained using these approaches is presented in Figures 4.4 for a system with $D_2^\star/D_1^\star = 30, H = 5$ and in Figure 4.5 for a system with $D_2^\star/D_1^\star = 10, H = 15$. Table 4.4 displays the ratio of interfacial concentrations determined for each case. No significant differences are observed in the evaluated

concentration field. This conclusion supports the fact that an accurate representation of the mass flux across interface proves to be more important than the formulation of the cell face diffusivity [59].

(a)

(b)

Figure 4.4: Concentration field evaluated using modified formulas of Patankar [59] - equation (3.57) and Davidson and Rudman [14] - equation (3.60) at time step 500 (a) and 1000 (b) - $D_2^\star / D_1^\star = 30$, $H = 5$
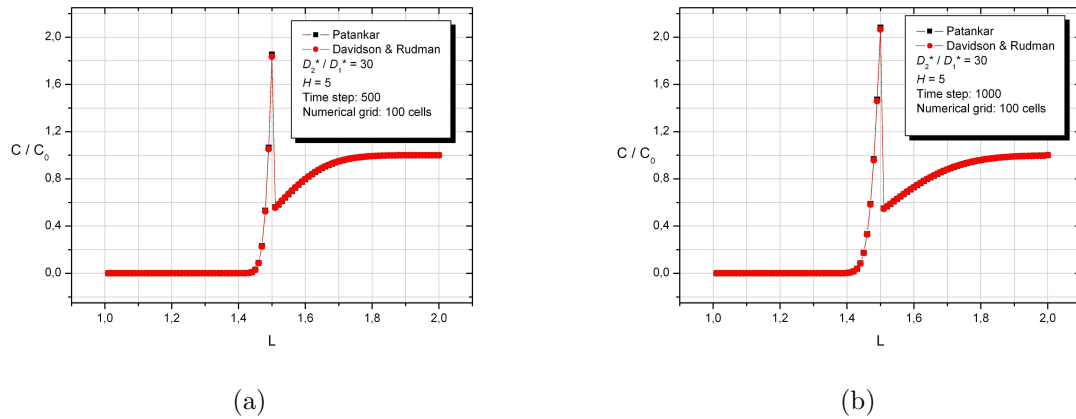

(a)

(b)
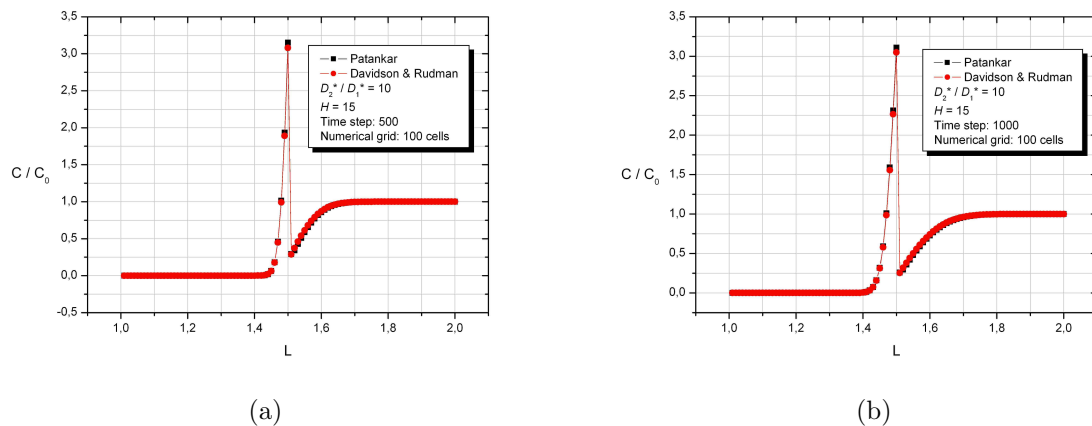
Figure 4.5: Concentration field evaluated using modified formulas of Patankar [59] - equation (3.57) and Davidson and Rudman [14] - equation (3.60) at time step 500 (a) and 1000 (b) - $D_2^\star / D_1^\star = 10$, $H = 15$

	$D_2^\star/D_1^\star = 30, H = 5$		$D_2^\star/D_1^\star = 10, H = 15$	
Time step	**Eq. (3.57)**	**Eq. (3.60)**	**Eq. (3.57)**	**Eq. (3.60)**
500	3.31	3.30	10.77	10.76
1000	3.79	3.78	12.01	12.00
3000	4.29	4.29	13.19	13.18

Table 4.4: Concentration jump at interface determined with the modified formulas of Patankar [59] - equation (3.57) and Davidson and Rudman [14] - equation (3.60)

4.1.2 Two dimensional case

For the two dimensional benchmark test, the numerical concentration field obtained with computer code `TURBIT-VoF` is compared against an analytical solution presented by Bothe et al. [7]. Since `TURBIT-VoF` is a three-dimensional code the geometry of the study is considered in a three dimensional space, as in the previous section. The mass transfer process is computed in two-dimensions, i.e. only along x and z axis. Therefore the concentration field at any y plane is the same. The geometry of the study consists of a cylinder filled with gas 2, which is placed in the center of a cube filled with liquid 1, as displayed in Figure 4.6. The species considered diffuses radially from the cylinder into the surrounding fluid. The cylinder has a diameter of 3.2 cm, while the side length of the cube is 12.8 cm. The initial non-dimensional concentration in the cylinder is $c_0 = 1$, while the initial concentration in the surrounding liquid is zero. Both fluids are stagnant and mass transfer occurs only by diffusion. The reference quantities used in the simulations are presented in Table 4.5.

$l_{\text{ref}}^\star[\text{m}]$	$v_{\text{ref}}^\star$ [m/s]	$g_{\text{ref}}^\star$ [m^2/s]	Re$_{\text{ref}}$	Sc$_{\text{ref}}^\alpha$	D$_{\text{ref}}^{\alpha\star}$[m^2/s]	$\Delta t^\star/t_{\text{ref}}^\star$
0.128	1	0	1280	1	0.0001	10^{-4}

Table 4.5: Reference parameters for the 2D numerical simulation of mass transfer

Considering the dimensionless values in Table 4.5 the product of Re$_{\text{ref}}$ and Sc$_{\text{ref}}^\alpha$ becomes:

$$\text{Re}_{\text{ref}} \cdot \text{Sc}_{\text{ref}}^\alpha = \frac{l_{\text{ref}}^\star v_{\text{ref}}^\star}{D_{\text{ref}}^{\alpha\star}} = 1280 \tag{4.5}$$

The maximum time step size has been computed using relation (3.73). Two grids have been employed in the simulations performed with `TURBIT-VoF`, function of the need to accurately capture the concentration field at interface. The reference grid consists of 100 x 4 x 100 cells, while the refined grid consists of 200 x 4 x 200 cells. The parameters used for the tests are presented in Table 4.6. Tests $1 \div 3$ are performed to study the influence of the diffusivity ratio $D_2^\star/D_1^\star$ on the numerical solution. The following two tests investigate the influence of the Henry number H^α on the numerical solution.

The concentration field obtained along the center of the cylinder (line A in Figure 4.6) is displayed in Figures 4.7 and D.8 ÷ D.10. The numerical solution is represented by a curve formed with black dots, while the analytical solution is represented by a red continuous curve.
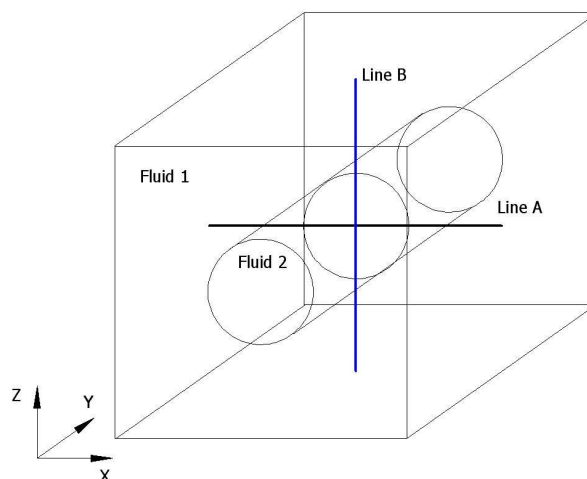
Figure 4.6: Geometry for diffusion study in two-dimensional case

Test	$D_2^\star/D_1^\star$	H	**Figure**
1	10	5	4.7
2	30	5	D.8 a, b
3	100	5	D.8 c, d
4	10	15	D.9
5	10	0.5	D.10

Table 4.6: Numerical tests for the two-dimensional diffusion problem

In Figures 4.7 the numerical solution obtained with `TURBIT-VoF` is compared against the analytical solution, for a system with $H = 5$ and $D_2^\star/D_1^\star = 10$. The purpose is to study the influence of the mesh cell size on the accuracy of the numerical solution. Two grids have been employed for the numerical solution, namely 100 x 4 x 100 (Figure 4.7 a, b) and 200 x 4 x 200 (Figure 4.7 c, d). The numerical solution overestimates the analytical solution for the concentration field within the dispersed phase and underestimates the analytical solution in the continuous phase side. One can observe the better agreement between the solutions in case of refined grid.

As for the one-dimensional diffusion problem discussed in the previous section, the increase in the ratio of the diffusivities $D_2^\star/D_1^\star$ leads to an underestimation of the analytical solution in the continuous phase. At the interface, for large values of the diffusivities

ratio $D_2^\star/D_1^\star$, the diffusive flux computed numerically is smaller than the physical molar flux. This is a consequence of the fact that the mean interfacial diffusivity is much smaller than $D_2^\star/D_1^\star$, as shown in the previous section. Also, the concentration gradient that is numerically evaluated in the interfacial molar flux is smaller than the physical interfacial concentration gradient. The reason is that the difference between the interfacial mean concentration, which are used to compute numerically the interfacial diffusive flux, is smaller than the difference between the real interfacial concentrations. A fine grid is needed to accurately capture the concentration boundary layer developing on each side of the interface. If the concentration boundary layer is not sufficiently resolved in the dispersed phase, the numerical errors introduced by the approximations used, lead in time to an accumulation of errors within the dispersed phase. As a consequence, the numerical solution overestimates the analytical solution throughout the entire dispersed phase.
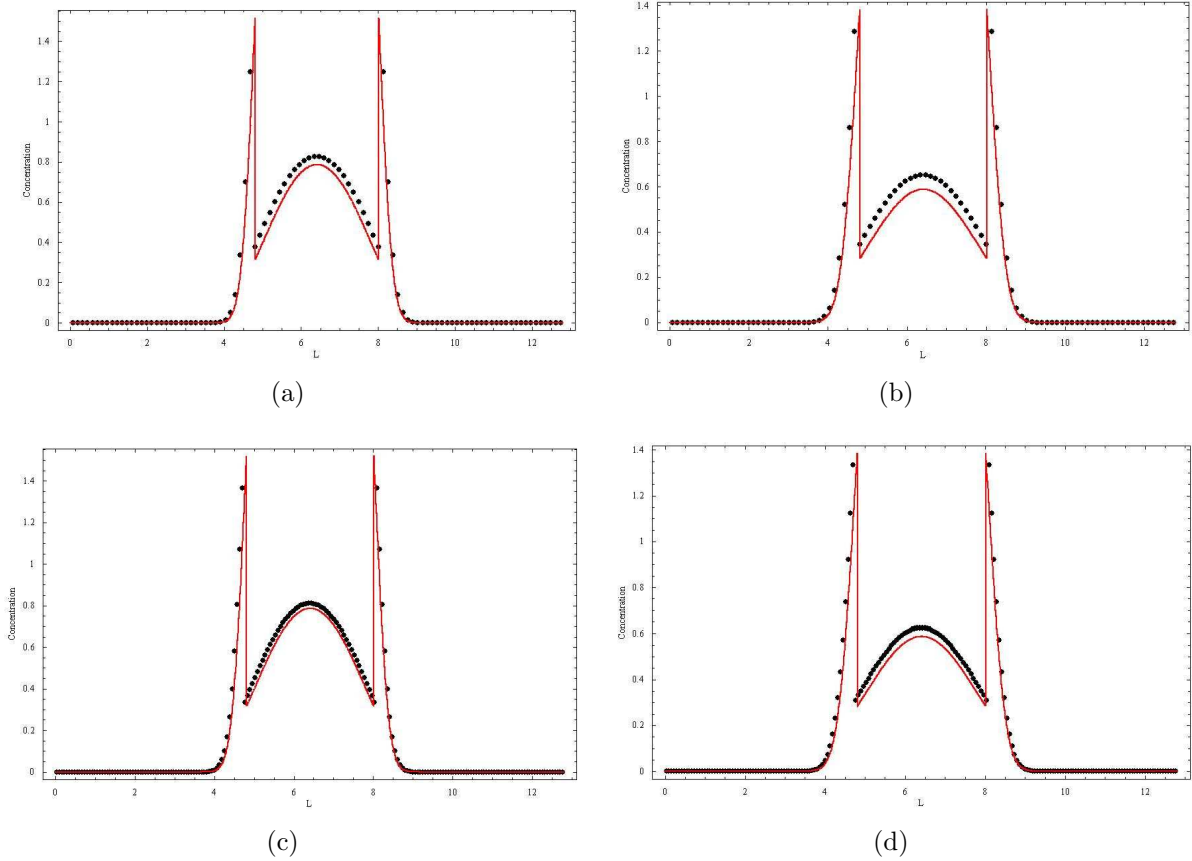
Figure 4.7: Numerical and analytical concentration profiles at time step 3000 (a, c) and 5000 (b, d) for system $D_2^\star/D_1^\star = 10$, $H = 5$ - grid 100 x 4 x 100 (a, b), grid 200 x 4 x 200 (c, d)

Therefore, for systems having large values of the diffusivities ratio $D_2^\star/D_1^\star$, at the initial stage of the numerical simulation, less mass is transferred to the continuous phase

than in the real system. This behavior explains the underestimation of the analytical solution in the continuous phase and the overestimation of the analytical solution in the dispersed phase.

Inspecting the Figures 4.7 and D.8 one can observe that the differences between the analytical and numerical solutions tend to approach a constant, as the ratio of the diffusivities increases.

The influence of the Henry number on the concentration field is displayed in Figures 4.7, D.9 and D.10. Similar to the one-dimensional case, at large values of the Henry number, a refined grid is required to accurately compute the large mass fluxes at the interface. For large values of the Henry number H, the amount of mass transferred in the continuous phase is smaller than in real systems. As can be seen in Table 4.3, increasing the Henry number H leads to a decrease of the mean interfacial diffusivity. The concentration gradient in both diffusive and convective term is computed using mean concentrations, defined by relation (3.27). Therefore, at interface, the concentration gradient computed numerically is always smaller than the real concentration gradient.

If the concentration boundary layer in the dispersed phase is not resolved, an accumulation of the errors occurs in time, as in the case of increased diffusivity ratio, leading to an overestimation of the analytical solution within the entire bubble. This leads also to an overestimation of the analytical solution on the liquid side of the interface.

Very good agreement is found in case of $H < 1$, as can be seen in Figure D.10. The small interfacial mass flux developed for this case is accurately captured even with a coarse grid.

The differences between the analytical and numerical solution appear at the initial stage of simulation, when the concentration gradient is large. As the mass is further transferred, the mass flux decreases leading to a increase in the agreement between the analytical and numerical solution.

4.2   Calculation of the mass transfer coefficient

According to Cussler [11] there are two mathematical models that can describe the diffusion. The most encountered model, largely known as Fick's law of diffusion (2.5), uses a diffusion coefficient. The second model uses a mass transfer coefficient and it is based on the assumption that the interfacial molar flux is proportional to the concentration of the solute:

$$\text{Molar flux}^{\alpha\star} = k_L^\star \cdot \Delta^\star c^{\alpha\star}, \tag{4.6}$$

where the mass transfer coefficient $k_L^\star$ is time dependent. The interfacial molar flux is defined as [11]:

$$\text{Molar flux}^{\alpha\star} = \frac{N^{\alpha\star}}{A^\star \cdot \Delta t^\star}, \tag{4.7}$$

where $N^{\alpha\star}$ represents the number of moles transferred in the continuous phase through the interfacial area $A^\star$ and time period $\Delta t^\star$.

Based on relations (4.6) and (4.7) the mass transfer coefficient can be defined in the following way:

$$k_L^\star(t) = \frac{\dot{N}^{\alpha\star}(t^\star)}{A^\star \cdot \Delta^\star c^{\alpha\star}}, \tag{4.8}$$

where $\dot{N}(t)^{\alpha\star}$ represents the number of moles transferred in the continuous phase in the time interval $\Delta t^\star$. In case of mass transfer without chemical reactions the mass is conserved and the number of moles that have left the continuous phase in a time period $\Delta t^\star$ is equal to the number of moles that have been transferred to the dispersed phase in the same time interval:

$$\dot{N}_L^{\alpha\star}(t) = \frac{N_L^{\alpha\star}(t^\star) - N_L^{\alpha\star}(t^\star - \Delta t^\star)}{\Delta t^\star} = \dot{N}^{\alpha\star}(t) = \frac{\mathrm{abs}\left(N_G^{\alpha\star}(t^\star) - N_G^{\alpha\star}(t^\star - \Delta t^\star)\right)}{\Delta t^\star} = \dot{N}_G^{\alpha\star}(t), \tag{4.9}$$

where $N_L^{\alpha\star}(t^\star)$ and $N_G^{\alpha\star}(t^\star)$ are the number of moles in the continuous and dispersed phase at time level $t^\star$.

Often, the bulk concentrations are used to define the driving concentration difference $\Delta^\star c^{\alpha\star}$ [9] in definition (4.8). Such an approach seems unappropriate for mass transfer studies in enclosed systems where the bulk concentrations are difficult to be defined. Also, the bulk concentrations cannot be used directly with a mass transfer coefficient to describe the rate of interphase mass transfer, since these two concentrations are differently related to the chemical potential, the real driving force of the process [82]. The concentration at the interface is also frequently used to define the driving concentration gradient [57]. The disadvantage of this approach is related to the difficulty in evaluating these quantities. In order to by-pass these drawbacks, we related the overall concentration gradient as follows:

$$\Delta^\star c^{\alpha\star} = \frac{c_G^{\alpha\,\mathrm{av}\,\star}}{H^\alpha} - c_L^{\alpha\,\mathrm{av}\,\star}, \tag{4.10}$$

Defined in this way, the concentration gradient becomes null when equilibrium is encountered in the system even when the concentration field presents a jump at the interface. In the above relation $c_G^{\alpha\,\mathrm{av}\,\star}$ and $c_L^{\alpha\,\mathrm{av}\,\star}$ represents the volumetric averaged concentrations in the dispersed and continuous phase:

$$c_G^{\alpha\,\mathrm{av}\,\star} = \frac{\sum_i^{\mathrm{NC}_G} c_G^{\alpha\star}}{\mathrm{NC}_G} \qquad\qquad c_L^{\alpha\,\mathrm{av}\,\star} = \frac{\sum_i^{\mathrm{NC}_L} c_L^{\alpha\star}}{\mathrm{NC}_L}, \tag{4.11}$$

where NC_G and NC_L represent the number of cells containing only the dispersed and respectively the continuous phase. Based on relations (4.11) the number of moles in the liquid phase, $N_L^{\alpha\star}$, and in the gas phase, $N_G^{\alpha\star}$, are determined as follows:

$$N_L^{\alpha\star} = c_L^{\alpha\,\mathrm{av}\,\star}(1 - \varepsilon)V^\star \qquad\qquad N_G^{\alpha\star} = c_G^{\alpha\,\mathrm{av}\,\star}\varepsilon V^\star, \tag{4.12}$$

where $V^\star$ represents the volume of the computational domain.

Considering the equations (4.8 ÷ 4.12) the dimensional overall mass transfer coefficient that can be determined using the data obtained with the code `TURBIT-VoF` is:

$$k_L^{\alpha\,\star}(t^\star) = \frac{\left[c_L^{\alpha\,\mathrm{av}\,\star}(t^\star) - c_L^{\alpha\,\mathrm{av}\,\star}(t^\star - \Delta t^\star)\right](1-\varepsilon)V^\star}{A^\star \Delta t^\star} \frac{1}{\dfrac{c_G^{\alpha\,\mathrm{av}\,\star}(t^\star)}{H^\alpha} - c_L^{\alpha\,\mathrm{av}\,\star}(t^\star)} \tag{4.13}$$

The above formulation of the mass transfer coefficient is compared in section 5.2 against the mass transfer coefficient (E.11), which is derived in Appendix E.

Based on the definition (4.13) of the mass transfer coefficient one can define the Sherwood number [75, 76] as follows:

$$\mathrm{Sh}(t^\star) = \frac{k_L^{\alpha\,\star}(t^\star)l^\star}{D^\star} \tag{4.14}$$

The Fourier number is defined as:

$$\mathrm{Fo}(t^\star) = \frac{D^\star t^\star}{l^{\star\,2}}, \tag{4.15}$$

Notice that for systems having $H > 1$, the concentration in the gas can be smaller than the one in the liquid, while the mass transfer is still from the gas phase to the liquid phase. This particular situation can lead to negative concentration gradient $\Delta c^{\alpha\,\mathrm{av}\,\star} = c_G^{\alpha\,\mathrm{av}\,\star}(t^\star)/H^\alpha - c_L^{\alpha\,\mathrm{av}\,\star}(t^\star) < 0$, as presented in Figure 4.8a. In order to avoid such situations and to maintain the positivity of the concentration gradient, for systems having $H > 1$, the quantity $\mathrm{AQ} = \left[c_G^{\alpha\,\mathrm{av}\,\star}(0)/H^\alpha - c_L^{\alpha\,\mathrm{av}\,\star}(0)\right] - \left[c_G^{\alpha\,\mathrm{av}\,\star}(t_{\mathrm{last}}^\star)/H^\alpha - c_L^{\alpha\,\mathrm{av}\,\star}(t_{\mathrm{last}}^\star)\right]$, where $t_{\mathrm{last}}^\star$ represents the total time considered, is added to the concentration gradient $\Delta c^{\alpha\,\mathrm{av}\,\star}$ in the mass transfer coefficient (4.13) and to the nominator as well as to the denominator of the logarithm in formula (E.11). Figure 4.8 displays the concentration gradient before (a) and after (b) adding quantity AQ.

(a)   (b)
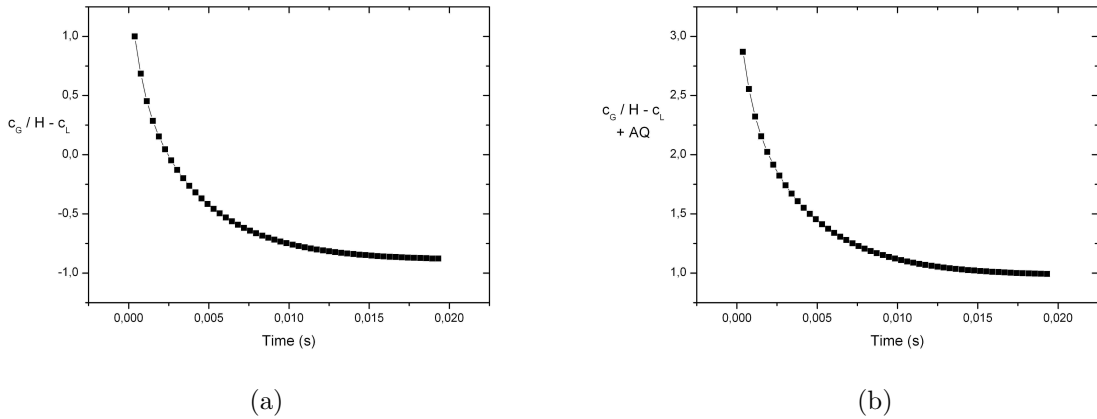
Figure 4.8: Concentration gradient $\Delta c^{\alpha\,\mathrm{av}\,\star} = c_G^{\alpha\,\mathrm{av}\,\star}(t^\star)/H^\alpha - c_L^{\alpha\,\mathrm{av}\,\star}(t^\star)$ before (a) and after (b) adding quantity AQ

4.3 Validation of the convective term

4.3.1 Mass transfer in single-phase flows

The case of mass transfer from a solid boundary into an adjoining fully developed laminar flow is considered by Apelblat [3]. A sketch of the hydrodynamics and a description of the mass transfer problem is illustrated in Figure 4.9. The solid boundary has a constant concentration c_0. The fluid is moving with a constant velocity u_0. At steady-state, neglecting diffusion in the flow direction, the problem considered is governed by the following partial differential equation:

$$u_0^\star \frac{\partial c^\star}{\partial x^\star} = D^\star \frac{\partial^2 c^\star}{\partial y^{\star 2}}, \tag{4.16}$$

subject to the boundary conditions:

$$\begin{aligned} c^\star = 0, \quad & x^\star = 0 \quad y^\star > 0 \\ c^\star = c_0^\star, \quad & x^\star \geq 0 \quad y^\star = 0 \end{aligned} \tag{4.17}$$

The analytical solution of the problem is [3]:

$$\frac{c^\star(X^\star, Y^\star)}{c_0^\star} = 1 - \mathrm{erf}\left(\frac{Y^\star}{2\sqrt{X^\star}}\right), \tag{4.18}$$

where

$$X^\star = x^\star / u_0^\star \qquad\qquad Y^\star = y^\star / \sqrt{D^\star} \tag{4.19}$$

Since `TURBIT-VoF` computes the non-dimensional concentration field, the solution (4.18) has been calculated also in a non-dimensional form.

$l_{\mathrm{ref}}^\star$[m]	$v_{\mathrm{ref}}^\star$ [m/s]	$g_{\mathrm{ref}}^\star$ [m^2/s]	$D_{\mathrm{ref}}^{\alpha\star}$[m^2/s]	$\Delta t^\star / t_{\mathrm{ref}}^\star$
1	1	0	1	10^{-4}

Table 4.7: Reference parameters for the numerical simulation of mass transfer in single-phase flow

Using relations (3.4), (3.5), (3.7) and the reference parameters in Table 4.7 the non-dimensional form of the analytical solution (4.18) becomes:

$$\frac{c(x,y)}{c_0} = 1 - \mathrm{erf}\left(\frac{y/\sqrt{D}}{2\sqrt{x/u_0}}\sqrt{\mathrm{Re}_{\mathrm{ref}}\mathrm{Sc}_{\mathrm{ref}}}\right) \tag{4.20}$$

The analytical solution (4.18) is expressed in terms of parameters $X^\star$ and $Y^\star$. In order to obtain the analytical solution in a non-dimensional form that is directly comparable
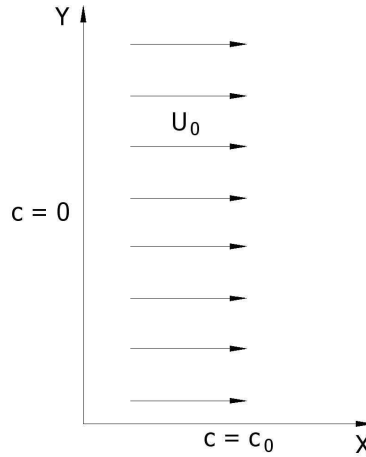
Figure 4.9: Flow hydrodynamics for the pure mass transfer problem

with the solution computed with `TURBIT-VoF`, the fluid velocity $u_0^\star$ and diffusivity $D^\star$ were considered unity. The effect of the velocity and of the diffusivity was studied by modifying the reference Reynolds and Schmidt parameters $\mathrm{Re}_{\mathrm{ref}}$ and $\mathrm{Sc}_{\mathrm{ref}}$, as displayed in Table 4.8.

`TURBIT-VoF` uses the no-slip condition for the velocity at the wall, while the analytical solution considers an uniform flow at wall. In order to obtain a consistent comparison for the velocity field, the first row of cells close to the wall was not considered in the evaluation of the numerical results. In order to fulfill the boundary condition (4.17), at the first row of cells close to the wall, i.e. at $y^\star = 0$, the concentration was held constant at $c^\star = c_0^\star$.

Non-periodic boundary conditions for the concentration field have been used for the numerical solution. At the inlet, the concentration was held constant at $c_{\mathrm{in}} = 0$, while at the outlet, first-order extrapolated boundary condition has been used for the concentration:

$$c_{\mathrm{out}} = 2c_{\mathrm{km}} - c_{\mathrm{km}-1}, \tag{4.21}$$

where `km` represents the last cell at the outlet.

Reynolds nr.	Schmidt nr.	Figure
100	0.1	4.10
300	0.1	4.11 a ÷ c
100	1.0	4.11 d ÷ f

Table 4.8: Reference Reynolds and Schmidt numbers

The non-dimensional concentration fields obtained analytically and numerically for the case with $\mathrm{Re}_{\mathrm{ref}} = 100$ and $\mathrm{Sc}_{\mathrm{ref}} = 0.1$ are displayed in Figure 4.10. One can observe the

excellent agreement between the solutions in Figure 4.10c, where the concentration isolines are displayed.

As the Re_{ref} and Sc_{ref} are increased the concentration boundary layer becomes thinner. This is the result of the increasing role of convection for the first case and of decreasing influence of diffusion in the latter case. For small values of the product $Re_{ref}Sc_{ref}$, when diffusion dominates, the numerical solution will not be able to capture the entire concentration field. The boundary conditions used for the upper wall in the numerical simulation will affect the flow. For very high values of Re_{ref} or Sc_{ref}, when convection dominates, the boundary layer is very thin and a large grid resolution is needed by `TURBIT-VoF` to accurately capture the concentration field.

(a)

(b)

(c)

Figure 4.10: Analytical (a) and numerical (b) concentration distribution for case of pure mass transfer in uniform flow. Comparison between analytical and numerical concentration isolines (c). $Re_{ref} = 100$ and $Sc_{ref} = 0.1$
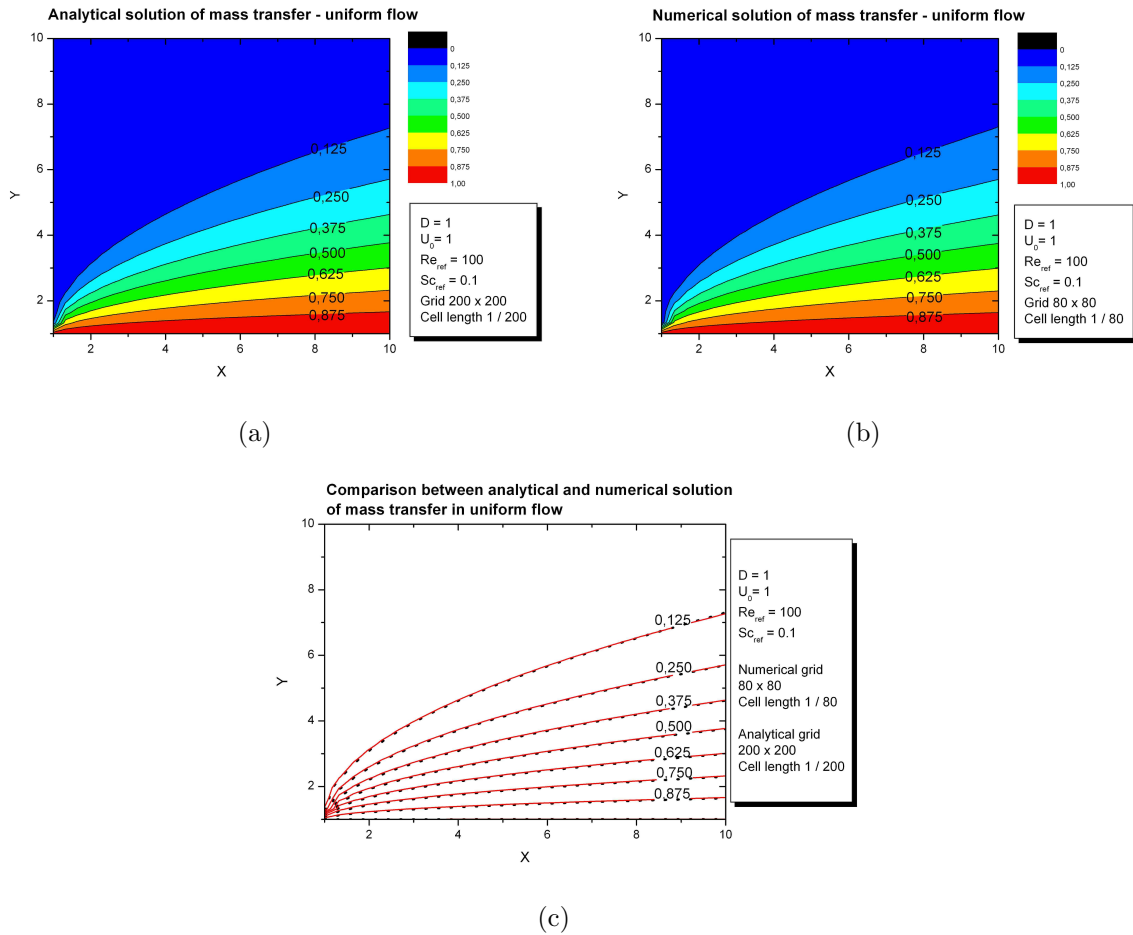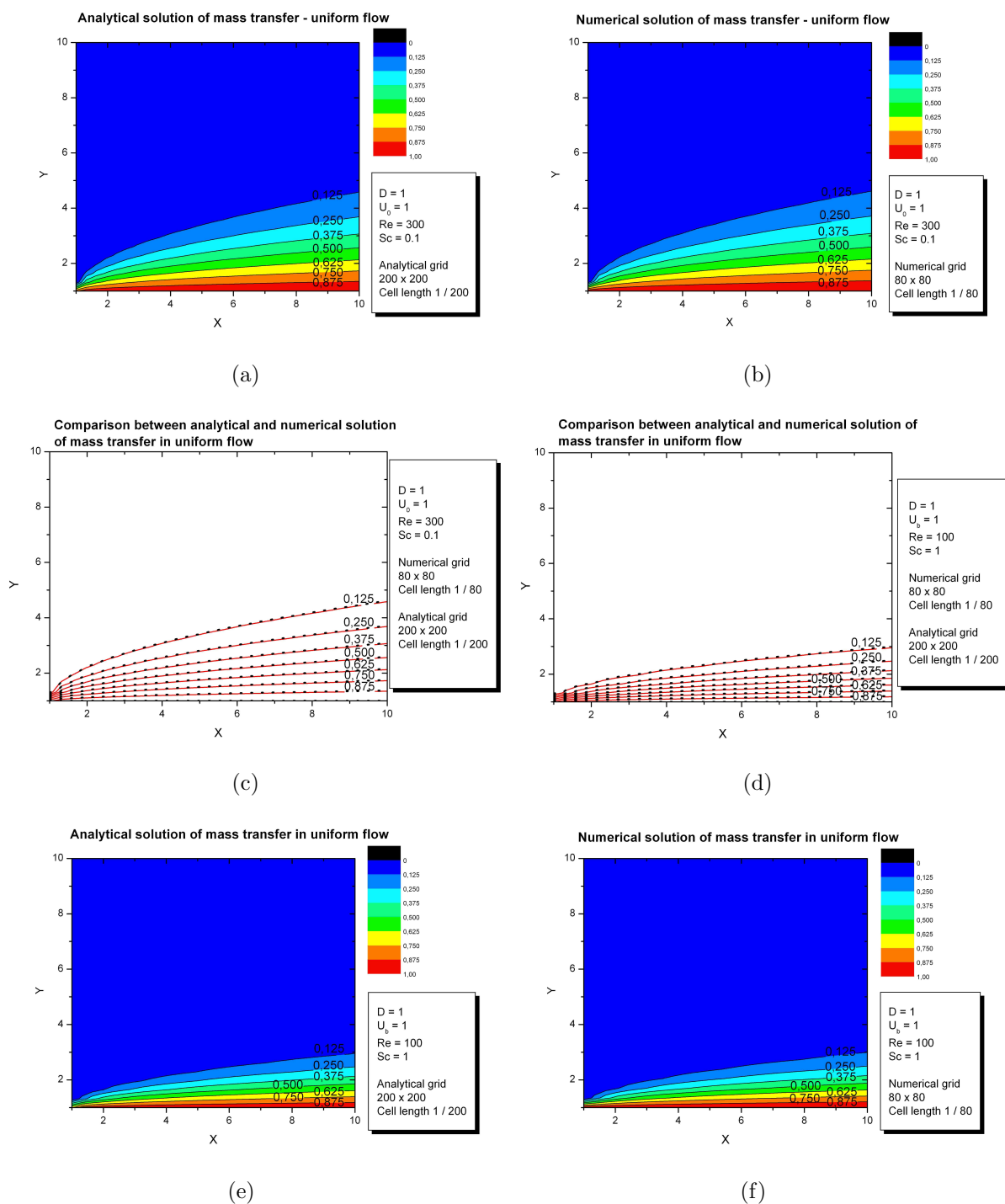
Figure 4.11: Analytical (a, e) and numerical (b, f) concentration distribution for case of pure mass transfer in uniform flow. Comparison between analytical and numerical concentration isolines (c, d). $\mathrm{Re_{ref}} = 300$ and $\mathrm{Sc_{ref}} = 0.1$ (a ÷ c), $\mathrm{Re_{ref}} = 100$, $\mathrm{Sc_{ref}} = 1$ (d ÷ f)

4.3.2   Mass transfer in two-phase flows

In order to investigate the implementation of the convective term, a numerical simulation of mass transfer during the rise of an 4mm air bubble in a stagnant mixture of water and glycerol was simulated. Oxygen represents the species transferred from the dispersed phase to the continuous phase. The results for mass transfer are compared against the numerical solution presented by Bothe et al. [8]. The results for the hydrodynamics of the problem are compared against the experimental data of Raymond and Rosant [64].

The rise of the initially sphere shaped bubble is considered for 0.2 s. The numerical simulation employed a 1 x 2 x 1 domain, discretized by 50 x 100 x 50 uniform mesh cells. The computational domain is bounded by four walls and has a square cross section. The equivalent bubble diameter is set to be one fourth of the channel width, that is $d_B^\star = l_{\text{ref}}^\star/4 = 0.004$m. Therefore, the resolution is 12.5 mesh cells per bubble diameter. The physical parameters of the fluids are displayed in Table 4.9.

	Water-glycerol mixture	Air
Density	1205 kg/m^3	1.122 kg/m^3
Dynamic viscosity	0.075 Pa s	18.24 x 10^{-6} Pa s
Oxygen diffusivity	62.24 x 10^{-8} m^2/s	19.16 x 10^{-6} m^2/s
Oxygen volume fraction	4 %	
Surface tension	0.063 N/m	
Henry number	0.03	
Morton number	98.17 x 10^{-5}	
Reference Weber number	301.25	
Reynolds number	0.37	27.95
Eötvös number	2.9525	
Weber number	6.247 x 10^{-4}	9.05 x 10^{-4}
Schmidt number	100	0.848
Kolmogorov length scale	6.72 x 10^{-4} m	2.45 x 10^{-4} m
Batchelor length scale	6.72 x 10^{-5} m	1.92 x 10^{-4} m
Cell length	32 x 10^{-5} m	

Table 4.9: Physical parameters

The Reynolds number for the liquid and gas phase are calculated as follows:

$$\text{Re}_L = \frac{\rho_L^\star U_L^\star l_{\text{ref}}^\star}{\mu_L^\star} \qquad\qquad \text{Re}_B = \frac{\rho_G^\star U_B^\star d_B^\star}{\mu_G^\star} \qquad (4.22)$$

The Weber number for both phases are given by:

$$\text{We}_L = \frac{\rho_L^\star l_{\text{ref}}^\star U_L^{\star\,2}}{\mu_L^\star} \qquad\qquad \text{We}_B = \frac{\rho_L^\star d_B^\star U_B^{\star\,2}}{\mu_G^\star} \qquad (4.23)$$

The Kolmorogov and the Batchelor length scales have been determined with the relations:

$$l^{\star}_{Ko} = \left(\frac{\nu^{\star 3}}{\epsilon^{\star}}\right)^{1/4} \qquad\qquad l^{\star}_{Ba} = \frac{l^{\star}_{K}}{\sqrt{Sc}}, \qquad\qquad (4.24)$$

where $\epsilon^{\star} = U^{\star}_{B}\, g^{\star}$ represents the rate of energy dissipation per unit mass [8] and Sc represents the Schmidt number:

$$Sc = \frac{\text{Kinematic viscosity}}{\text{Diffusivity}} = \frac{\nu^{\star}}{D^{\star}}, \qquad\qquad (4.25)$$

The gas volume fraction was determined using the definition:

$$\varepsilon = \frac{V^{\star}_{G}}{V^{\star}}, \qquad\qquad (4.26)$$

where $V^{\star}_{G}$ represents the volume of the dispersed phase and $V^{\star}$ represents the volume of the computational domain. Based on (4.26) it follows that the liquid volumetric fraction is $V^{\star}_{L}/V^{\star} = 1 - \varepsilon$.

Within the short period of time that was simulated, the bubble reached almost the steady-state. The magnitude of the velocity, which is displayed in Figure 4.12a is in good agreement with the experimental values obtained by Raymond and Rosant [64] for steady-state (see Table 4.10). Consistent results are obtained also for the bubble aspect ratio.

The concentration wake, as well as the bubble initial shape and position, are displayed in Figure 4.12b. Notice that the concentration field displayed is the one that is used during the integration, i.e. after applying the transformation (2.16).

Table 4.10 summarizes a comparison of the hydrodynamics and mass transfer data between the results presented in [8] and [64] and the results obtained with TURBIT-VoF.

	Bothe et al.	Raymond and Rosant	TURBIT-VoF
Bubble velocity attained	0.12 m/s	0.135 m/s	0.1136 m/s
Distance travelled	0.0205 m	-	0.02128 m
Aspect ratio	0.86	0.86	0.87
Length of concentration wake	0.014 m	-	0.018 m
Width of concentration wake	0.0028 m	-	0.0036 m

Table 4.10: Hydrodynamics and mass transfer results obtained by Bothe et al. [8], Raymond and Rosant [64] and TURBIT-VoF for the rise of a 4mm oxygen bubble in a mixture of water and glycerol

At the interface mass is transferred in the continuous phase only by diffusion. Therefore, the Schmidt number has a significant role. For the large value of the Schmidt number that was considered, small amounts of mass are transported across the interface. This leads to large concentration gradients at the interface. Therefore, a fine grid is needed to resolve
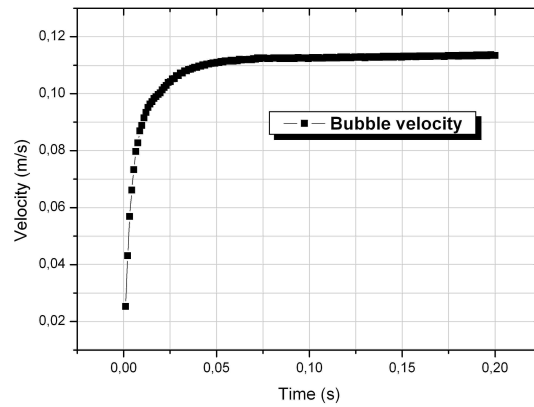
(a)
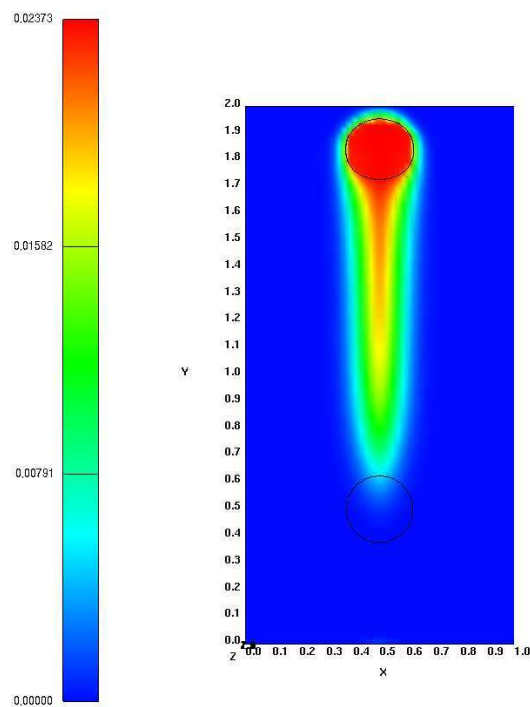
(b)

Figure 4.12: a) Bubble velocity computed by `TURBIT-VoF`. b) Concentration wake for a 4mm oxygen bubble rising in a water-glycerol mixture ($t^\star = 2$ s)

the thin concentration boundary layer that develops. In order to obtain a reasonable CPU time, the bubble diameter was resolved using 12.5 mesh cells, corresponding to a cell size of 0.32mm. The resolution of the grid employed by Bothe et al. [8] was 32 cells per bubble diameter, corresponding to a cell size of 0.125mm. While the results for the hydrodynamics agree very well with the experimental data, as can be seen in Table 4.10, the concentration wake is longer and wider as the one obtained by Bothe et al. [8]. We attribute this aspect to the insufficient resolution of the grid employed in `TURBIT-VoF`. The concentration wake is closed and contains the entire dissolved gas, as reported also by Bothe et al. [8] and Koynov et al. [45].

The numerical simulation performed with `TURBIT-VoF` on a POWER-4 processor required around 870 CPU hours.

In order to investigate the influence of the grid resolution, a numerical simulation employing a refined grid has been performed. A cubic domain, discretized by a refined grid consisting of 100^3 uniform mesh cells, was used instead of the previous parallelepiped-shaped domain to save computational time. In Figure 4.13 is displayed the concentration field in vertical midplane for the coarse and refined grid that were employed.

(a)   (b)
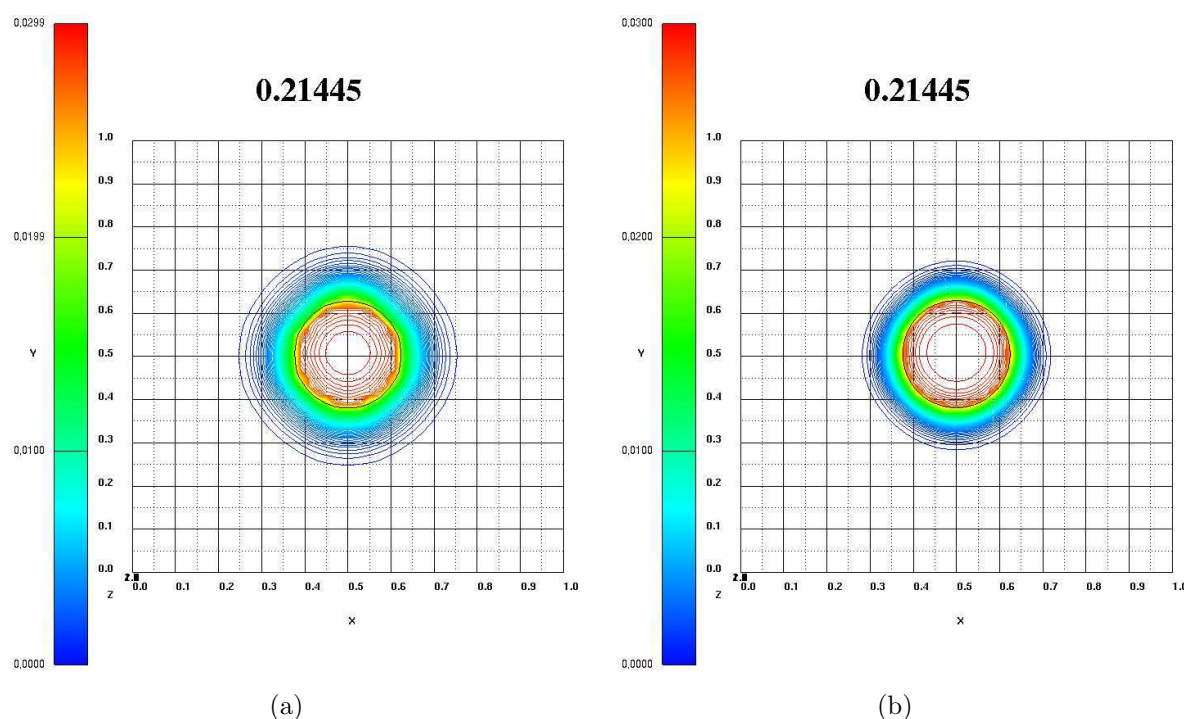
Figure 4.13: Concentration isolines in vertical midplane for grid 50x100x50 (a) and grid 100^3 (b) at time $t^\star \simeq 0.003$s

The simulation was made considering a smaller value of the Schmidt number, e.g. Sc = 1, for which the thickness of the concentration boundary layer is appreciably large as

a consequence of the large mass transfer by diffusion. Moderate concentration gradients develop therefore at the interface, decreasing the need for a refined grid. Only a short period of time was simulated, i.e. until $t^\star = 0.00343$ s (non-dimensional time $t = 0.21445$), since the computational time for the refined grid case is very large. Within this short period, the bubble raised an insignificant short distance, from the initial position at $x = y = 0.5$. Comparing Figure 4.13a and 4.13b one can notice that the concentration boundary layer was better captured in case of refined grid. Notice that the concentration distribution represents the transformed concentration field, the one which is actually used during the integration. This results demonstrates that employing a refined grid for the simulation of mass transfer during the rise of an 4mm oxygen bubble would lead to a thinner and shorter concentration wake, as reported by Bothe et al. [8].

4.4 Validation of the source term

In order to validate the implementation of the source term, `TURBIT-VoF` is compared against analytical solutions of purely mass transfer and mass transfer with heterogeneous and homogeneous chemical reaction. The analytical solutions are presented in literature by several authors [3, 63].

4.4.1 Mass transfer with first order homogeneous chemical reaction

The case of mass transfer into an adjoining fully developed laminar flow where the species is consumed by a first-order homogeneous chemical reaction is considered by Apelblat [3]. The hydrodynamics of the problem is similar to the one in the purely mass transfer case, illustrated in Figure (4.9). From the mathematical point of view, the source term for a homogeneous chemical reaction is considered in the partial differential equation, since the reaction takes place in the entire domain. At steady-state, considering diffusion only in the direction normal to the flow direction, the problem considered is governed by the following equation:

$$u_0^\star \frac{\partial c^\star}{\partial x^\star} = D^\star \frac{\partial^2 c^\star}{\partial y^{\star 2}} - k^\star c^\star, \tag{4.27}$$

subject to the boundary conditions (4.17).

The analytical solution of the problem is [3]:

$$\frac{c^\star(X^\star, Y^\star)}{c_0^\star} = \frac{1}{2} \left[\exp\left(-Y^\star\sqrt{k^\star}\right) \mathrm{erfc}\left(\frac{Y^\star}{2\sqrt{X^\star}} - \sqrt{k^\star X^\star}\right) \right.$$
$$\left. + \exp\left(Y^\star\sqrt{k^\star}\right) \mathrm{erfc}\left(\frac{Y^\star}{2\sqrt{X^\star}} + \sqrt{k^\star X^\star}\right) \right] \tag{4.28}$$

where $X^\star$ and $Y^\star$ are defined by equations (4.19).

Considering relations (3.4), (3.5), (3.7) and the reference parameters in Table 4.11 the non-dimensional form of the analytical solution (4.28) becomes:

$$
\begin{aligned}
\frac{c(x,y)}{c_0} = \; & \frac{1}{2}\Bigg[\exp\left(-y\sqrt{\mathrm{Re_{ref}Sc_{ref}}}\sqrt{\frac{k}{D}}\right)\mathrm{erfc}\left(\frac{y/\sqrt{D}}{2\sqrt{x/u_0}}\sqrt{\mathrm{Re_{ref}Sc_{ref}}}-\sqrt{\frac{k\,x}{u_0}}\right) \\
& + \; \exp\left(y\sqrt{\mathrm{Re_{ref}Sc_{ref}}}\sqrt{\frac{k}{D}}\right)\mathrm{erfc}\left(\frac{y/\sqrt{D}}{2\sqrt{x/u_0}}\sqrt{\mathrm{Re_{ref}Sc_{ref}}}+\sqrt{\frac{k\,x}{u_0}}\right)\Bigg] \quad (4.29)
\end{aligned}
$$

(a)   (b)

(c)
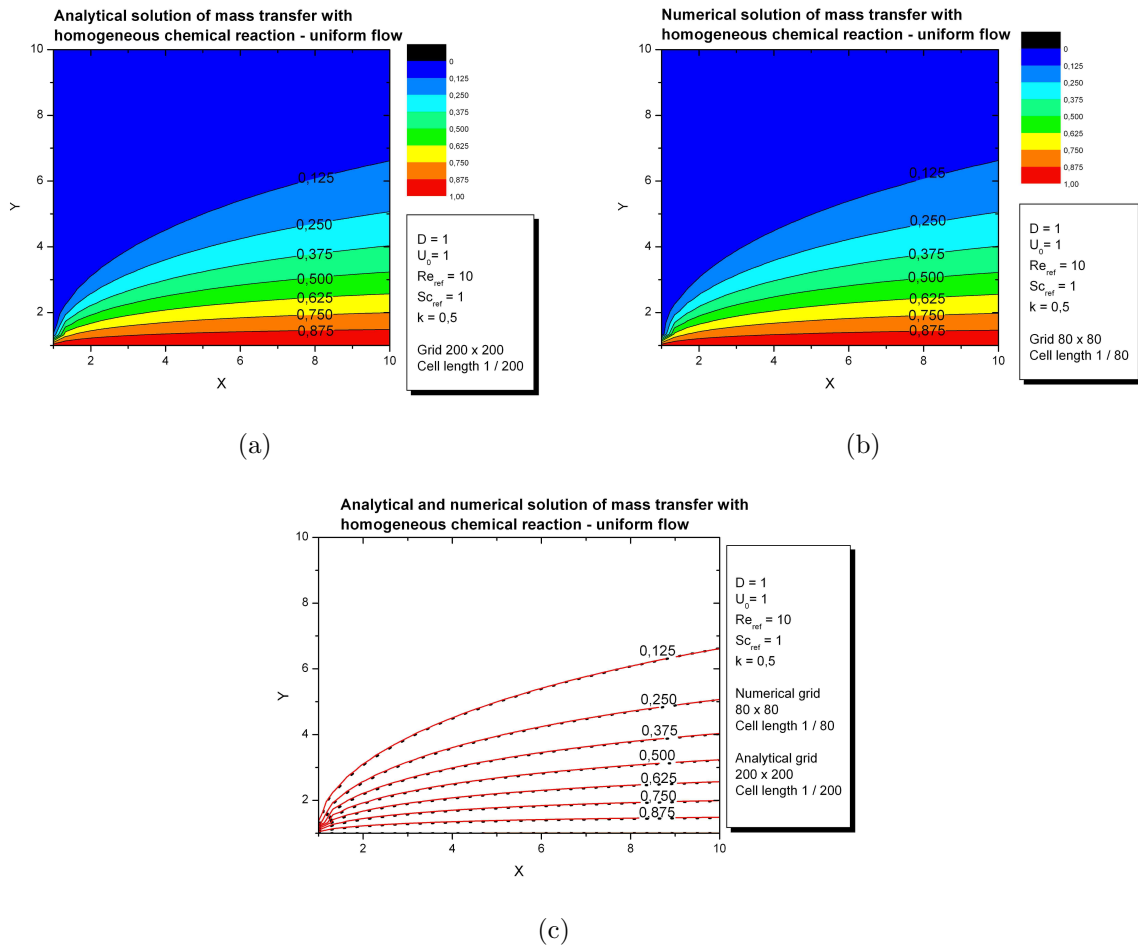
Figure 4.14: Analytical (a) and numerical (b) concentration distribution for mass transfer with homogeneous chemical reaction in uniform flow ($\mathrm{Re_{ref}} = 10$, $\mathrm{Sc_{ref}} = 1$ and $k = 0.5$)

(a)

(b)

(c)
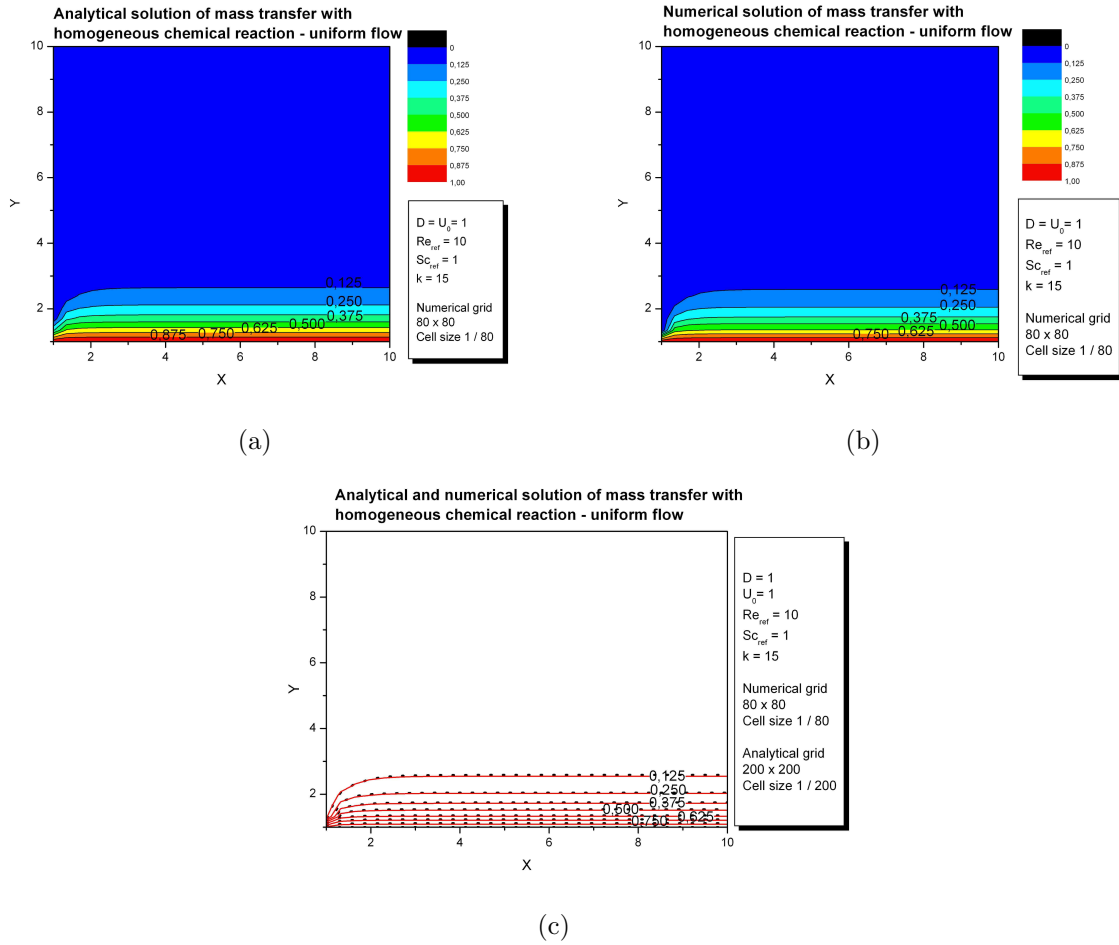
Figure 4.15: Analytical (a) and numerical (b) concentration distribution for mass transfer with homogeneous chemical reaction in uniform flow ($Re_{ref} = 10$, $Sc_{ref} = 1$ and $k = 15$)

$l^\star_{ref}[m]$	$v^\star_{ref}$ [m/s]	$g^{\star}_{ref}$ [m^2/s]	$D^{\alpha\star}_{ref}[m^2/s]$	$\Delta t^\star/t^\star_{ref}$	$k^\star_{ref}$ [s^{-1}]
1	1	0	1	10^{-4}	1

Table 4.11: Reference parameters for the numerical simulation of mass transfer accompanied by homogeneous reaction in single-phase flow

In Figure 4.14 is displayed the steady-state concentration field for a system having $Re_{ref} = 10$, $Sc_{ref} = 1$ and $k = 0.5$. In Figure 4.15 the concentration field displayed is evaluated for a constant of the reaction rate $k = 15$. Excellent agreement between the theoretical and numerical solution is obtained as presented in Figure 4.14c and 4.15c, where the concentration isolines are displayed. As the constant of the reaction is increasing, more

species is consumed in the bulk fluid by chemical reaction. As a consequence, at steady-state, the concentration boundary layer is thinner for a larger constant of reaction, as can be seen in the Figure 4.15.

4.4.2 Mass transfer with first order heterogeneous chemical reaction

The case of mass transfer with first-order heterogeneous chemical reaction is considered in this section. Figure 4.16 illustrates the hydrodynamics of the flow and the boundary conditions for mass transfer. The inlet and the wall at $y^\star \to \infty$ are held at constant concentration $c_0^\star$. The species is consumed by first order heterogeneous chemical reaction at the wall situated at $y^\star = 0$. From the mathematical point of view, the source term for a heterogeneous chemical reaction is considered in the boundary condition, since the reaction takes place at the wall. At steady-state, the problem considered is governed by the following partial differential equation:

$$u_0^\star \frac{\partial c^\star}{\partial x^\star} = D^\star \frac{\partial^2 c^\star}{\partial y^{\star 2}}, \tag{4.30}$$

subject to the boundary conditions:

$$
\begin{aligned}
c^\star &= c_0^\star & x^\star > 0 \quad y^\star &\to \infty \\
c^\star &= c_0^\star & x^\star = 0 \quad y^\star &\geq 0 \\
D^\star \frac{\partial c^\star}{\partial y^\star} &= k^\star c^\star & x^\star > 0 \quad y^\star &= 0
\end{aligned}
\tag{4.31}
$$

The analytical solution of the problem is presented by Apelblat [3]:

$$\frac{c^\star(X^\star, Y^\star)}{c_0^\star} = \exp\left(\beta^\star Y^\star + \beta^{\star 2} X^\star\right) \operatorname{erfc}\left(\frac{Y^\star}{2\sqrt{X^\star}} + \beta^\star \sqrt{X^\star}\right) + \operatorname{erf}\left(\frac{Y^\star}{2\sqrt{X^\star}}\right) \tag{4.32}$$

where $X^\star$ and $Y^\star$ are defined by equations (4.19) and $\beta^\star = k^\star/\sqrt{D^\star}$.

Considering relations (3.4), (3.5), (3.7) and the reference parameters in Table 4.12 the non-dimensional form of the analytical solution (4.32) becomes:

$$
\frac{c(x,y)}{c_0} = \exp\left[\sqrt{\mathrm{Re_{ref}Sc_{ref}}}\left(-\beta \frac{y}{\sqrt{D}} + \beta^2 \frac{x}{u_0}\right)\right]
$$
$$
\operatorname{erfc}\left(\frac{y}{\sqrt{D}}\frac{1}{2\sqrt{x/u_0}}\sqrt{\mathrm{Re_{ref}Sc_{ref}}} + \beta\sqrt{\frac{x}{u_0}}\sqrt{\mathrm{Re_{ref}Sc_{ref}}}\right) + \operatorname{erf}\left(\frac{y}{\sqrt{D}}\frac{1}{2\sqrt{x/u_0}}\sqrt{\mathrm{Re_{ref}Sc_{ref}}}\right)
\tag{4.33}
$$

In order to approximate the boundary condition $c^\star = c_0^\star$ at the wall $x^\star > 0$ and $y^\star \to \infty$, the numerical simulation has to be evaluated considering a domain of size 1 x n,
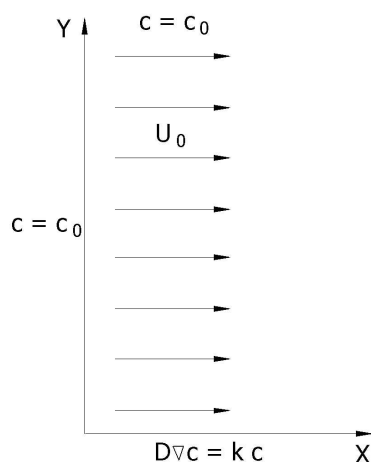
Figure 4.16: Flow hydrodynamics for the problem of mass transfer with heterogeneous chemical reaction

where n > 3. In this way is minimized the influence of the presence of the wall at finite y on the concentration field.

$l_{\text{ref}}^{\star}[\text{m}]$	$v_{\text{ref}}^{\star}$ [m/s]	$g_{\text{ref}}^{\star}$ [m^2/s]	$D_{\text{ref}}^{\alpha\star}[\text{m}^2/\text{s}]$	$\Delta t^{\star}/t_{\text{ref}}^{\star}$	$k_{\text{ref}}^{\star}$ [m/s]
1	1	0	1	10^{-4}	1

Table 4.12: Reference parameters for the numerical simulation of mass transfer accompanied by heterogeneous reaction in single-phase flow

In Figure 4.17a ÷ c the steady-state concentration field is displayed for a system with $\text{Re}_{\text{ref}} = 10$, $\text{Sc}_{\text{ref}} = 0.1$ and $k = 10$, while Figure 4.17d ÷ f displays the stationary concentration field for $k = 50$. Very good agreement between the theoretical and numerical solution has been obtained, as presented in Figure 4.17c and d, where the concentration isolines are displayed.

As the constant of the heterogeneous chemical reaction increases, more mass is consumed at the wall by chemical reaction. Therefore, at steady-state, in the region close to the wall, where the chemical reaction occurs, the species concentration is small.

Figure 4.17: Analytical and numerical concentration distribution for mass transfer with first order heterogeneous chemical reaction in uniform flow ($Re_{ref} = 10$ and $Sc_{ref} = 0.1$ and $k = 10$ (a ÷ c) and $k = 50$ (d ÷ f)

Chapter 5

Numerical simulations of interfacial mass transfer with and without chemical reaction in mini-channels

This chapter presents the numerical simulations of mass transfer with and without chemical reaction in two-fluid flows with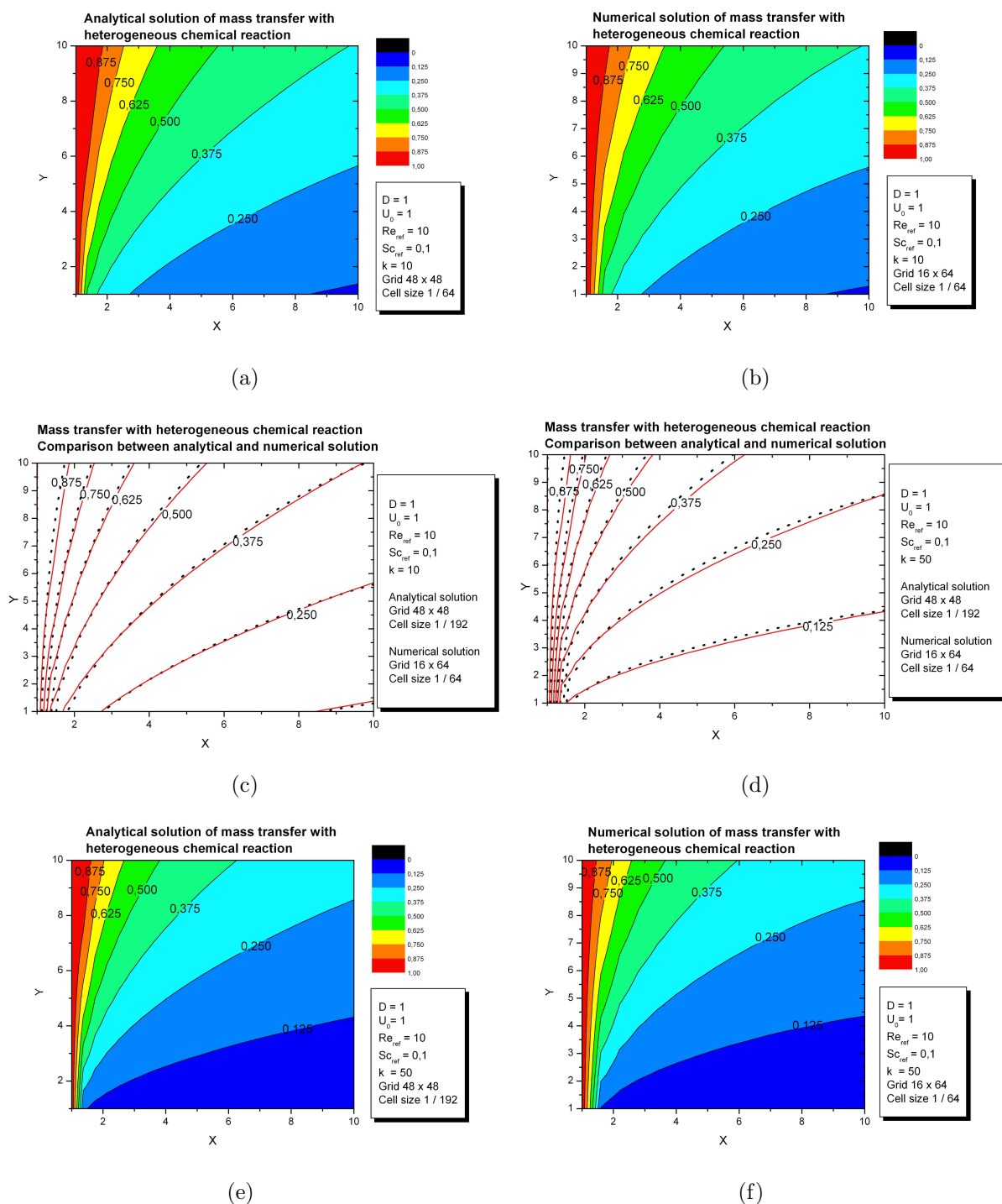in small channels. The first section describes the bubble train flow. Further, the influence of the unit cell length, liquid slug length and bubble length on the mass transfer process in bubble train flow is discussed. The last section compares the mass transfer process in square and rectangular mini-channels of identical hydraulic diameter.

5.1   Bubble train flow

Bubble train flow represents a flow pattern commonly encountered in two-phase flows in mini- and micro-devices. The flow consists of usually long bubbles, separated by liquid slug, flowing concurrently in capillaries having circular or square cross-section. For steady-state bubble train flow, one can identify regions that are free of entrance effects and which consists of bubbles that have an identical shape and move with a constant velocity. Therefore, one can define a unit cell consisting of one bubble and the liquid slug that characterize completely the developed bubble train flow. The bubbles fill almost the entire cross-section of the capillary, being separated from the wall by a thin liquid film. Such a unit cell is displayed in Figure 5.1 for a bubble that rises. In Figure 5.1 are presented also the boundary conditions that are used during the simulations.

The bubble train flow is of interest since the flow pattern has an important influence on the mass transfer process. For mass transfer in bubble train flow the volumetric mass transfer coefficient is reported to be inverse proportional with the unit cell length in circular capillaries [5, 87]. For mass transfer with chemical reaction at the wall significantly increased radial mass transfer in reactors having catalytically walls are reported in [27, 33].

(a)
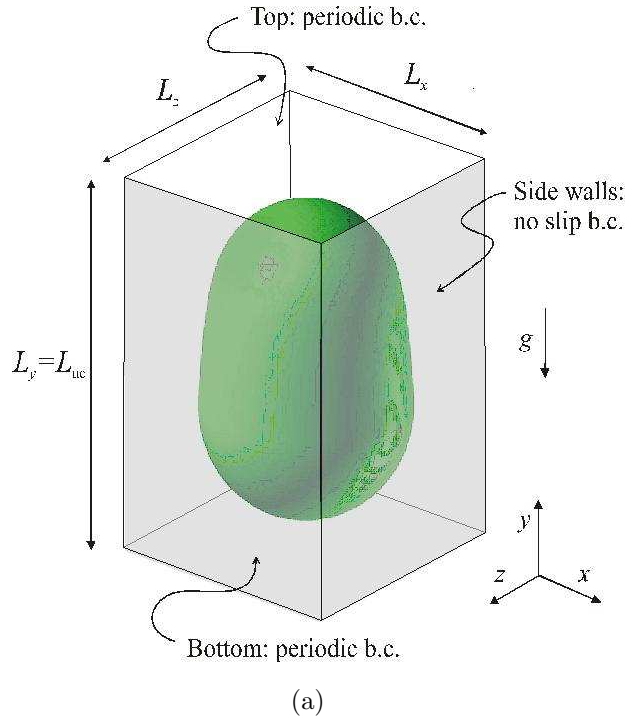
Figure 5.1: Concept of a unit cell

Case	Grid	$\varepsilon[\%]$	$L_{UC}^\star/L_z^\star$	$L_x^\star/L_z^\star$	$U_B^\star/U_{ref}^\star$	$U_l^\star/U_{ref}^\star$	Section
A	48 x 48 x 48		1.0	1	3.65	1.208	
B	48 x 66 x 48	33	1.375	1	3.65	1.307	5.2
C	48 x 84 x 48		1.750	1	3.67	1.324	
D	48 x 66 x 48	33	1.375	1	3.763	1.333	5.3
E	48 x 80 x 48	24.77	1.667	1	3.804	1.604	5.3,5.4
F	48 x 80 x 48	31.89	1.667	1	3.764	1.388	5.4
G	48 x 60 x 48		1.25	1	3.62	1.294	
H	60 x 66 x 48	33	1.1	1.25	3.646	1.125	5.5
I	64 x 60 x 40		0.9375	1.60	3.62	1.15	

Table 5.1: Flow parameters of the performed simulations

Due to the predominance of the surface tension forces over gravity forces in flows within capillaries, the bubble train flow has the same characteristics in both vertical and horizontal direction. The influence of the surface tension forces in flows within capillaries is quantified by the Capillary number:

$$\mathrm{Ca} = \frac{\mu_L^\star U_B^\star}{\sigma^\star}, \tag{5.1}$$

where $\mu_L^\star$ represents the dynamic viscosity of the liquid phase, $U_B^\star$ the velocity of the bubble and $\sigma^\star$ the surface tension. For Ca > 0.1, bubbles flowing within square cross-section capillaries are reported to be axisymmetric, while for Ca < 0.1, the bubbles tend to fill the corners of the channel [44].

Table 5.1 describes the flow parameters for the simulations considered in this chapter.

For all the simulations performed, null concentration flux at the walls and periodic boundary conditions for the concentration field along axial direction have been considered.

5.2 Influence of unit cell length on mass transfer process

In this section is investigated the influence of the unit cell length ($L_{\mathrm{UC}}^\star$) on mass transfer for an arbitrary species. The influence of the length of the unit cell on the hydrodynamics of two-phase flow was reported by Wörner et al. [103]. They extended the original work of Ghidersa [23, 24], which studied numerically the influence of the Capillary number on two-phase flows and compare it successfully with the experimental work of Thulasidas et al. [80].

Three simulations have been performed, with a length of the unit cell ranging between 1 and 1.75, as presented in Table 5.2. The computational domain is $l_{\mathrm{ref}}^\star$ x $L_{\mathrm{UC}}^\star$ x $l_{\mathrm{ref}}^\star$. After normalizing with the reference length $l_{\mathrm{ref}}^\star = 0.002$ m, the non-dimensional domains employed are 1 x L_{UC} x 1. The same gas volume fraction, i.e. $\varepsilon = 33\%$, was used in all simulations. The coordinate system is defined so that y represents the stream-wise vertical direction, while x and z the wall-normal directions. The physical parameters of the fluids, as well as mass transfer parameters are presented in Table 5.3. The gas phase density and viscosity were set 10 times higher than in reality, in order to increase the computational efficiency. For low values of the density ratio the time integration scheme imposes a small value of the time step. The procedure is based on the invariance of the velocity field and bubble shape for different gas-liquid density ratios, reported by Wörner et al. [102].

The lengths of the bubbles that are used in experiments is several times the width of the channel. Employing such a realistic bubble length would require a large computational domain that would lead to significant increase in computational time. Therefore, rather "short" bubbles have been employed in the simulations.

The simulations were performed using the following strategy. First, the hydrodynamic steady-state was obtained, i.e. the bubble shape and velocity as well as the liquid velocity are constant. The bubble was initialized afterwards with the concentration $c_G^{\alpha\star}(0) = H^\alpha$, which corresponds to the physical initial gas concentration $c_G^{\alpha\star}(0) = 1$ mol/m^3, after the transformation (2.16) is applied. The initial concentration in liquid is zero. The pressure drop was adjusted in such a way that the bubble velocity is equal in all cases. Still, the liquid velocity obtained is directly proportional to $L_{\mathrm{UC}}^\star$, i.e. long $L_{\mathrm{UC}}^\star$ have an intense recirculation within the liquid slug.

The velocity field in bubble frame of reference, using normalized vectors, is displayed

Case	A	B	C
Domain [mm]	2 x 2 x 2	2 x 2.75 x 2	2 x 3.50 x 2
Domain's volume [m^3]	8 x 10^{-9}	11 x 10^{-9}	14 x 10^{-9}
Interfacial area [m^2]	9.35 x 10^{-6}	16.24 x 10^{-6}	24.79 x 10^{-6}
Interfacial area concentration [-]	2.33759	2.9529	3.54132
Interfacial area concentration [1/m]	1168.795	1476.45	1770.66
Bubble velocity [m/s]	0.09636	0.09636	0.09688
Liquid velocity [m/s]	0.03189	0.0345	0.03495
Reference velocity [m/s]		0.0264	
Reference length [m]		0.002	
Reference concentration [mol/m^3]		1	
Schmidt number (liquid)		0.806	
Morton number		49.26 x 10^{-4}	
Reference Reynolds number		1.0527	
Bubble Reynolds number	9.8896	10.5695	10.5031
Capillary number		0.2085	
Reference Eötvös number		1.6724	
Bubble Eötvös number	1.0703	1.2226	1.1941
Reference Weber number		60.14 x 10^{-3}	
Bubble Weber number	78.37 x 10^{-3}	83.76 x 10^{-3}	83.68 x 10^{-3}
Euler number	27.03	26.23	23.8

Table 5.2: Flow parameters for different unit cell lengths

	Continuous phase	Dispersed phase
Density $\rho^\star$ [kg/m^3]	957	11.7
Dynamic viscosity $\mu^\star$ [Pa s]	0.048	1.842 x 10^{-4}
Species diffusivity $D^\star$ [m^2/s]	62.24 x 10^{-6}	19.16 x 10^{-6}
Surface tension $\sigma^\star$ [N/m]		0.02218
Henry number H [-]		0.03 and 3
Reaction constant $k^\star_{\text{Hmg}}$ [1/s]		1500
Reaction constant $k^\star_{\text{Htg}}$ [m/s]		50

Table 5.3: Physical parameters

in Figure 5.2 for each unit cell length configuration. The scale shown in the left part of the picture represents the non-dimensional `TURBIT-VoF` velocity and it is case specific. It can be observed that one laminar toroidal vortex develops in the bubble for each flow

configuration. The intensity of the vortex in the liquid slug is much smaller than the one of the bubble vortex, due to the flow low Reynolds number. It can be observed that the intensity of the vortex (in the bubble and also in the liquid) is directly proportional with the L_{UC}, although the bubble velocity is similar.

(a)   (b)   (c)
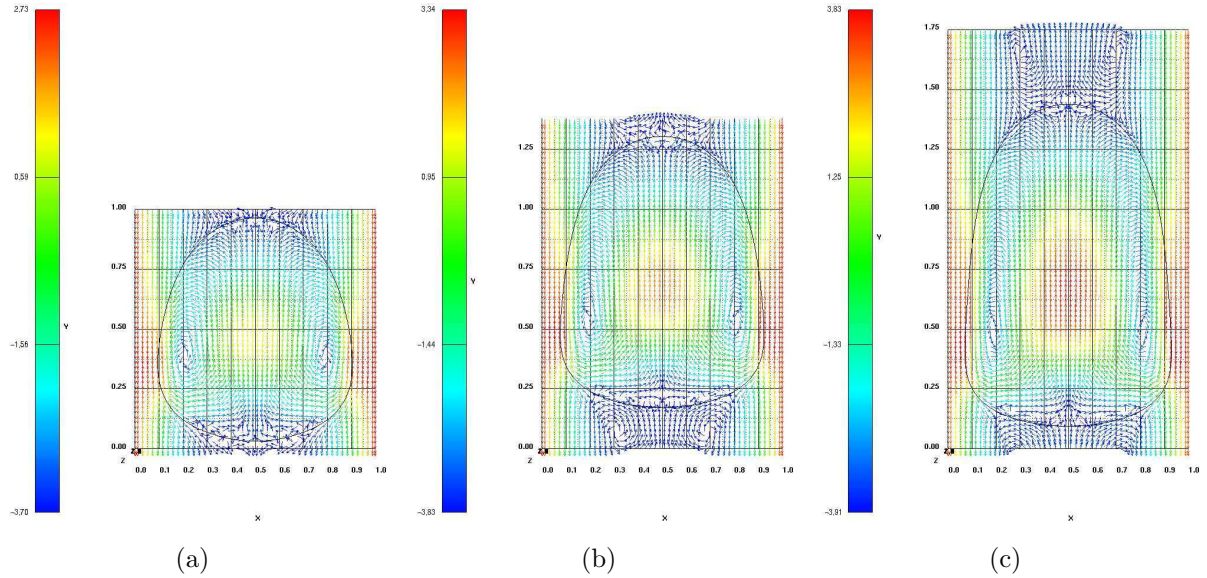
Figure 5.2: Velocity field in bubble frame of reference for $L_{UC}^{\star} = 2$mm (a), $L_{UC}^{\star} = 2.75$mm (b) and $L_{UC}^{\star} = 3.5$mm (c) in vertical midplane

(a)   (b)   (c)
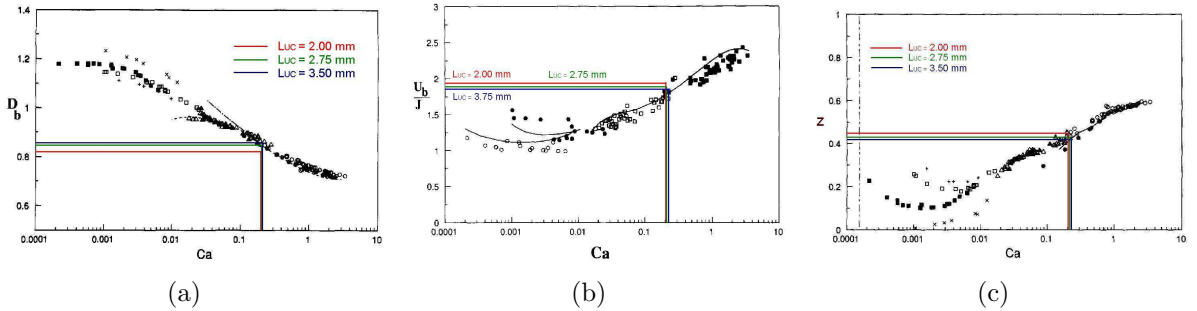
Figure 5.3: Non-dimensional bubble diameter (a), non-dimensionless bubble velocity (b) and the ratio of relative velocity to bubble velocity (c) as function of the Capillary number. The figures showing experimental data are reproduced from [80].

For the validation of the two-phase flow hydrodynamics, the non-dimensional bubble diameter $D_B^{\star}/D_h^{\star}$, the ratio of bubble velocity to the total superficial velocity $U_B^{\star}/J^{\star}$ and the ratio of the relative velocity to the bubble velocity $(U_B^{\star} - J^{\star})/U_B^{\star}$ are compared in

Figure 5.3 against the experimental data reported by Thulasidas et al. [80]. The discrete values of these parameters obtained with `TURBIT-VoF` are displayed in Table 5.4.

The total superficial velocity is defined as:

$$J^\star = \varepsilon U_G^\star + (1 - \varepsilon)U_L^\star, \tag{5.2}$$

where the mean gas velocity $U_G^\star$ is equal to the bubble velocity $U_B^\star$ and $U_L^\star$ represents the mean liquid velocity, while the relative bubble velocity is defined as follows:

$$Z = \frac{U_B^\star - J^\star}{U_B^\star} \tag{5.3}$$

Case	$L_{\mathrm{UC}}^\star[\mathrm{mm}]$	$D_B^\star/D_h^\star$	$U_B^\star/J^\star$	Z
A	2.00	0.822	1.812	0.448
B	2.75	0.846	1.755	0.430
C	3.50	0.858	1.749	0.428

Table 5.4: Non-dimensional bubble diameter, bubble velocity to total superficial velocity ratio and relative velocity computed with `TURBIT-VoF`

Although all three simulations have almost the same Capillary number, the thickness of the liquid film between the bubble and the wall, measured in the region where the bubble exhibits its largest diameter, decreases with increasing unit cell length $L_{\mathrm{UC}}^\star$. This appears to be an effect of the increased intensity of the velocity field, which is proportional to the unit cell length. As a consequence, as the unit cell length increases, the intensity of the forces acting on the bubble increases also, leading to a larger bubble deformation, i.e. a thinner liquid film and a wider bubble. This explains why the shortest unit cell case deviates slightly from the experimental result. It is worth mentioning that long bubbles were used in the experiments performed in [80]. For the bubbles having $L_B^\star > L_{\mathrm{UC}}^\star$ excellent agreement is found. Very good agreement is found for the bubble velocity and bubble relative velocity.

Pure mass transfer

Mass transfer is considered in three systems having different length of the unit cell, for Henry number $H = 0.03$ and $H = 3$. Figure 5.4 displays the normalized mean gas concentration distribution, the equilibrium concentration determined with relation (5.6), the mass transfer coefficient evaluated with formula (4.13) and the Sherwood number (4.14) function of Fourier number (4.15). The normalized mean gas concentration represents the concentration in the bubble at time level $t^\star$ divided by the initial bubble concentration $c_G^{\alpha\star}(0)$. From Figure 5.4 it can be observed that the short unit cell is more efficient (has a stepper gradient) than long unit cell for any Henry number. The same conclusion is reported also by van Baten and Krishna [87] for mass transfer in Taylor flow operated within circular capillary.

(a)

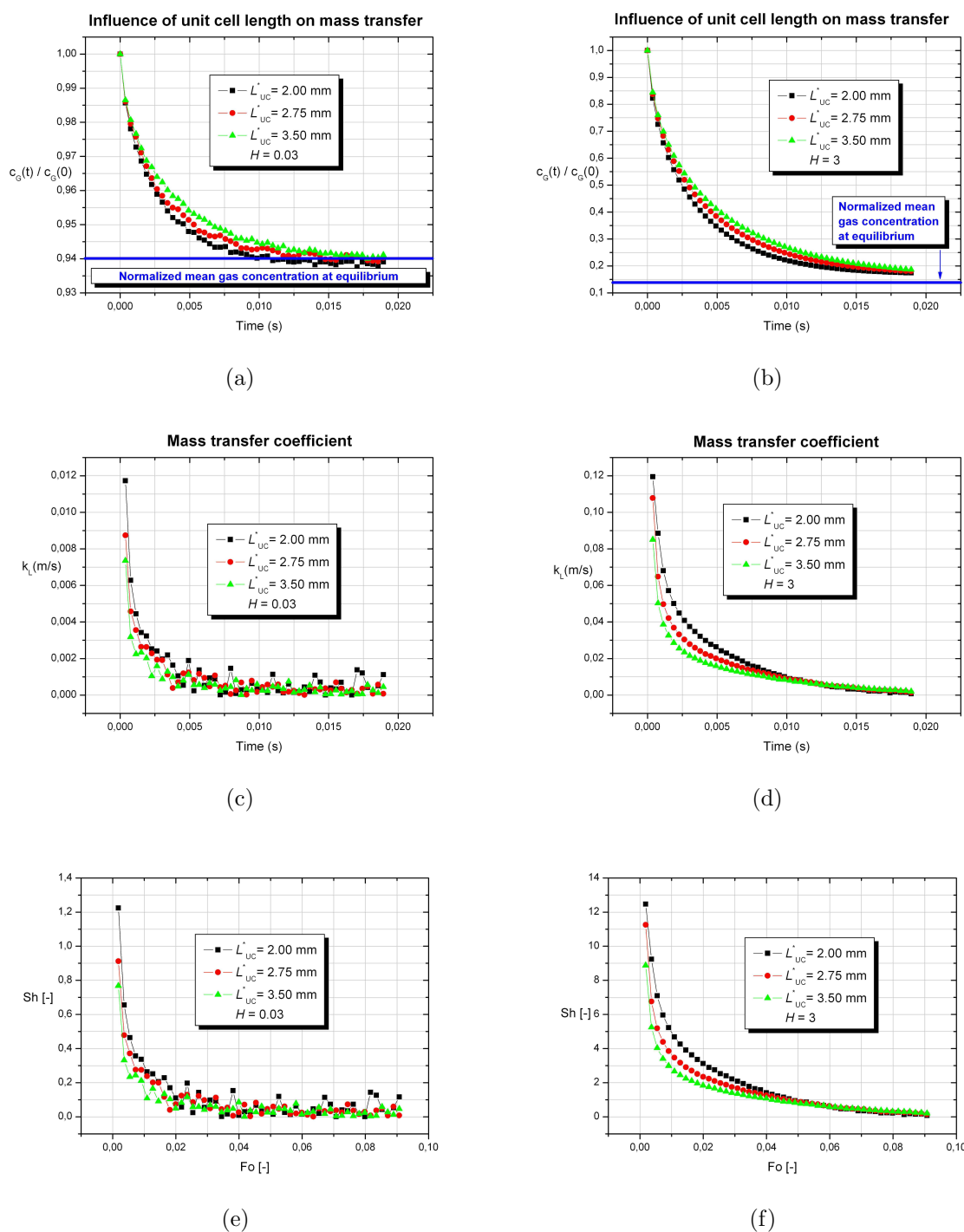
(b)

(c)

(d)

(e)

(f)

Figure 5.4: Influence of the unit cell length on mass transfer for $H = 0.03$ (a, c) and $H = 3$ (b, d). Mass transfer coefficient (4.13) (c, d). Sherwood number (4.14) function of the Fourier number (4.15) (e, f)

The interfacial area concentration is smaller for systems with shorter unit cell than for systems with longer unit cell, for the same length of the domain (see Table 5.2). The larger interfacial area concentration, which is specific to two-phase flows in micro-reactors, is considered to be responsible for the high mass transfer rates realized in these devices. The results in Figure 5.4 show that the largest mass transfer rate are obtained for the smallest $L_{\text{UC}}^{\star}$ case, i.e. for the system employing the smallest interfacial area concentration. Longer unit cell configurations exhibit a larger contact area between the bubble interface and the wall by means of a liquid film than short unit cell systems. The liquid film in this contact area provides a buffer zone in which mass is rapidly accumulating due to short diffusion lengths and long exposure time. Therefore, the film becomes very rapidly saturated, leading to a fast decrease of the local concentration gradient.

Considering a mass-less particle flowing within the film, the period for which the particle is entrapped in the liquid film represents the exposure time, which can be determined with the following expression:

$$t_{\text{exp}}^{\star} = \frac{\text{Liquid film length}}{\text{Liquid velocity}}, \qquad (5.4)$$

where the liquid velocity in the film was considered in the bubble frame of reference (see Figure 5.2).

The time of exposure in the liquid film can be estimated in terms of Fourier number, with Fo < 1 denoting short contact time and Fo > 1 long contact time [81]. For short exposure time, although the diffusion length is very small, no accumulation of the species occurs due to the fast convective transport in the liquid film. For long exposure time, the liquid film is slowly refreshed, leading to the species accumulation in this region and therefore to rather ineffective local mass transfer.

Unit cell length [mm]	2	2.75	3.50
Length of the film [m]	4.2×10^{-4}	8×10^{-4}	11.8×10^{-4}
Liquid velocity in the film [m/s]	0.066	0.082	0.095
Time of exposure [s]	6.36×10^{-3}	9.77×10^{-3}	12.41×10^{-3}
Thickness of the film [m]	18×10^{-5}	15.4×10^{-5}	14×10^{-5}
Fourier number	12.224	25.654	39.427

Table 5.5: Time of exposure and Fourier number

In order to determine the Fourier number, the exposure time $t_{\text{exp}}^{\star}$ was considered instead of time $t^{\star}$ and the thickness of the film was deemed as the characteristic length in expression (4.15). The Fourier number, the exposure time and thickness of the film for each UC configuration are displayed in Table 5.5. It can be concluded that the film between the bubble and the wall is saturated faster in systems having large $L_{\text{UC}}^{\star}$ than in systems with small $L_{\text{UC}}^{\star}$. Nevertheless, since Fo > 0.1 for all configurations, the film is saturated almost instantaneously.

The concentration distribution is displayed in Figure 5.6 for the case with $H = 0.03$ and in Figure 5.7 for systems having $H = 3$. Notice that the concentration scale shown in the left is case specific. For $H = 0.03$, the concentration in the bubble is the one used during the integration, which is continuous at the interface. Due to the low Henry number, a visualization consisting of real concentration values is not used since it cannot display meaningfully the concentration distribution. In order to transform back the bubble concentration field, one needs to divide the concentration in the dispersed phase with the Henry number $H = 0.03$. For the case $H = 3$ the non-dimensional concentration field is displayed. For all cases, the concentration field displayed for the continuous phase is non-dimensional. Inspecting these figures one can observe that the liquid film between the bubble and the wall is rapidly saturated with species, as predicted by the Fourier number in Table 5.5.

As the concentration field in the liquid becomes saturated, the normalized mean concentration becomes independent of the unit cell length, since the rates of mass transfer equalize. It is to be expected that, for real much longer bubbles that are used in experiments, the normalized mean concentration to be larger, i.e. less mass is transferred across the interface, than the one obtained for the rather "short" bubbles that were considered in the simulations. Based on the results obtained, the recommended strategy for bubble injection is the introduction of groups of small bubbles separated in time, instead of a regularly bubble train flow consisting of large bubbles.

The large value of the normalized mean gas concentration in Figure 5.4 a., i.e. $c_t^\star/c_0^\star \cong 0.94$, is explained by the small amount of mass needed in the liquid phase for the system to achieve the equilibrium state, as described by equation (2.9)

For small values of the Henry number, the amount of mass needed in the liquid phase for the system to achieve the equilibrium state is also small, as described by equation (2.9). This explains the large value of the normalized mean gas concentration in Figure 5.4a. and the fact that equilibrium is rapidly established. The value of the normalized mean gas concentration at equilibrium can be estimated based on the mass conservation, as follows:

$$c_G^{\alpha\star}(0)\, V_G^\star = c_G^{\alpha\star\mathrm{eq}}\, V_G^\star + c_L^{\alpha\star\mathrm{eq}}\, V_L^\star \tag{5.5}$$

Inserting relations (2.9), (4.26) and rearranging one obtains the normalized mean gas concentration at equilibrium:

$$\frac{c_G^{\alpha\star\mathrm{eq}}}{c_G^{\alpha\star}(0)} = \frac{1}{1 + H^\alpha(1/\varepsilon - 1)}, \tag{5.6}$$

For $H = 0.03$, the normalized mean gas concentration at equilibrium is $c_G^{\alpha\star\mathrm{eq}}/c_G^{\alpha\star}(0) = 0.94$ in very good agreement with the normalized mean gas concentration obtained numerically, as can be observed in Figure 5.4a. For $H = 3$, the normalized mean gas concentration at equilibrium is $c_G^{\alpha\star\mathrm{eq}}/c_G^{\alpha\star}(0) = 0.14$, being slightly smaller than the normalized mean gas concentration obtained numerically. This result suggests that, in case of $H = 3$, the equilibrium has not been reached in the system in the time interval simulated.

In Figure 5.5 is presented the normalized mean gas concentration for case A and the equilibrium concentration determined with formula (5.6). It can be observed that equilibrium is reached in approximately 0.015s due to large diffusivity in the liquid and small

Henry number. Since the gas concentration in cells containing the interface was not considered, the normalized mean gas concentration obtained numerically has a slightly smaller value than the normalized mean gas concentration at equilibrium obtained theoretically.
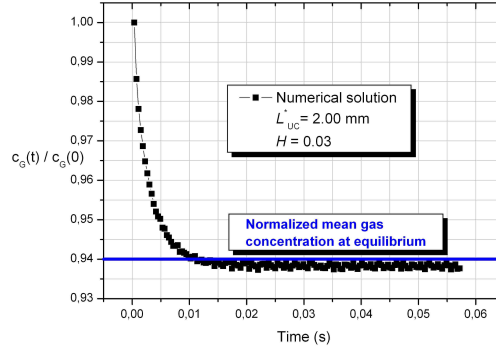
(a)

Figure 5.5: Normalized mean gas concentration for case A

For longer $L_{UC}^\star$ and $H = 0.03$ one can observe that the bubble inner vortex plays an important role. The major part of species inside the bubble is entrapped inside the vortex and recirculated along it. This behavior allows for a continuously supplied mass at the interface, in the region close to the wall. Since this region becomes very rapidly saturated with species, due to small diffusion lengths, the efficiency of this region decreases. It can be expected that for circular channels the efficiency will decrease even faster due to the lack of the fluid recirculation within corners and faster saturation. Also, one can observe in Figures 5.6 that a large concentration gradient builds up at the bottom and at the cap of the bubble. In these regions most of the mass transfer takes place by diffusion, since the velocity gradients are very small. Therefore the species concentration within the cap and the bottom have approximately the same value. The bubble top and bottom contribute to the major part of the mass transfer. The same observation is reported also by Berčič and Pintar [5], based on experimental investigations. Elperin and Fominykh [18] investigated theoretically the contribution of the leading edge of the bubble to the total mass flux. For bubbles in the range of the lengths used in this study, i.e. $L_B^\star/L_x^\star \simeq 1.5 \div 3$, it is found that the bottom part of the bubble contributes significantly to the mass transfer.

The smallest $L_{UC}^\star$ case exhibits a different concentration pattern than the other two cases for $H = 0.03$, which can be a result of two hydrodynamical characteristics. The first one is that the very small liquid slug presents no vortex. The second one is the smaller intensity of the bubble vortex as compared to the one in case of longer $L_{UC}^\star$. Therefore, at the initial stage of simulation diffusion dominates over convection. As the concentration field levels off, the influence of the diffusion decreases in favor of the bubble inner vortex, i.e. species recirculation along the vortex will be observed.
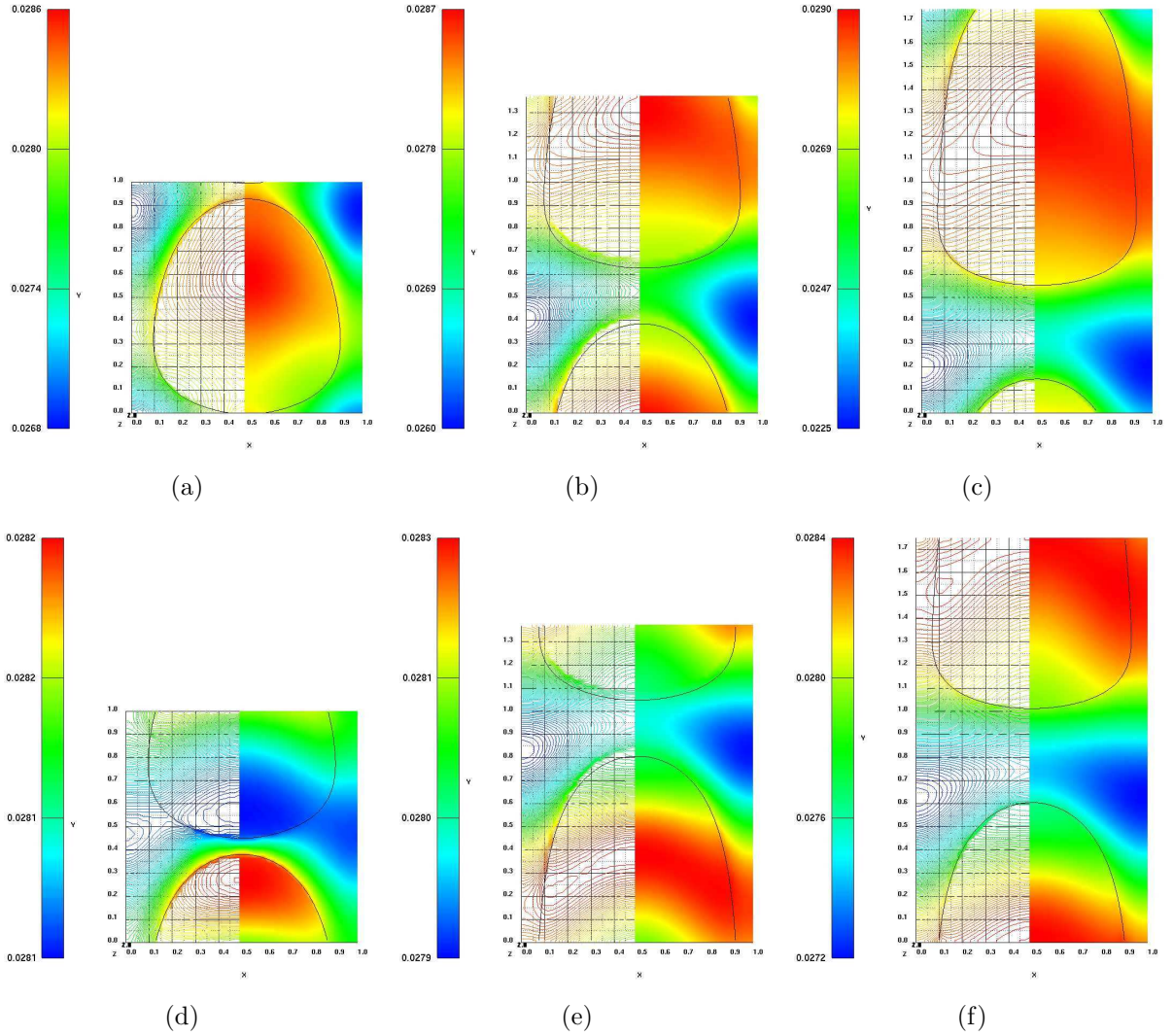
Figure 5.6: Non-dimensional concentration field for $L_{UC}^{\star} = 2$mm (a, d), $L_{UC}^{\star} = 2.75$mm (b, e) and $L_{UC}^{\star} = 3.50$mm (c, f) at time $t^{\star} \simeq 0.01$ s (a $\div$ c) and $t^{\star} \simeq 0.02$ s (d $\div$ f) for Henry number $H = 0.03$ in vertical midplane

The main difference in the concentration distribution between systems with $H < 1$ (see Figure 5.6) and systems with $H > 1$ (see Figure 5.7) is that, for the latter, the diffusion process dominates over convection, at the beginning of the simulation. This aspect is attributable to the large concentration gradient specific for these cases. Therefore, for the small periods of time that are simulated, no mass recirculation is observed. Similar to the cases with $H < 1$, the cap and the bottom of the bubble contribute to the major part of the mass transfer, as seen in Figure 5.7a $\div$ c, while the lateral part of the bubble is ineffective due to the saturation in the liquid film.

At the interface, a concentration gradient develops due to the different solubility of

the transferred species. This concentration gradient enhances the mass transfer in two ways. In the first place, it enhances the mass transfer in the bubble, towards the interface. In the liquid phase, due to the large concentration difference, the mass diffuses fast toward the bulk of the liquid.
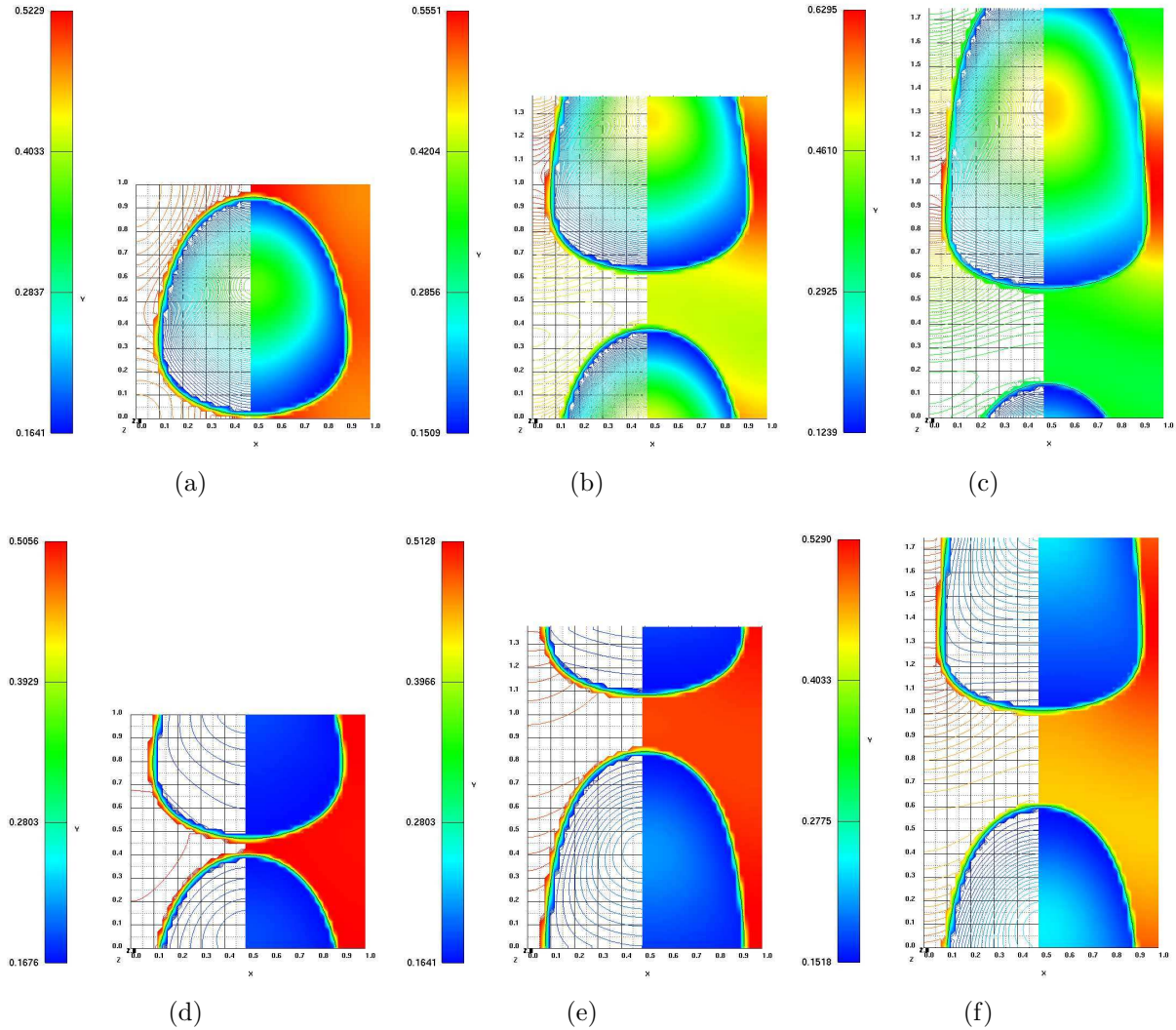
Figure 5.7: Non-dimensional concentration field for $L_{\mathrm{UC}}^{\star} = 2$mm (a, d), $L_{\mathrm{UC}}^{\star} = 2.75$mm (b, e) and $L_{\mathrm{UC}}^{\star} = 3.50$mm (c, f) at time $t^{\star} \simeq 0.01$ s (a ÷ c) and $t^{\star} \simeq 0.02$ s (d ÷ f) for Henry number $H = 3$ in vertical midplane

As expected, the need for refined grid increases with the increase of the Henry number, as can be observed in Figure 5.6 and 5.7.

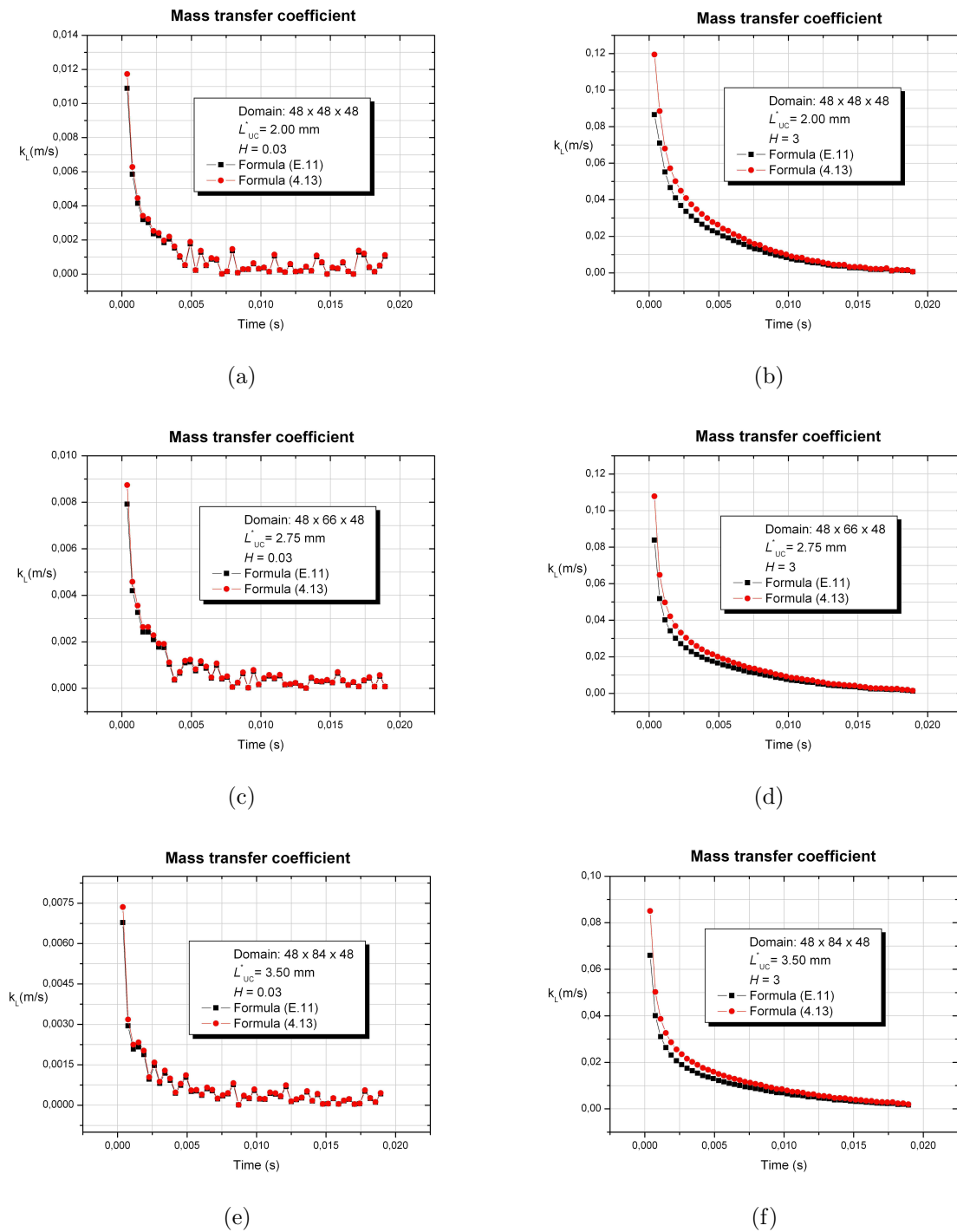Figure 5.8: Comparison between the mass transfer coefficient calculated with formula (4.13) and (E.11) for $L_{\mathrm{UC}}^{\star} = 2$mm (a,b), $L_{\mathrm{UC}}^{\star} = 2.75$mm (c,d) and $L_{\mathrm{UC}}^{\star} = 3.50$mm (e,f) for Henry number $H = 0.03$ (a, c, e) and $H = 3$ (b, d, f)

In Figure 5.8 the mass transfer coefficient evaluated with relations (4.13) and (E.11) is presented. Very good agreement is found between these two formulations provided the case of small variations in the mass transfer coefficient. For systems having $H = 3$ larger mass transfer coefficients are observed, especially at the beginning of the simulations, which are a consequence of the large mass fluxes at the interface. Examining the results it can be roughly estimated that, at the beginning of the mass transfer, increasing the Henry number by a factor of 100 corresponds to an increase in the mass transfer coefficient by a factor of 10.

All the simulations have been performed using the second order central difference scheme (3.42) for the convective term. Figure 5.9 displays the normalized mean gas concentrations for the convective term discretized with the central difference and the upwind scheme for the system having $L_{\mathrm{UC}}^{\star} = 2$mm and $H = 0.03$. As expected, the diffusive character specific to upwind discretization schemes leads to a smaller normalized gas concentration.

The short times considered for mass transfer, i.e $t^{\star} \simeq 0.02$s, justify the employment of periodic boundary conditions, since the bubbles move only a short distance of approximately 2mm.
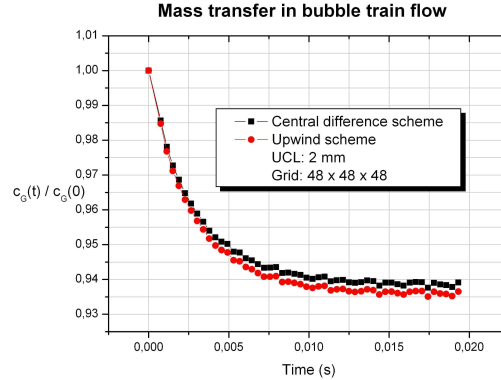

Figure 5.9: Comparison between the central difference scheme and upwind scheme for the convective term ($L_{\mathrm{UC}}^{\star} = 2$mm)

It can be concluded that increasing the length of the unit cell may enhance the mass transfer by increased vortex intensity and, as it is demonstrated in section 5.3, by increased length of the liquid slug. Although the length of the liquid film increases also, the contribution to mass transfer is small, as a consequence of saturation. Inspecting the mass transfer coefficient E.11 it can be observed that it is proportional to the inverse of the interfacial area concentration. Since the unit cell is proportional to the interfacial area concentration, it can be concluded that even in the case of unsaturated liquid film, the long unit cells will not perform better than the small unit cells.

Mass transfer with first order homogeneous chemical reaction

The normalized mean gas concentration distributions in case of mass transfer where the mass is consumed in the liquid by first order homogeneous chemical reaction are displayed in Figure 5.10. The chemical reaction constant used was $k^\star = 1500$ 1/s. It was considered that the chemical reaction takes place only when the solute exceeds 0.015% from the initial gas concentration. As in the case of pure mass transfer, the configuration exhibiting the smaller unit cell proves to be the most efficient. Since more mass is transferred to the continuous phase by small unit cell configurations in comparison with large unit cell systems in the same time unit, the amount of species available for reaction is also larger.

For a first order homogeneous chemical reaction the Damköhler number has been calculated as follows:

$$\mathrm{Da_{Hmg}} = \frac{k^\star_{\mathrm{Hmg}} D_h^{\star 2}}{D_L^\star} = 96.4 \tag{5.7}$$

Unit cell length [mm]	2	2.75	3.50
Reynolds number (liquid)	1.27	1.376	1.39
Schmidt number (liquid)	0.806		
$\mathrm{Da_{Hmg}}$ / ReSc [-]	94.07	86.96	85.84

Table 5.6: ReSc product for first order homogeneous reaction

Since the ratio $\mathrm{Da_{Hmg}}$ / ReSc > 10 for all unit cells considered, as can be observed in Table 5.6, it can be concluded that the chemical reaction is fast [22].
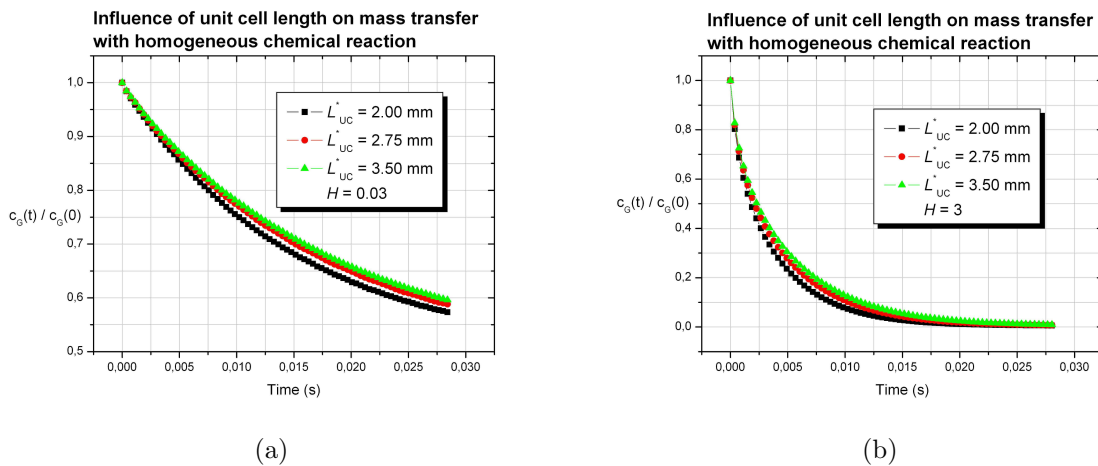

(a)   (b)

Figure 5.10: Influence of the unit cell length on mass transfer with homogeneous chemical reaction for $H = 0.03$ (a) and $H = 3$ (b)

The concentration field in vertical midplane is displayed in Figure 5.11. The concentration scale shown in the left is case specific. For the case $H = 0.03$, the concentration shown in the bubble is the transformed concentration (2.16) that is also used during the integration. For the case with $H = 3$, the non-dimensional concentration field displayed is obtained after transforming back the bubble concentration field. For $H = 0.03$ it can be noticed that the concentration in the liquid slug is homogeneous and has a mean value slightly below the limit at which the chemical reaction occurs. For cases having $H = 3$, the mass in the liquid phase is also homogeneous and does not exceed $c_L^{\alpha\star} = 0.015$ mol/m^3, the value at which it is consumed by reaction.

(a)   (b)   (c)

(d)   (e)   (f)
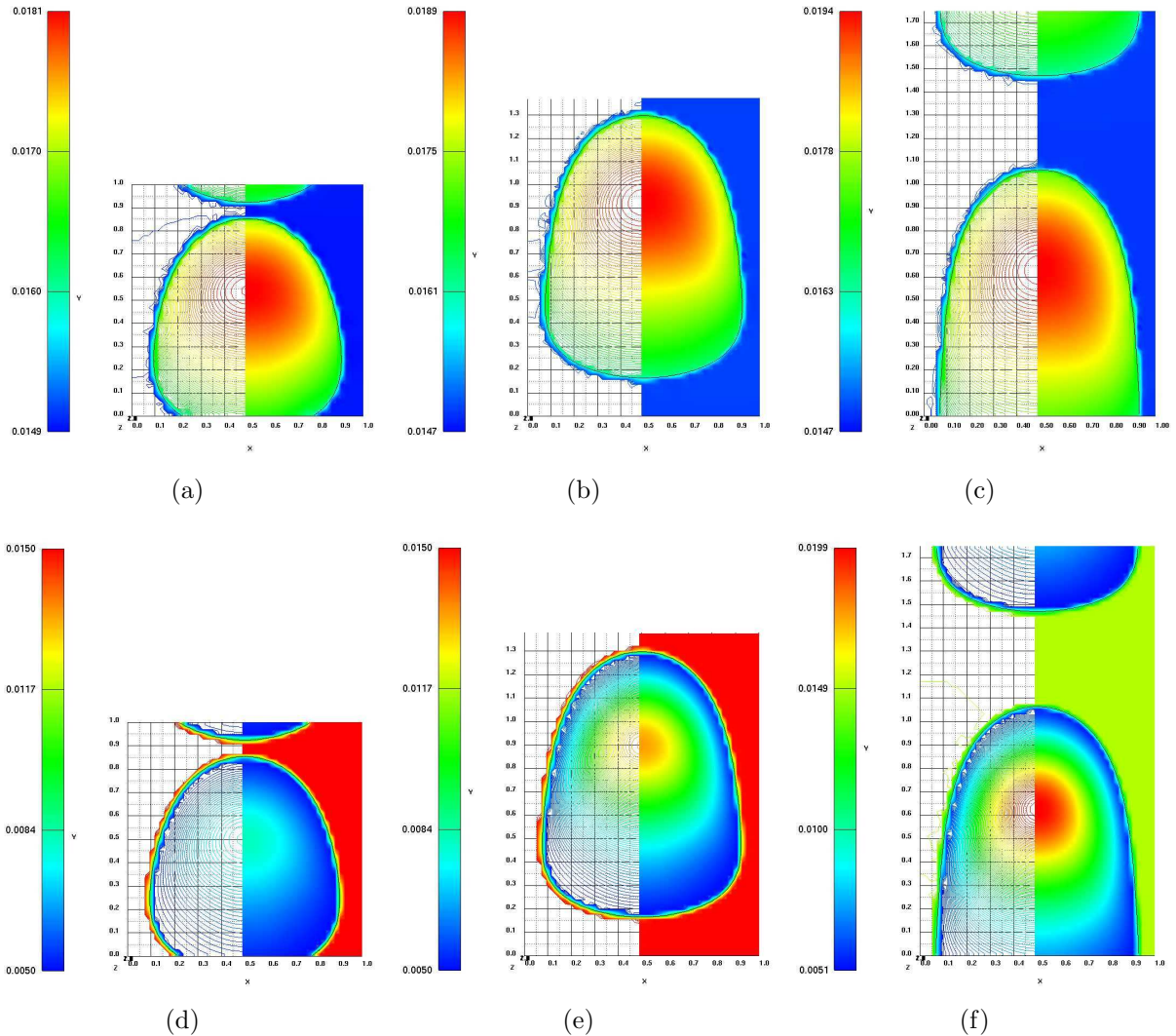
Figure 5.11: Concentration field for $L_{\mathrm{UC}}^\star = 2$mm (a,d), $L_{\mathrm{UC}}^\star = 2.75$mm (b,e) and $L_{\mathrm{UC}}^\star = 3.50$mm (c,f) at $t^\star \simeq 0.03$ s for $H = 0.03$ (a $\div$ c) and $H = 3$ (d $\div$ f) in vertical midplane

Since the bubbles exhibit large interfacial area at the bottom and small interfacial area at the cap, the largest local mass transfer rate can be found at the bottom of the bubble, while the smallest one, at the cap.

Due to the permanent mass consumption, the diffusive mass fluxes are large and dominate over convective mass motion. As a result, no species recirculation in the bubble or in the liquid due to vortices is observed.

The difference between the systems with small H and the systems having large H is the developing of an interfacial concentration gradient attributable to the difference in the species solubility. As mentioned in the previous section, this concentration gradient enhances the diffusive mass transfer in both phases. As a consequence, for $H = 3$ the steady-state mass transfer is obtained much faster than it is the case for configurations with $H = 0.03$.

Mass transfer with first order heterogeneous chemical reaction

For the case of mass transfer with mass consumption by first order chemical reaction at the wall, the normalized mean gas concentration distributions are displayed in Figure 5.12. The chemical reaction constant used is $k^\star = 50 \, \mathrm{m/s}$. One can observe that the systems exhibiting longer unit cells are slightly more efficient in comparison with configurations having shorter unit cells for $H < 1$. Since the liquid film between the bubble and the wall is saturated very rapidly, large amounts of mass are available for the chemical reaction. The unit cell length is proportional to the area contact between the bubble and the wall. Therefore, larger unit cell configurations exhibit larger efficient contact areas than shorter unit cell systems.

For a first order heterogeneous chemical reaction the Damköhler number has been calculated as follows:

$$\mathrm{Da}_{\mathrm{Htg}} = \frac{k^\star_{\mathrm{Htg}} D^\star_h}{D^\star_L} = 1606.68 \tag{5.8}$$

Unit cell length [mm]	2	2.75	3.50
Reynolds number (liquid)	1.27	1.376	1.39
Schmidt number (liquid)	0.806		
$\mathrm{Da}_{\mathrm{Htg}}$ / ReSc [-]	1567.89	1449.27	1430.62

Table 5.7: ReSc product for first order heterogeneous reaction

As can be observed in Table 5.7, the ratio $\mathrm{Da}_{\mathrm{Htg}}$ / ReSc > 10 for all cases considered, meaning that the chemical reaction is fast [22].

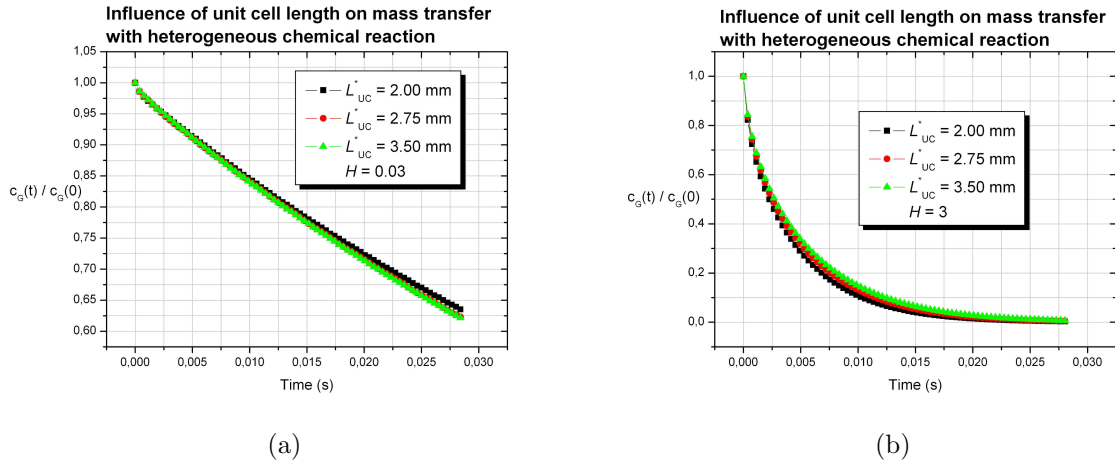(a)   (b)

Figure 5.12: Influence of unit cell length on mass transfer with chemical reaction at the walls for $H = 0.03$ (a) and $H = 3$ (b)

The concentration field along the stream-line direction through the center of the domain is displayed in Figure 5.13. The concentration scale in the left side is case specific. The gas concentration shown in Figure 5.13a÷c represents the concentration used during the integration. In Figure 5.13d÷f is displayed the non-dimensional concentration field. One can notice that in the region where the bubble reaches a maximum in diameter, the concentration in the bubble reaches a minimum, as a consequence of the large local concentration gradient.

In case of $H = 3$, the diffusive mass transfer in the rear of the bubble is large due to the difference in the species solubility and the large interfacial area. The mass transfer is further enhanced by the mass consumption at the wall. For the largest unit cell configuration, due to the combination of these fluxes, the mass is extremely fast transferred from the rear of the bubble leading to a very small local concentration. As a result the mass transfer in the bubble rear decreases significantly. A concentration gradient between the bubble rear and the top of the bubble occurs further. This gradient acts against the convective transport.

In case of small unit cell configuration, the convective transport has a reduced intensity (see Figure 5.2). Therefore, the concentration gradient between the bubble rear and bubble top is more effective in keeping a balanced concentration field within the entire bubble. This behavior provides permanently mass in the rear of the bubble. Therefore, for systems with high solubility, the small unit cell configuration proves slightly more efficient than large unit cell configurations, until steady-state for mass transfer is obtained.

For systems employing chemical reactions, no fluctuations of the normalized mean gas concentration distribution are observed. This signifies that the amount of species transferred is largely consumed by the chemical reaction and no local accumulation of the species is encountered.

Due to the constant and fast mass consumption by reaction, the diffusive mass fluxes

dominate over convective mass motion. Therefore, in the bubble as well as in the liquid no species recirculation due to vortices is observed.
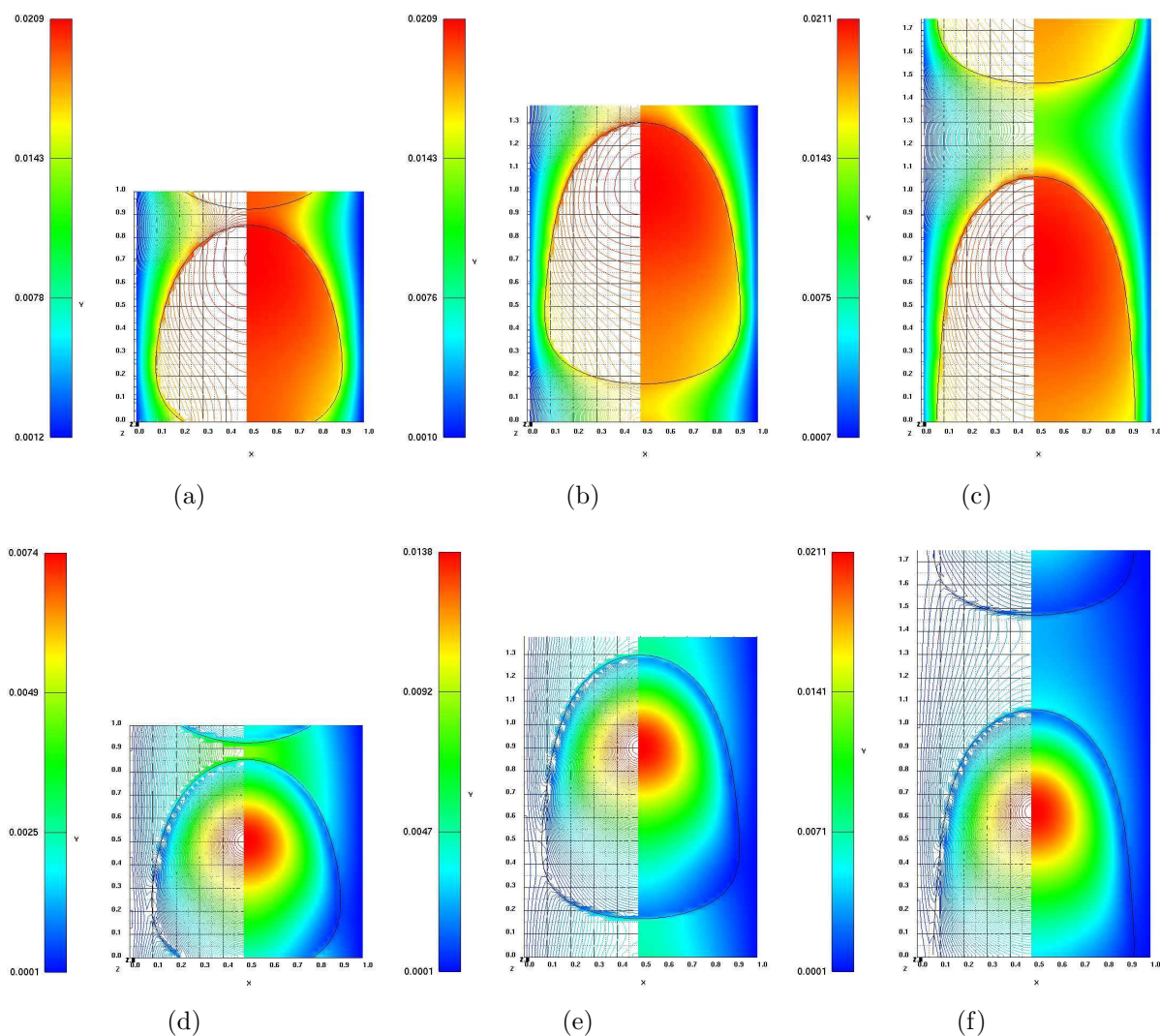

Figure 5.13: Non-dimensional concentration field for $L_{UC}^{\star} = 2$mm (a,d), $L_{UC}^{\star} = 2.75$mm (b,e) and $L_{UC}^{\star} = 3.50$mm (c,f) at time $t^{\star} \simeq 0.03$ s for $H = 0.03$ (a $\div$ c) and $H = 3$ (d $\div$ f) in vertical midplane

The species consumption in the liquid slug increases as the unit cell length increases. This is attributable to the vortex in the liquid slug, which becomes more vigorous with increasing unit cell length. One can also observe in Figure 5.13 that the liquid film between the bubble and the wall has a rather similar contribution to mass transfer as the liquid slug. This is attributable to the short diffusion length, large liquid diffusivity and fast chemical reaction. This result agrees with the experiments of Irandoust and Andersson

[36, 37] who consider that, besides the recirculation in the liquid slug, the influence of the liquid film is also of high importance. This observation is in contrast to the experimental results of Berčič and Pintar [5] who reported that the major part of the reaction occurs on the catalytic wall surface exposed to the liquid slug.

Since in our case the mass transfer is the controlling rate, the variance of the mass transfer coefficient can help in the investigation of the mass transfer mechanism in Taylor flow within narrow devices.

5.3   Influence of liquid slug length on mass transfer process

This section focuses on the influence of the liquid slug length on mass transfer for an arbitrary species. Two unit cell configurations, having the same bubble dimensions, but different liquid slug length, have been considered.

The computational domains, normalized with the reference length $l_{\text{ref}}^{\star} = 0.002$ m, are 1 x 1.375 x 1 and 1 x 1.667 x 1. The domains are discretized by 48 x 66 x 48, respectively by 48 x 80 x 48 uniform cells. The gas volume fraction for each flow configuration is $\varepsilon = 33\%$ and $\varepsilon = 24.76\%$. The coordinate system, physical parameters of the fluids as well as mass transfer parameters are defined as in the previous section, see Table 5.3. A different pressure drop was applied so that each flow configuration should share almost the same bubble velocity, as presented in Table 5.8.

In order to keep the computational time at a reasonable level, a small difference in the liquid slug lengths was considered, at the cost of small differences in the results for mass transfer.

Pure mass transfer

As it can be seen in Figure 5.14a, where the normalized mean gas concentration is presented, the mass transfer process is more efficient for the configuration employing a longer liquid slug. This result confirms the conclusions drawn in the previous section. That is the lateral sides have the smallest contribution to the mass transfer process, while the most part of mass transfer occurs through the cap and bottom side of the bubble. As the liquid slug increases it becomes slower saturated. Therefore, the concentration gradient at the interface decreases slower as in the case of short liquid slug. This can be observed by comparing the concentration field displayed in Figure 5.15a and b. In Figure 5.15 is displayed the transformed concentration field that is used during the integration.

The normalized mean gas concentrations at equilibrium are determined with formula (5.6). As expected, good agreement is found between the normalized mean gas concentration obtained numerically and relation (5.6). The normalized mean gas concentration at equilibrium calculated with (5.6) is $c_G^{\alpha\star\text{eq}}/c_G^{\alpha\star}(0) = 0.94$ for case D and $c_G^{\alpha\star\text{eq}}/c_G^{\alpha\star}(0) = 0.916$ for case E. It can be also noticed that equilibrium is established slightly faster for case D. As a consequence, bubble train flows exhibiting very long liquid slugs can benefit

|	Short liquid slug	Long liquid slug
Case	D	E
Domain [-]	1 x 1.375 x 1	1 x 1.667 x 1
Domain's volume [m^3]	11 x 10^{-9}	13.33 x 10^{-9}
Interfacial area [m^2]	16.24 x 10^{-6}	18.26 x 10^{-6}
Interfacial area concentration [-]	2.95	2.74
Interfacial area concentration [1/m]	1476.45	1369.35
Length of the bubble [mm]	2.27	2.16
Length of the liquid slug [mm]	0.48	1.1732
Bubble velocity $U_B^\star$ [m/s]	0.09934	0.10043
Liquid velocity $U_L^\star$ [m/s]	0.035419	0.04235
Euler number Eu$_{\text{ref}}$ [-]	27.03	35.82
Gas volume fraction ε[%]	33	24.7
Da$_{\text{Hmg}}$ / ReSc	84.7	70.84
Da$_{\text{Htg}}$ / ReSc	1411.67	1180.64

Table 5.8: Flow parameters
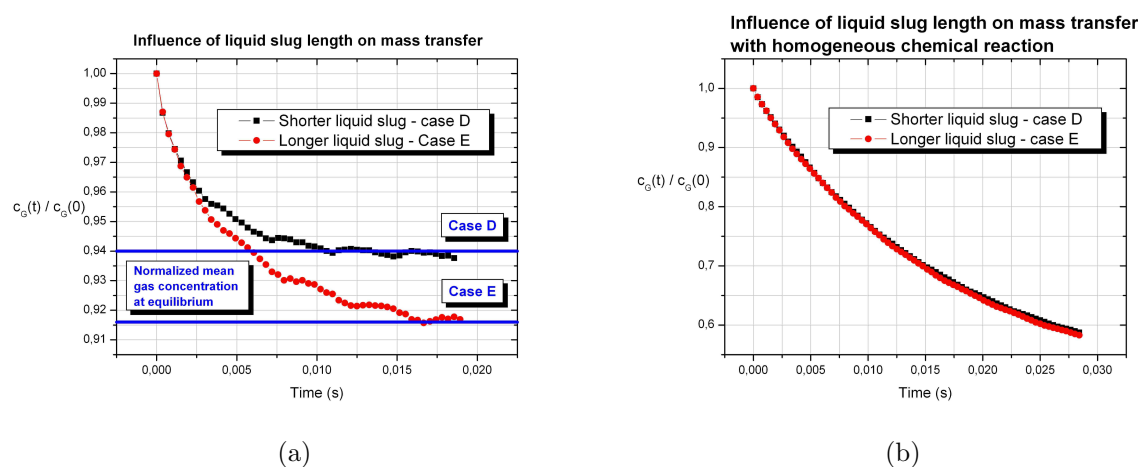
Figure 5.14: Influence of the liquid slug length on pure mass transfer process (a) and on mass transfer with first order homogeneous reaction

from the slower establishment of the equilibrium, since the concentration gradient does not decreases.

The fact that systems with long liquid slugs reach equilibrium faster than systems with short liquid slugs is in good agreement with the formulation of the mass transfer coefficient (E.11), which is inverse proportional to the interfacial area concentration. As
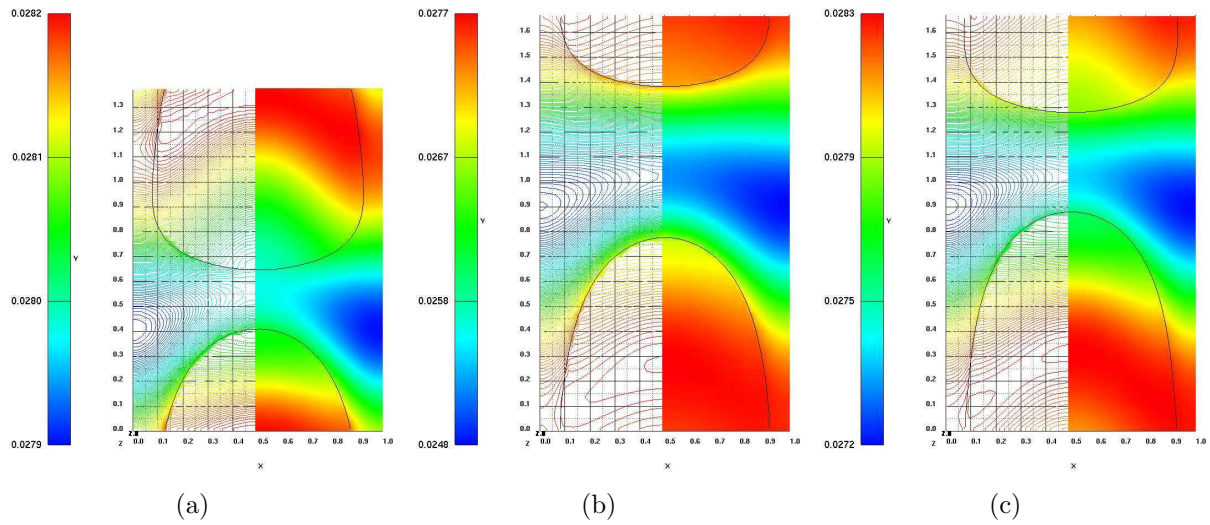
<div style="text-align:center">(a)   (b)   (c)</div>

Figure 5.15: Non-dimensional concentration field for case D (a), case E (b) and case F (c) at time $t^{\star} \simeq 0.02$ s (vertical midplane)

can be observed in Table 5.8, systems having short liquid slugs exhibit larger interfacial area concentration than systems having long liquid slugs. Therefore, the mass transfer coefficient for case D is smaller than for case E, according to relation (E.11).

Mass transfer with first order homogeneous chemical reaction

No significant difference has been observed for various liquid slug lengths on the process of mass transfer with consumption of mass by first order homogeneous chemical reaction. The normalized mean gas concentration for this case is displayed in Figure 5.14b. As in the previous section, the homogeneous chemical reaction takes place only if the amount of species exceeds 0.015% of the initial species concentration in the gas phase. Although the mass transfer process proves to be more efficient for a configuration employing a longer liquid slug, at the initial stage of the simulation no difference between the two configurations is observed. Initially, the mass diffuses throughout the entire liquid slug. As can be observed from Figures 5.15a and b, the liquid slug saturates faster in the system with short liquid slug as in the system having a longer liquid slug. Therefore, the chemical reaction occurs faster in the system with short liquid slug, as predicted also by the ratio Da_{Hmg} / ReSc displayed in Table 5.8. This leads to increased mass consumption for this configuration. The advantage offered by the system with longer liquid slug is that the chemical reaction can occur in a larger volume.

At the initial stage, the longer liquid slug system does not benefit from the advantage of increased mass transfer rate. This configuration can be made more efficient if the amount of the species, required for the chemical reaction to take place, is very small. In this way, the chemical reaction can occur without delay, allowing the longer liquid slug configuration

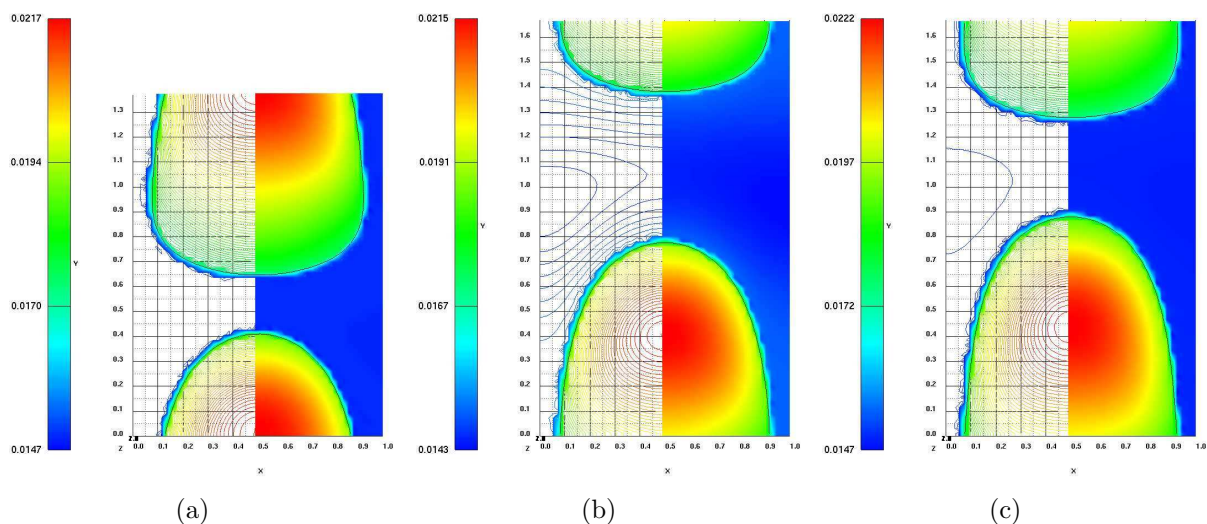to take advantage of the increased mass transfer rate.

Figure 5.16: Non-dimensional concentration field in case of mass transfer with homogeneous reaction for case D (a), case E (b) and case F (c) at time $t^\star \simeq 0.02$ s (vertical midplane)

Figure 5.16a and b, shows the similarity of the concentration patterns between the short and long liquid slug. The bottom part of the bubble contributes most to mass transfer, while the larger concentration zone can be found in the upper part of the bubble. This is a consequence of the bubble shape, exhibiting large interfacial area in the bottom and small interfacial area at the cap. Due to the large concentration gradient at the interface, which is a consequence of the species consumption in the liquid, the influence of the bubble vortex on the bubble concentration distribution is small.

Mass transfer with first order heterogeneous chemical reaction

A small increase in the mass transfer efficiency is observed for the longer liquid slug system in case of mass transfer with mass consumption by first order chemical reaction at the wall, as displayed in Figure 5.17. At the initial stage of the simulation no difference is observed between the normalized mean concentration in the bubble for each length of the liquid slug. As the mass transfer occurs further, the system employing a longer liquid slug takes benefit from the increased mass transfer rate. Since more mass is transferred in the liquid for this configuration, the concentration gradient at the wall is larger than for the shorter liquid slug system. Still, the difference between the normalized mean concentrations is not as large as in the case of purely mass transfer. That is because the larger amount of species transferred in the liquid for the system with $L^\star_{\mathrm{UC}} = 3.33$mm, is transported throughout the entire liquid slug and not only at the wall. At a larger Reynolds number the recirculation within the liquid slug would be more intense and more mass can arrive at the wall, enhancing therefore the mass transfer.
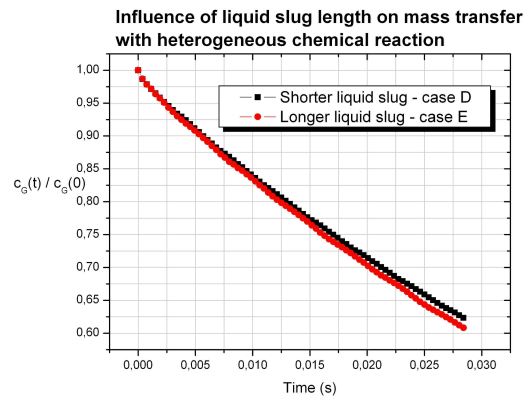
Figure 5.17: Influence of the liquid slug length on mass transfer with first order heterogeneous reaction

The small differences in the normalized mean gas concentrations are attributable also to the fast character of the chemical reaction. As displayed in Table 5.8 the ratio Da_{Htg} / $ReSc > 10$, denoting a fast chemical reaction [22].

In Figure 5.18a and b, where the concentration field for the short and long liquid slug is displayed, one can observe that the larger local mass transfer rate is obtained in the region where the bubble reaches a maximum in diameter.
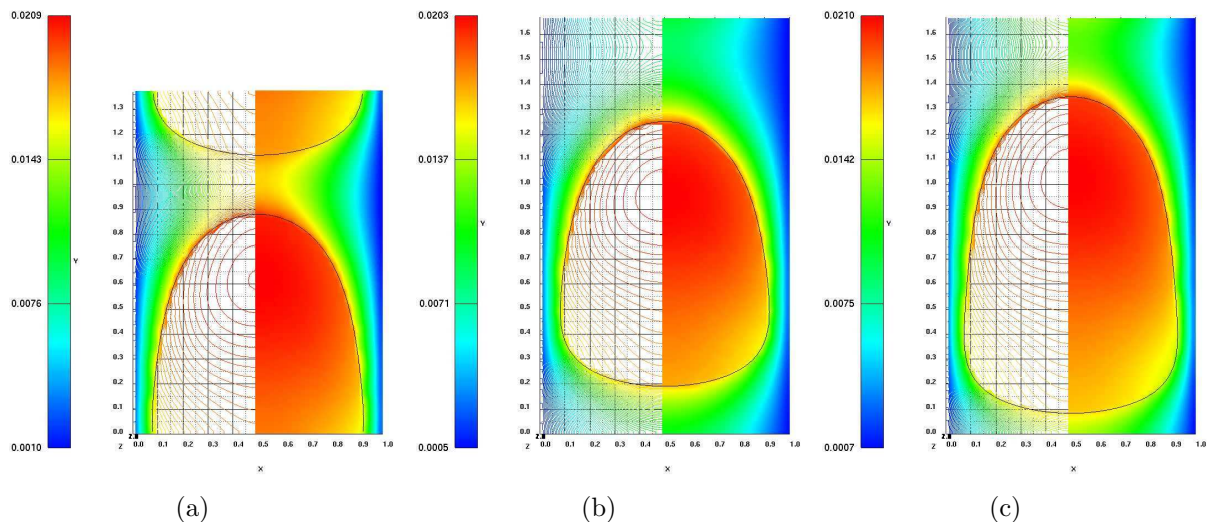

(a)　　　　　　　　　　(b)　　　　　　　　　　(c)

Figure 5.18: Concentration field in case of mass transfer with heterogeneous reaction for case D (a), case E (b) and case F (c) at time $t^{\star} \simeq 0.03$ s (vertical midplane)

5.4 Influence of bubble length on mass transfer process

This section investigates the influence of the bubble length on mass transfer with and without chemical reaction. Two unit cell configurations, having the same length $L_{\text{UC}}^{\star} = 3.33$mm, but different bubble length, have been considered.

The non-dimensional parallelepiped-shaped computational domain, normalized with the reference length $l_{\text{ref}}^{\star} = 0.002$ m, is 1 x 1.667 x 1. The domain is discretized by 48 x 80 x 48 uniform cells. The coordinate system, physical parameters of the fluids as well as mass transfer parameters are employed as in the section 5.2, see Table 5.3. The pressure drop was adjusted to obtain similar bubble velocity for each case, as presented in Table 5.9.

	Short bubble	Long bubble
Case	E	F
Domain	48 x 80 x 48	
Domain's volume [m^3]	13.33 x 10^{-9}	
Interfacial area [m^2]	18.26 x 10^{-6}	22.05 x 10^{-6}
Interfacial area concentration [-]	2.74	3.29
Interfacial area concentration [1/m]	1369.35	1653.38
Length of the bubble [mm]	2.16	2.54
Length of the liquid slug [mm]	1.1732	0.7932
Bubble velocity $U_B^{\star}$ [m/s]	0.10043	0.09937
Liquid velocity $U_L^{\star}$ [m/s]	0.04235	0.03664
Euler number Eu$_{\text{ref}}$ [-]	35.82	26.63
Gas volume fraction ε[%]	24.767	31.899
Da$_{\text{Hmg}}$ / ReSc	70.84	81.88
Da$_{\text{Htg}}$ / ReSc	1180.64	1364.63

Table 5.9: Flow parameters

Pure mass transfer

The normalized mean concentration in the gas phase is displayed in Figure 5.19a. It can be observed that more mass is transferred in the liquid phase, at the same time level, by the system employing a short bubble. This result is in perfect agreement with the one in the previous section, where longer liquid slugs were found more efficient for mass transfer than shorter slugs, since they saturate slower.

The normalized mean gas concentrations at equilibrium are determined with formula (5.6). As expected, the normalized mean gas concentration obtained with `TURBIT-VoF` and the theoretical relation (5.6) agree well. For case F the normalized mean gas concentration

at equilibrium calculated with (5.6) is $c_G^{\alpha\star\,\mathrm{eq}}/c_G^{\alpha\star}(0) = 0.939$. The result confirms also the opinion that the liquid film contributes only slightly to the overall mass transfer. That is due to the rapid species accumulation in the film, as a consequence of small diffusion length. In this way small concentration gradients build up fast in the liquid film, decreasing the mass transfer.

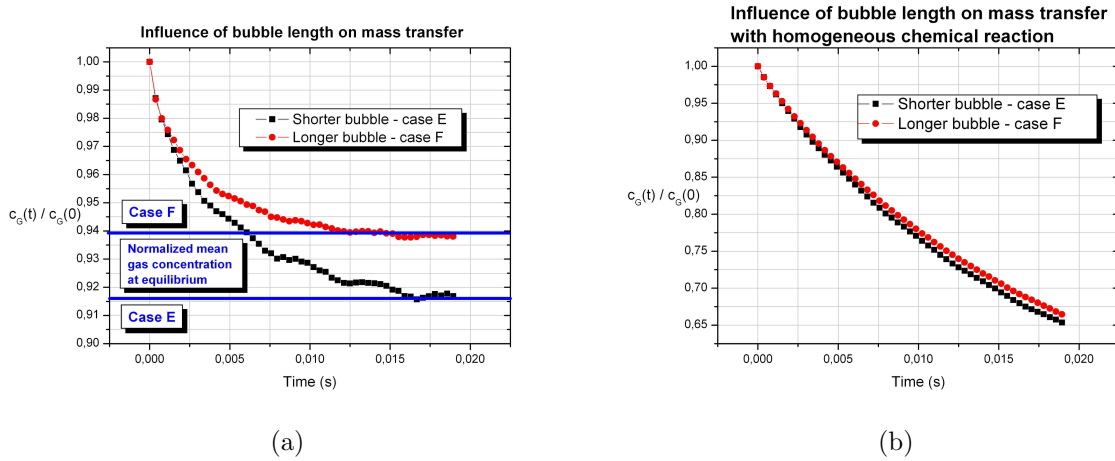(a)   (b)

Figure 5.19: Influence of the bubble length on pure mass transfer (a) and on mass transfer with first order homogeneous chemical reaction (b) for cases E and F

The largest part of the mass transfer occurs in the bottom and upper part of the bubble, as can be seen in Figure 5.15c. A similar result is found by Elperin and Fominykh [19] who investigated theoretically the mass transfer in Taylor flow with small gas bubbles in the liquid slug. It is reported that the contribution of these small bubbles to mass transfer is significantly higher than the contribution of the Taylor bubble.

The result agrees also with the formulation of the mass transfer coefficient (E.11). As can be observed in Table 5.9, case E exhibits a smaller interfacial area concentration than case F. Therefore, the mass transfer coefficient in case E is larger than in case F, explaining the faster approach of the equilibrium state.

Mass transfer with first order homogeneous chemical reaction

As in the previous sections, it is considered that the chemical reaction will occur if the concentration $c_{\lim}^{\alpha\star} = 0.015\,c_G^{\alpha\star}$ is exceeded. Since the ratio $\mathrm{Da_{Hmg}}$ / ReSc displayed in Table 5.9 is larger than 10 it can be concluded that the chemical reaction has a fast character. For the case of shorter bubble, the process of mass transfer accompanied by a first order homogeneous chemical reaction is more efficient than the system with longer bubble, as can be seen in Figure 5.19b. Since more mass is transferred in the continuous phase per time unit for the short bubble case, more mass is available for the reaction. The increase in the efficiency is much smaller as for the pure mass transfer case. This demonstrates

that the increase in the mass transfer rate due to chemical reaction is large. For mass transfer processes that are reaction rate limited and for which the amount consumed is small, it can be assumed that the difference in the normalized concentration will approach the differences observed for the pure mass transfer case.

The concentration distribution presents the same pattern, high concentration in the upper part and low concentration in the bottom part, as the case of short bubble, see Figure 5.16b and c.

Mass transfer with first order heterogeneous chemical reaction

In the case of mass transfer with first order heterogeneous chemical reaction, the system employing a shorter bubble proves to be slightly more efficient than the one with a longer bubble, as shown in Figure 5.20. As in the case of mass transfer with homogeneous chemical reaction, at the initial stage of simulation there is no difference between the normalized concentrations. As amounts of mass arrive at wall, the chemical reaction takes place and a steady concentration gradient builds up. The system employing a shorter bubble takes advantage of the larger amount of mass transferred in the liquid. It is noticeable that if the same liquid slug would be kept, the increase in the bubble length would result in an increase of the mass transferred. This would be a consequence of the rapidly saturated film between the bubble and the wall.

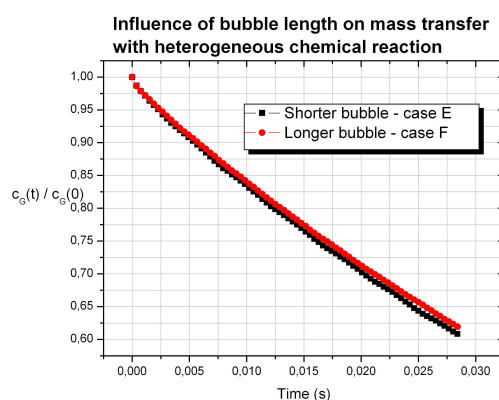The concentration distribution for this configuration is presented in Figure 5.18c.

Figure 5.20: Influence of the bubble length on mass transfer with first order heterogeneous chemical reaction - case E and F

Since the ratio Da_{Htg} / $ReSc$ displayed in Table 5.9 is large the chemical reaction is fast. This explains also the small differences obtained for the normalized mean gas concentration.

5.5   Mass transfer in square and rectangular channels

This section investigates the influence of the channel cross-section on mass transfer with and without chemical reaction. To the author's best knowledge, no similar investigation has been reported up to now. Three unit cell configurations have been considered having square and rectangular-cross sections and a ratio of width to length of 1, 1.25 and 1.6. In order to provide the same basis with respect to mass transfer and flow hydrodynamics all systems share the same gas volume fraction $\varepsilon = 33\%$ and the same hydraulic diameter $D_{\mathrm{h}}^{\star} = 2\mathrm{mm}$.

Case G	Case H	Case I
$(L_x^{\star}/L_z^{\star} = 1.00)$	$(L_x^{\star}/L_z^{\star} = 1.25)$	$(L_x^{\star}/L_z^{\star} = 1.60)$

(a)	(b)	(c)

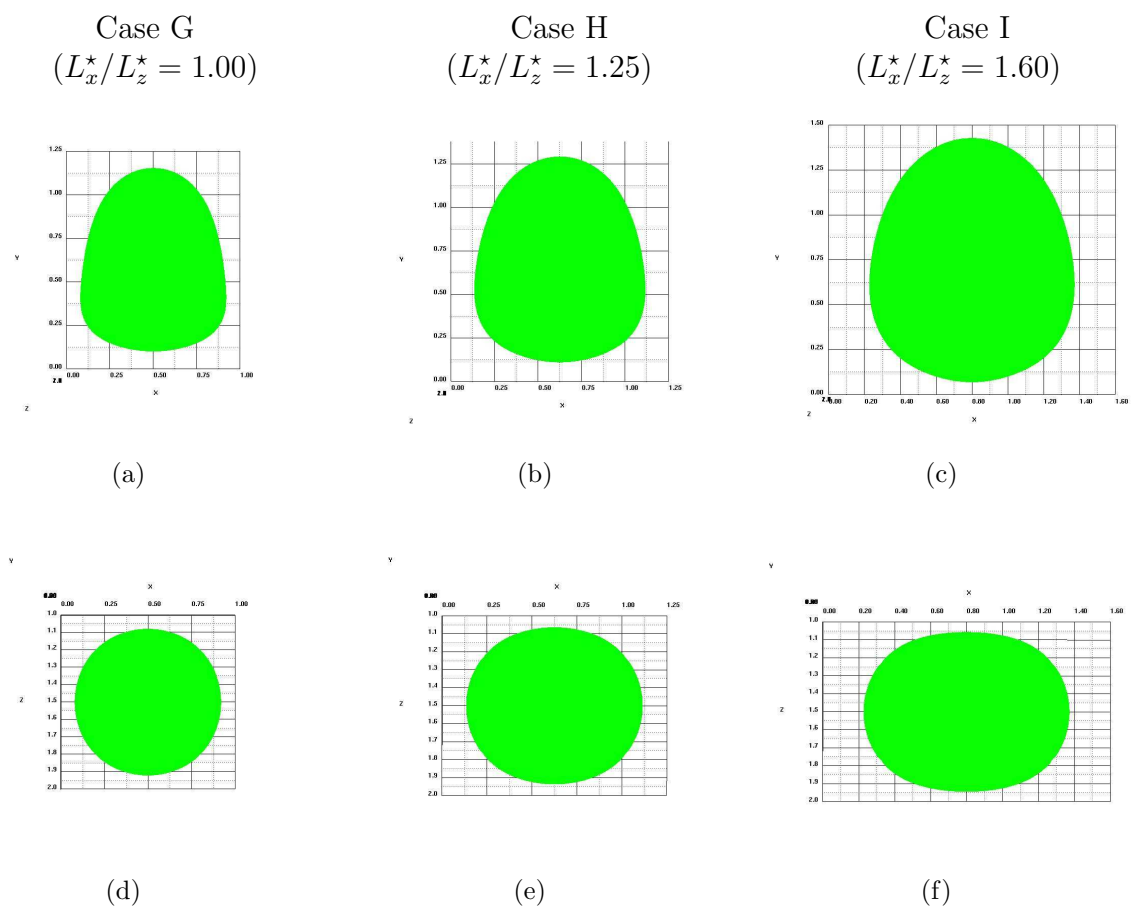| (d)	(e)	(f)

Figure 5.21: Lateral (a ÷ c) and top view (d ÷ f) of the bubble in case G (a, d), H (b, e) and I (c, f). Non-dimensional scale.

The geometry and the hydrodynamic data for each case considered are presented in Table 5.10. In Figure 5.21 are displayed the configuration of the unit cell and the shape of the bubbles. Notice that although the non-dimensional scale is the same, the dimensional size is different due to the difference in the reference length $l_{\mathrm{ref}}^{\star}$. The bubble in the square channel has a circular cross-section, while the bubbles in the rectangular channels have an

ellipsoidal cross-section. It can be observed that the length of the liquid slug decreases with increasing ratio of width to length, since the bubble deforms significantly along x axis. In axial direction it can be noticed that, as the ratio of the width to length increases, the bottom of the bubbles becomes more rounded.

The coordinate system, the physical parameters of the fluids as well as mass transfer parameters are employed as in Table 5.3, with the only difference that the Henry number considered is $H = 0.03$. The pressure drop was adjusted to obtain a similar bubble velocity for each case, as presented in Table 5.10. Therefore, a constant product $\mathrm{ReSc} = D_h^\star U_B^\star / D_{\mathrm{ref}}^\star$ is obtained for every channel configuration.

In the square channel, due to the constant circular shape of the bubble cross-section, the liquid film has the same thickness in both x and z directions. In the rectangular channels, the thickness of the liquid film is smaller than the one in the square channel in z direction and significantly larger in x direction.

Domain	Square	Rectangular	Rectangular
Case	G	H	I
Width / length [-]	1	1.25	1.6
Grid	48 x 60 x 48	60 x 66 x 48	64 x 60 x 40
Reference length $l_{\mathrm{ref}}^\star$ [m]	0.002	0.0018	0.001625
Unit cell [-]	1 x 1.25 x 1	1.25 x 1.375 x 1	1.6 x 1.5 x 1
Unit cell [mm]	2 x 2.5 x 2	2.25 x 2.475 x 1.8	2.6 x 2.4375 x 1.625
Domain's volume [m^3]	10^{-8}	1.024×10^{-8}	1.029×10^{-8}
Interfacial area concentration [-]	2.68	3.39	4.28
Interfacial area concentration [1/m]	1340	1883.3	2633.8
Interfacial area [m^2]	1.34×10^{-5}	1.887×10^{-5}	2.712×10^{-5}
Bubble length [mm]	2.1	2.115	2.215
Liquid slug length [mm]	0.4	0.36	0.22
Bubble velocity $U_B^\star$ [m/s]	0.09557	0.09625	0.09557
Liquid velocity $U_L^\star$ [m/s]	0.03416	0.03329	0.03036
Reference Euler $\mathrm{Eu}_{\mathrm{ref}}$ [-]	27.03	24.00	21.24
Reaction constant $k_{\mathrm{Hmg}}^\star$ [1/s]	1500		
Reaction constant $k_{\mathrm{Htg}}^\star$ [m/s]	50		
$\mathrm{Da}_{\mathrm{Hmg}}$ / ReSc	87.82	90.12	98.81
$\mathrm{Da}_{\mathrm{Htg}}$ / ReSc	1463.7	1501.95	1646.9

Table 5.10: Flow parameters for the study of channel aspect ratio on mass transfer

Pure mass transfer

The normalized mean gas concentration obtained with `TURBIT-VoF` and the normalized mean gas concentration at equilibrium determined with formula (5.6) are displayed in Figure 5.22. Good agreement is found between these two distributions. It can be observed that increased mass transfer is obtained for low values of the width to length ratio. For scenario H a larger bubble velocity was obtained, which may justify the smaller normalized mean gas concentration.
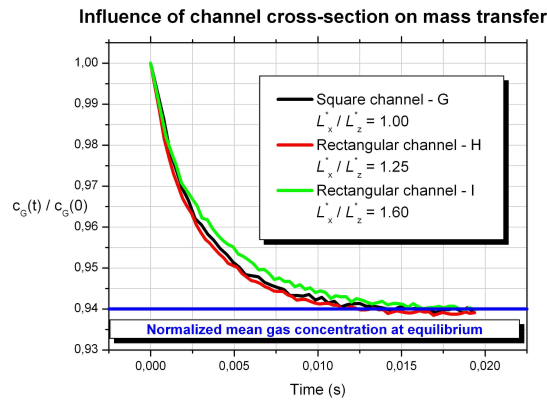
(a)

Figure 5.22: Normalized mean gas concentration distribution at time $t^\star \simeq 0.02$ s for cases G, H and I

The concentration distribution in vertical midplane is presented in Figure 5.23. The concentration scale in the left side is case specific. The gas concentration shown represents the concentration used during the integration, which is continuous at the interface. In order to obtain the non-dimensional gas concentration one needs to divide the concentration in the bubble with the Henry number $H = 0.03$. The concentration displayed for the liquid phase represents the non-dimensional liquid concentration.

It can be observed in Figure 5.21 that as the ratio $L_x^\star/L_z^\star$ increases, the thickness of the liquid film between the bubble and the wall decreases along z axis and increases significantly in x direction. Therefore, the liquid film reaches saturation slightly faster along z axis as the ratio $L_x^\star/L_z^\star$ increases. The rectangular channels benefit from enhanced mass transfer along the width of the channel, where the film does not reach saturation. In rectangular channels the bubbles exhibit ellipsoidal cross-sectional shape and increased surface in close proximity to the wall as compared to square channels. As a consequence, the bubbles in rectangular channels have larger inefficient surface in which the liquid film becomes fast saturated. Another disadvantage of the rectangular channels for mass transfer processes is the decreasing of the liquid slug length with increasing ratio of width to length. As seen in section 5.3 this issue contributes to the decrease of the mass transfer.
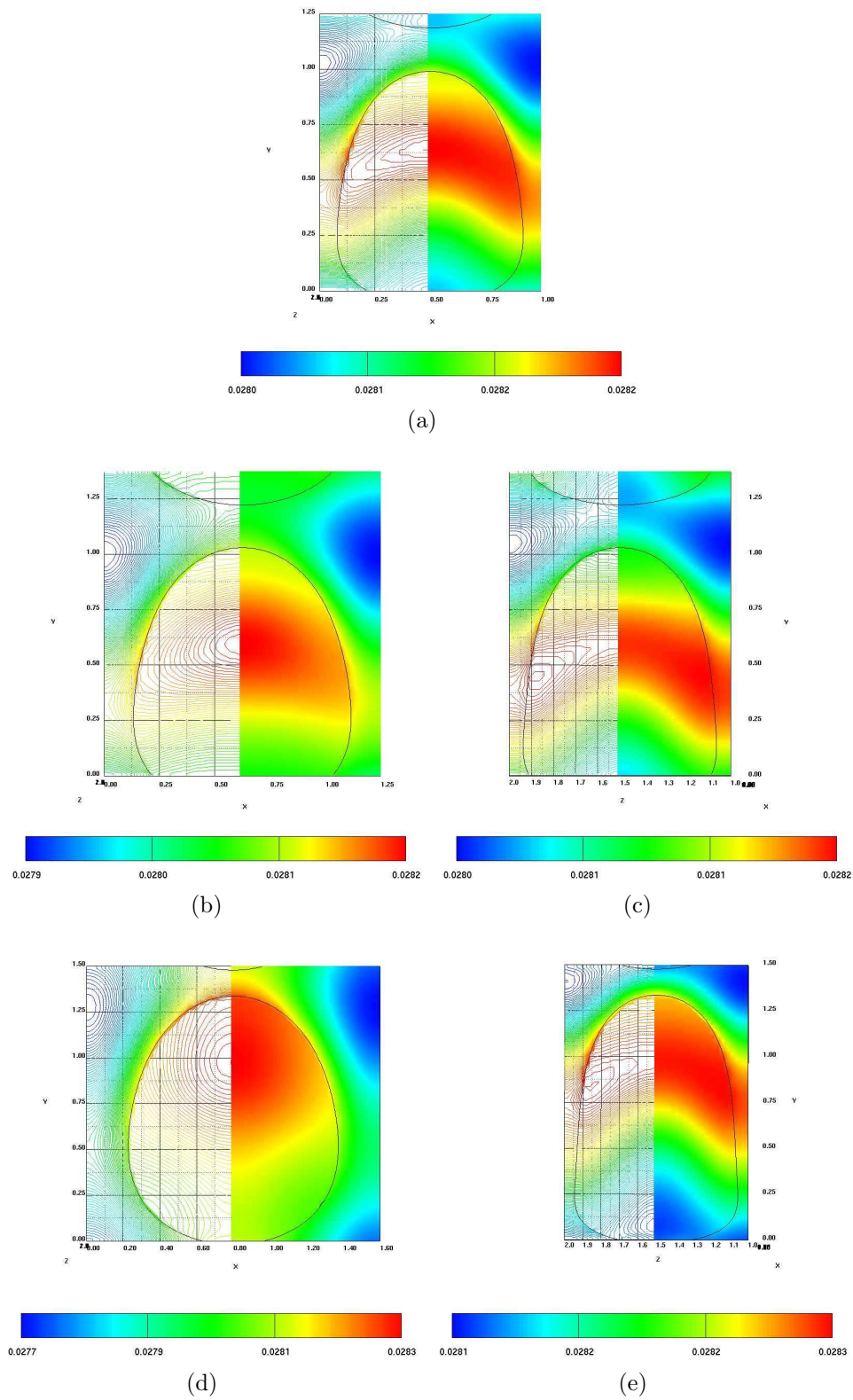
Figure 5.23: Influence of the channel aspect ratio on mass transfer: case G (a), case H - vertical midplane along x (b) and z (c) axis and case I - vertical midplane along x (e) and z (f) axis

Similar to the results obtained in section 5.2, the rear and the top of the bubble contribute to the major part of mass transfer, as can be observed in Figure 5.23a-c. When the length of the liquid slug decreases significantly, as in case I, the contribution of the top of the bubble to the mass transfer decreases, since the liquid slug becomes saturated from the amount of species transferred from the bottom of the ahead rising bubble. This situation, displayed in Figure 5.23d,e, has been also observed in section 5.2, for the case of short unit cell (see Figure 5.6a,d).

Another similarity with the previous results is that the system having the smallest interfacial area concentration, i.e. case G, reaches equilibrium in the shortest time. This result is explained by the fact that the mass transfer coefficient (E.11) is inverse proportional to the interfacial area concentration.

Mass transfer with first order homogeneous chemical reaction

The normalized mean gas concentration in the case of mass transfer with mass consumption by first order homogeneous reaction in the liquid phase is displayed in Figure 5.24. As considered also in the previous sections within this chapter that deal with mass transfer accompanied by homogeneous reaction, the chemical reaction constant is $k_{\mathrm{Hmg}}^{\star}$ = 1500 1/s and the species is consumed by chemical reaction only when the solute exceeds 0.015% from the initial gas concentration. It can be observed in Figure 5.24 that rectangular channels tend to transfer more mass in the liquid phase. In x direction the rectangular channels exhibit a larger region closed to the wall, where the liquid film becomes fast saturated, than square channels. Therefore, within this liquid film, the chemical reaction occurs faster and within a larger volume, as opposite to square channels. This issue can constitute the key factor for the increased mass consumption by chemical reaction in rectangular channels.
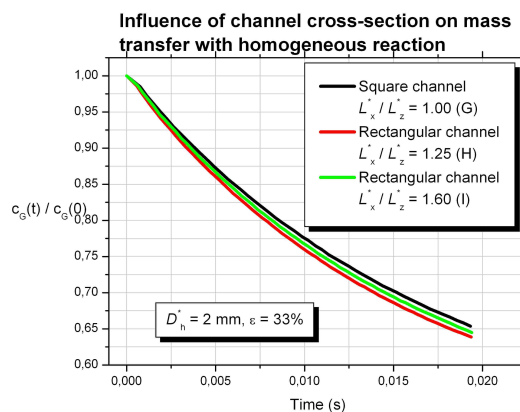

Figure 5.24: Influence of the channel aspect ratio on mass transfer with homogeneous reaction
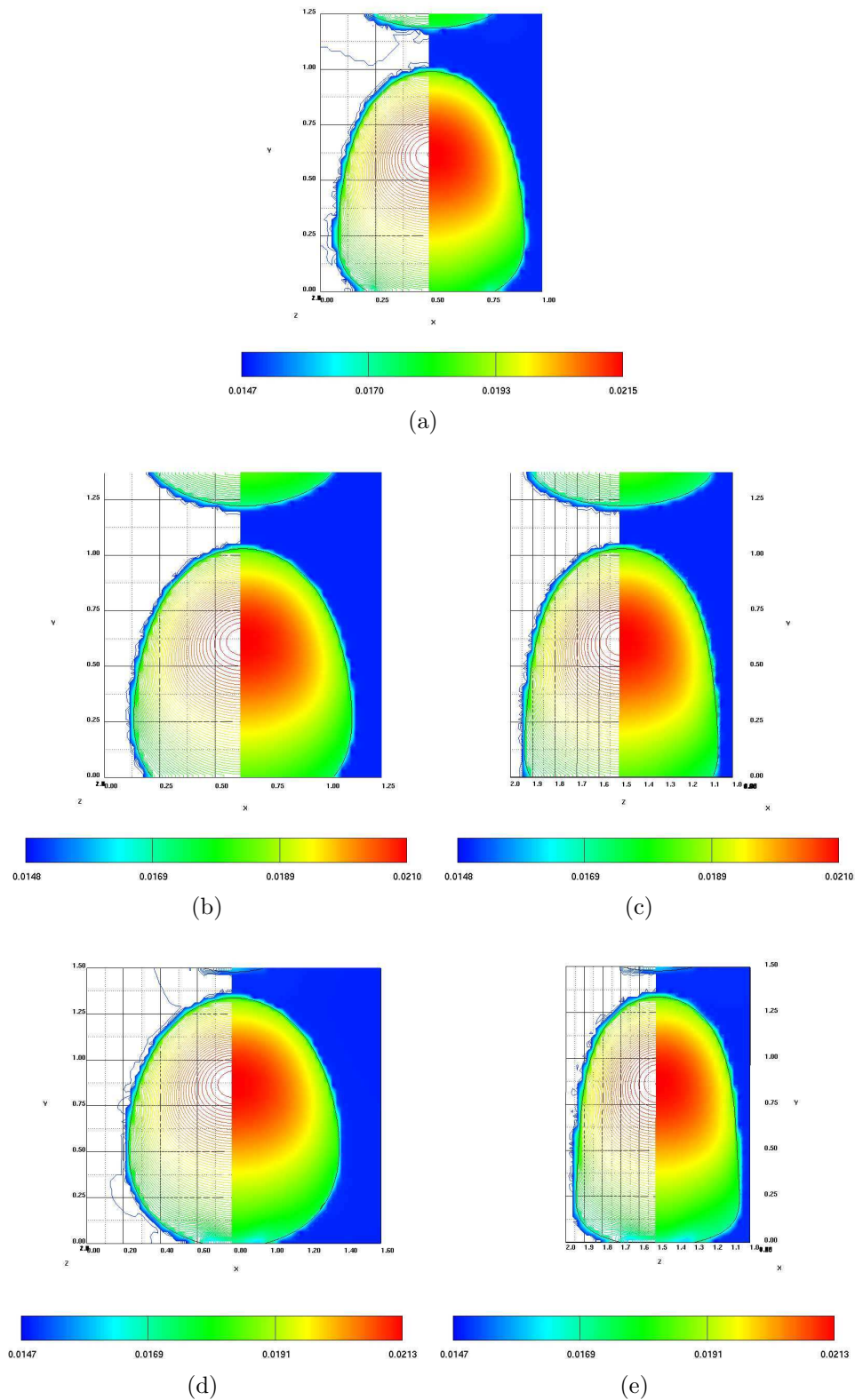
Figure 5.25: Influence of the channel aspect ratio on mass transfer accompanied by homogeneous reaction at time $t^\star \simeq 0.02$ s. Case G (a), case H - vertical midplane along x (b) and z (c) axis, case I - vertical midplane along x (d) and z (e) axis

The result obtained suggests that in case of mass transfer in mini-channels having different aspect ratios the occurrence of the chemical reaction has a much more influence than in case of mass transfer in unit cells of different lengths. Despite the largest interfacial area concentration, which is not a benefit for mass transfer problems, in rectangular channels having large aspect ratio more mass is transferred into the continuous phase than in channels of low aspect ratio.

Since the physical properties of the species have been kept constant, the Damköhler number (5.7) is $Da_{Hmg} = 96.4$, similar to the previous cases investigated which considered homogeneous reaction. The ratio $Da_{Hmg} / ReSc > 10$, as seen in Table 5.10, suggesting that the chemical reaction has a fast character.

The larger bubble velocity obtained for case H can potentially enhance the mass transfer by convection, leading to a smaller normalized mean gas concentration, as observed in Figure 5.24.

The non-dimensional concentration field in vertical midplane is displayed in Figure 5.25. The concentration scale shown below is case specific. The concentration displayed in the bubble is the concentration (2.16) that is used during the integration. The non-dimensional concentration in the dispersed phase can be obtained if the concentration displayed is divided by Henry number H. It can be observed that all cases exhibit a similar concentration pattern. The major contribution to mass transfer is made through the bottom part of the bubble. The chemical reaction dominates over diffusion and convection and, as a consequence, no species recirculation within the bubble and in the liquid slug is observed.

Mass transfer with first order heterogeneous chemical reaction

In case of mass transfer with species consumption at the walls by first order chemical reaction, the normalized mean gas concentration is displayed in Figure 5.26.
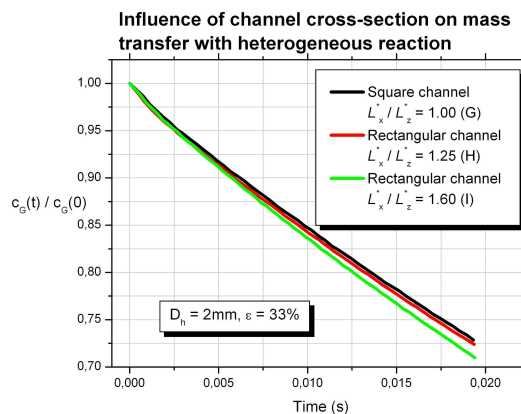

Figure 5.26: Influence of the channel aspect ratio on mass transfer with heterogeneous reaction
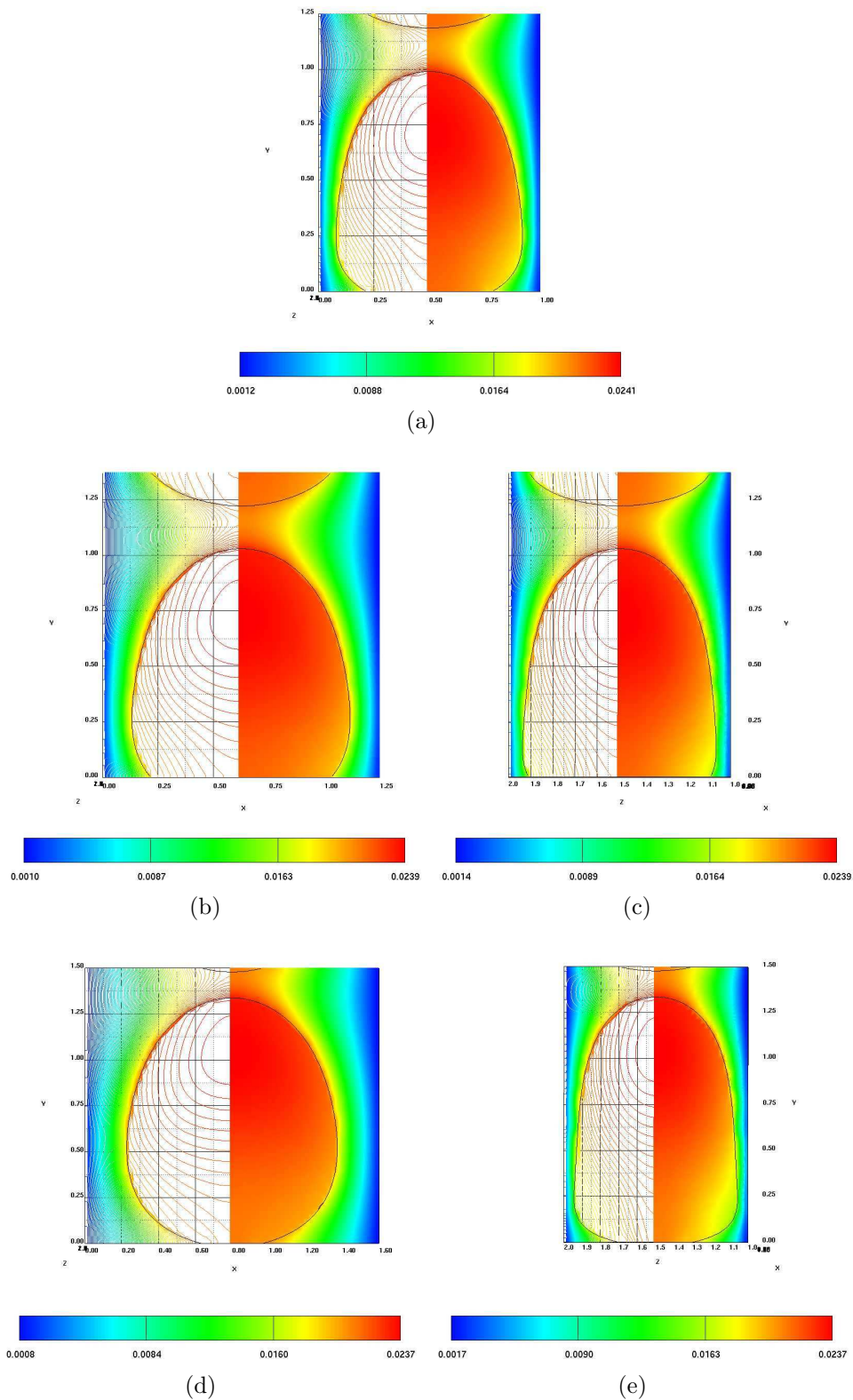
Figure 5.27: Influence of the channel aspect ratio on mass transfer with heterogeneous reaction at time $t^\star \simeq 0.02$ s Case G (a), case H - vertical midplane along x (b) and z (c) axis, case I - vertical midplane along x (d) and z (e) axis

The constant of the chemical reaction is $k_{\mathrm{Htg}}^{\star} = 50$ m/s.

Similar to the previous results obtained in this section, it can be observed that, as the ratio of width to length increases, more mass is transferred into the continuous phase.

The result suggests that the channel aspect ratio has a qualitatively and quantitatively different influence on mass transfer with heterogeneous chemical reaction than the unit cell. Despite exhibiting larger interfacial area concentration, in large aspect ratio rectangular channels more mass is consumed by chemical reaction in the continuous phase than in channels of low aspect ratio.

The transformed concentration distribution, which is employed during the integration, is presented in Figure 5.27. The non-dimensional concentration in the dispersed phase can be obtained by division of the concentration with Henry number H. The concentration in the continuous phase is non-dimensional.

In Figure 5.21 it can be observed that, as the ratio $L_x^{\star}/L_z^{\star}$ increases, the thickness of the liquid film between the bubble and the wall decreases along the length of the cross-section. Furthermore, along the width of the channel, rectangular channels exhibit a larger flatter interfacial area in closed proximity to the wall. Both these issues enhances the mass consumption at the wall since the diffusion length decreases.

Since the ratio $\mathrm{Da}_{\mathrm{Htg}} / \mathrm{ReSc} > 10$, as seen in Table 5.10, the heterogeneous chemical reaction is fast. Similar to the previous case of mass transfer with homogeneous chemical reaction, all cases exhibit a resembling concentration pattern. No species recirculation within the bubble or in the liquid slug can be observed, since the chemical reaction at the wall is fast and dominates over diffusion and convection.

Chapter 6

Summary and conclusions

The present study explores the process of mass transfer with and without first order chemical reaction in two-fluid systems. The investigations performed are based on the implementation of the species conservation equation in computer code `TURBIT-VoF`. One of the goals of this research was the exploration of mass transfer mechanisms from the dispersed phase towards the continuous phase in segmented two-fluid flows performed in narrow channels. For this purpose the investigations performed focused on studying the influence of the unit cell length, liquid slug length and bubble length on the mass transfer process. Interesting results are reported also for the influence of the channel cross-section on mass transfer.

The implementation of the species conservation equation in computer code `TURBIT-VoF` was successfully validated against analytical solutions. The validation of the implementation was focused on each term from the species conservation equation and the concentration field was considered without feedback on the flow field. The validation of the diffusive term revealed that systems exhibiting species having a large solubility in the solvent require a fine grid to accurately capture the high concentration gradients that build up in the concentration boundary layer. Another conclusion that can be drawn from this test is that the approximation employed to express the mean diffusivity at the interface underestimates the interfacial molar flux for large values of the diffusivities ratio $D_G^\star/D_L^\star$. As a consequence, the concentration field in the continuous phase is underestimated, while the concentration field in the dispersed phase is overestimated. For the testing of the convective term, the mass transfer of a rising 4mm oxygen bubble in a mixture of water and glycerol was simulated and compared against another numerical simulation reported in literature. Very good agreement has been obtained for the hydrodynamical aspects of the flow, i.e. bubble velocity, bubble aspect ratio and bubble shape, suggesting that the viscous boundary layer was correctly resolved. The mass transfer was considered at a large Schmidt number, i.e. Sc = 100, that implies a thin concentration boundary layer as a consequence of reduced interfacial molar flux. The length of the cell used in the simulation exceeded the Kolmogorov and Batchelor length scales, resulting in a less accurate capture of the concentration boundary layer. Therefore, the length and the width of the concentration wake are overestimated. Nevertheless, the concentration wake has the same structure as reported by Bothe et al.

[8] and Koynov et al. [45]. Very good agreement with the analytical solutions was obtained for the validation of the source term, for both types of the first order chemical reactions that were considered.

One of the demanding tasks was the treatment of the diffusivity at the interface between phases. The difficulty wells from the discontinuous character of the concentration at interface. It is assumed that equilibrium is instantaneously established at interface and it is described by means of Henry's law. The physically discontinuous concentration field was transformed and a continuous field was used during the integration. As a result of this transformation, the interfacial jump was shifted from the concentration field into the normal interfacial mass flux. Two formulations of the cell face diffusivity were implemented after proper modification to account for the interfacial jump. No significant differences are reported in the results obtained with these cell face formulations. In all simulations the centered-scheme was used for the discretization of the convective term. Although implemented, the first order upwind scheme has a diffusive character and was not employed.

A formulation of the normalized mean gas concentration at equilibrium is proposed. Excellent agreement is found between this formulation and the data obtained with computer code `TURBIT-VoF` for mass transfer processes.

The present research was focused on bubble train-flows in co-current flow operated in mini-channels having the hydraulic diameter of about 1mm. Since bubble train flow exhibit periodic flow conditions in axial direction, the analysis was restricted to a unit cell of the flow field consisting of one bubble and one liquid slug. For the flow hydrodynamics, good agreement is obtained in terms of non-dimensional bubble diameter, ratio of bubble velocity to the total superficial velocity and relative velocity in comparison with experimental data reported in [80]. The investigations performed on the influence of the unit cell length on mass transfer revealed that short unit cells are more more efficient than long unit cells for the case of mass transfer and mass transfer with species consumption by homogeneous chemical reaction. The thin liquid film separating the bubble from the wall represents a region were mass is rapidly accumulating due to short diffusion length and long contact time. The unit cell length is direct proportional to the volume of this region, which contains a small concentration gradient. Therefore, long unit cells exhibit a larger inefficient surface for mass transfer than short unit cells. The result obtained shows the same tendency with the study performed by van Baten and Krishna [87]. On the contrary, for the case of mass transfer with species consumption at the wall, the large film region specific for long unit cells provides constantly larger amounts of species for the reaction than short unit systems. Still, this mechanism is encountered only for species exhibiting a low solubility in the solvent, i.e. small Henry number H. In flows with larger species solubility in the continuous phase, diffusion dominates over reaction and the short unit cell systems transfer more mass than long unit configurations, as previously mentioned in the case of pure mass transfer. A mass transfer coefficient is proposed, based on the mean concentrations within the phases. In this way, the difficulties encountered by considering the concentration in the bulk phase or the interfacial concentration are circumvented. For the case of pure mass transfer, the visualization of the concentration field reveals that the cap and the bottom of the bubble contribute to the major part of mass transfer. This conclusion agrees with

the results reported by Berčič and Pintar [5]. Since short times are considered for the simulation of mass transfer, the implementation of periodic boundary conditions for the concentration field in axial direction is justified.

The investigation of the influence of liquid slug length on mass transfer shows the same qualitative agreement with the work performed in [5]. For mass transfer with species consumption by chemical reaction in the bulk phase or at the walls, long liquid slug configurations tend to be more efficient than short liquid slugs. The small differences obtained for the normalized mean gas concentration for these two cases are explained by the small Reynolds number exhibited by the flows and the small differences in the length of the liquid slug. For larger Reynolds number or longer liquid slugs, the recirculation within the liquid slug would be more vigorous, enhancing therefore the mass transfer for systems with long liquid slugs. In complete agreement with the results previously mentioned, configurations having short bubbles, i.e. longer liquid slugs, are found more efficient than systems with long bubbles.

Interesting results are presented also for the study of the influence of channel cross-section on mass transfer. To the author's knowledge no study on this topic has been up to now published. The simulations were performed for different ratios of width to length, while keeping constant the hydraulic diameter, the gas volume fraction and the bubble velocity. The results show increased mass transfer for systems having small width to length ratio. As the ratio of the width to length increases, the bubble becomes more flatted along the width of the channel, exhibiting an ellipsoidal cross-section. Due to the bubble deformation rectangular channels present increased bubble surface in close proximity to the wall as compared to square channels. As a consequence, in rectangular channels, the bubbles have large inefficient surface due to fast film saturation, while in case of mass transfer with homogeneous chemical reaction this issue represent an advantage since the reaction occurs faster and within a larger volume. For the case of mass transfer with chemical reaction at the wall this issue constitutes also an advantage, since more mass can be transported towards the walls due to short diffusion lengths.

Based on the investigations performed on the numerical simulations of mass transfer in bubble train flow it can be concluded that:

1. Equilibrium state in the dispersed phase is achieved extremely fast within the narrow channels considered for mass transfer processes. The equilibrium condition is found dependable on Henry number and the gas volume fraction. The time in which equilibrium state is established is dependent on the unit cell length, liquid slug length, bubble length and channel cross-section. Although not investigated within this work, the ratio of the diffusivities and the bubble velocity are considered to greatly influence the time in which equilibrium is achieved.

2. Long liquid slugs and short bubbles are responsible for mass transfer enhancement in bubble train flows operated within narrow channels.

3. The mass transfer mechanism differs qualitatively and quantitatively from the mechanism of mass transfer accompanied by chemical reaction. The thin liquid film devel-

oped between the bubble lateral side and the wall as well as the vortex in the liquid slug represent the key factors for the large mass transfer rates observed in case of mass transfer with chemical reaction at the wall.

4. Rectangular channels may be best suited for mass transfer accompanied by chemical reaction in the bulk of the continuous phase or at the wall.

5. The interfacial area concentration is found to be inverse proportional to the mass transfer coefficient, suggesting therefore that the species contained in small bubbles is transferred faster in the continuous phase than the species contained within large bubbles.

The results obtained in this work serve for the optimization of mass transfer processes with and without first order chemical reaction operated in micro-fabricated systems such as micro-bubble columns and monolithic catalyst flow reactors.

Bibliography

[1] W. M. Adekojo, M. Henschke, and A. Pfennig. Mass transfer by free and forced convection from single spherical liquid drops. *International Journal of Heat and Mass Transfer*, **45**(22):4507–4514, 2002.

[2] J.D. Anderson Jr. *Computational fluid dynamics*. McGraw-Hill, Inc., 1995.

[3] A. Apelblat. Mass transfer with a chemical reaction of the first order: analytical solutions. *Chemical Engineering Journal*, **19**:19–37, 1980.

[4] K. H. Baumann and K. Mühlfriedel. Mass transfer and concentration profiles near phase boundaries. *International Journal Thermal Science*, **40**:425–436, 2001.

[5] G. Berčič and A. Pintar. The role of gas bubbles and liquid slug lengths on mass transport in the Taylor flow through capillaries. *Chemical Engineering Science*, **52**(21-22):3709–3719, 1997.

[6] R. B. Bird, W. E. Stewart, and E. N. Lightfoot. *Transport phenomena*. John Wiley & Sons, 2nd edition, 2002.

[7] D. Bothe, M. Koebe, K. Wielage, J. Prüss, and H. J. Warnecke. Direct numerical simulation of mass transfer between rising gas bubbles and water. In M. Sommerfeld, editor, *Bubbly flows. Analysis, Modelling and Calculation*, pages 159–174. Springer Verlag, 2004.

[8] D. Bothe, M. Koebe, K. Wielage, and H. J. Warnecke. VoF-simulations of mass transfer from single bubbles and bubble chains rising in aqueous solutions. Proceedings of FEDSM2003-45155: 4th ASME_JSME Joint Fluids Engineering Conference, Honolulu, USA, ASME 2003.

[9] H. Brauer. Unsteady state mass transfer through the interface of spherical particles. Physical and mathematical description of the mass-transfer problem. *International Journal of Heat and Mass Transfer*, **21**:445–453, 1978.

[10] J. Crank. *The mathematics of diffusion*. Oxford - Clarendon Press, 2nd edition, 1994.

[11] E.G. Cussler. *Diffusion. Mass transfer in fluid systems.* Cambridge University Press, 2nd edition, 1997.

[12] P. V. Danckwerts. *Gas-liquid reactions.* MacGraw-Hill, 1970.

[13] P.V. Danckwerts. Significance of liquid-film coefficients in gas absorption. *Industrial and Engineering Chemistry*, **43**:1460–1467, 1951.

[14] M. R. Davidson and M. Rudman. Volume-of-fluid calculation of heat or mass transfer across deforming interfaces in two-fluid flow. *Numerical Heat Transfer B*, **41**:291–308, 2002.

[15] S. R. de Groot. *Thermodynamics of irreversible processes.* North-Holland, Amsterdam, 1951.

[16] D. A. Drew and S. L. Passman. *Theory of multicomponent fluids.* Springer Verlag, 1999.

[17] S. Dănăilă and C. Berbente. *Metode numerice în dinamica fluidelor.* Editura Academiei Române, 2003 (in Romanian).

[18] T. Elperin and A. Fominykh. Two models of fluid flow and mass transfer at the trailing edge of a gas slug. *International Journal of Heat and Mass Transfer*, **38**(18):3341–3347, 1995.

[19] T. Elperin and A. Fominykh. Combined mass and heat transfer during nonisothermal absorption in gas-liquid slug flow with small bubbles in liquid plugs. *International Journal of Heat and Mass Transfer*, **42**(1):153–163, 1999.

[20] J. H. Ferziger and M. Perić. *Computational methods for fluid dynamics.* Springer Verlag, 3rd edition, 2002.

[21] M. Gad-el Hak. The fluid mechanics of microdevices - the freeman scholar lecture. *Journal of Fluids Engineering*, **121**:5–33, 1999.

[22] A. N. Gartsman, V. V. Cherkashin, and N. N. Rassadnikova. Diffusion flux through a spherical gas-liquid interface in the presence of a chemical reaction in the liquid phase. *International Chemical Engineering*, **19**(2):356–360, 1979.

[23] B.E. Ghidersa. *Finite volume-based Volume-of-Fluid method for the simulation of two-phase flows in small rectangular channels.* PhD thesis, Universität Karlsruhe, Forschungszentrum Karlsruhe, Wissenschaftliche Berichte, FZKA 6889, 2004.

[24] B.E. Ghidersa, M. Wörner, and D.G. Cacuci. Exploring the flow of immiscible fluids in a square vertical mini-channel by direct numerical simulation. *Chemical Engineering Journal*, **101**(1-3):285–294, 2004.

[25] W. G. Gray. A derivation of the equations for multi-phase transport. *Chemical Engineering Science*, **30**(2):229–233, 1975.

[26] G. Grötzbach. *Direkte numerische Simulation turbulenter Geschwindigkeits-,Druck- und Temperaturfelder bei Kanalströmungen*. PhD thesis, Universität Karlsruhe, KfK 2426, 1977.

[27] R. Gruber and T. Melin. Radial mass-transfer enhancement in bubble-train flow. *International Journal of Heat and Mass Transfer*, **46**(15):2799–2808, 2003.

[28] A. Günther, M. Jhunjhunwala, M. Thalmann, M. A. Schmidt, and K. F. Jensen. Micromixing of miscible liquids in segmented gas-liquid flow. *Langmuir*, 21(4):1547–1555, 2004.

[29] V. Hessel, S. Hardt, and H. Löwe. *Chemical Micro Process Engineering. Fundamentals, modelling and reactions*. Wiley-VCH Verlag GmbH & Co. KGaA, 2004.

[30] R. Higbie. The rate of absorption of pure gas into a still liquid during short periods of exposure. *Transm. Am. Inst. Chem. Eng.*, **365**:365–389, 1935.

[31] C. Hirsch. *Numerical computation of internal and external flows*. John Wiley & Sons, 1997.

[32] C. W. Hirt and B. D. Nichols. Volume of fluid (VOF) method for the dynamics of free boundaries. *Journal of Computational Physics*, **39**(1):201–225, 1981.

[33] C. Horvath, B. A. Solomon, and J. M. Engasser. Measurement of radial transport in slug flow using enzyme tubes. *Industrial and Engineering Chemistry Fundamentals*, **12**:431–439, 1973.

[34] H. Hotokezaka, M. Tokeshi, M. Harada, T. Kitamori, and Y. Ikeda. Development of the innovative nuclide separation system for high-level radioactive waste using microchannel chip - extraction behavior of metal ions from aqueous phase to organic phase in microchannel. *Progress in Nuclear Energy*, **47**(1-4):439–447, 2005.

[35] M. Ilić. *Statistical analysis of liquid phase turbulence based on direct numerical simulations of bubbly flows*. PhD thesis, Universität Karlsruhe, Forschungszentrum Karlsruhe, Wissenschaftliche Berichte, FZKA 7199, 2005.

[36] S. Irandoust and B. Andersson. Mass transfer and liquid-phase reactions in a segmented two-phase flow monolithic catalyst reactor. *Chemical Engineering Science*, **43**(4):1983–1988, 1988.

[37] S. Irandoust and B. Andersson. Simulation of flow and mass transfer in Taylor flow through a capillary. *Computers Chem. Engineering*, **13**(4-5):519–526, 1989.

[38] M. Ishii. *Thermo-fluid dynamic theory of two-phase flow*. Eyrolles, 1975.

[39] K. Jähnisch, M. Baerns, V. Hessel, W. Ehrfeld, V. Haverkamp, H. Löwe, Ch. Wille, and A. Guber. Direct fluorination of toluene using elemental fluorine in gas/liquid microreactors. *Journal of Fluorine Chemistry*, **105**:117–128, 2000.

[40] K. F. Jensen. Microreaction engineering - is small better? *Chemical Engineering Science*, **56**:293–303, 2001.

[41] G.-S. Jiang and C.-W. Shu. Efficient implementation of weighted ENO schemes. *Journal of Computational Physics*, **126**:202–228, 1996.

[42] G. Juncu. The influence of the Henry number on the conjugate mass transfer from a sphere; I. Physical mass transfer. *Heat and Mass Transfer*, **37**:519–530, 2001.

[43] G. Juncu. The influence of the Henry number on the conjugate mass transfer from a sphere; II. Mass transfer accompanied by a first-order chemical reaction. *Heat and Mass Transfer*, **38**:523–534, 2002.

[44] W. B. Kolb and R. L. Cerro. Coating the inside of a capillary of square cross section. *Chemical Engineering Science*, **46**(9):2181–2195, 1991.

[45] A. Koynov, J. G. Khinast, and G. Tryggvason. Mass transfer and chemical reactions in bubble swarms with dynamic interfaces. *A.I.Ch.E. Journal*, **51**(10):2786–2800, 2005.

[46] M. T. Kreutzer, P. Du, J. J. Heiszwolf, F. Kapteijn, and J. A. Moulijn. Mass transfer characteristics of three-phase monolith reactors. *Chemical Engineering Science*, **56**(21-22):6015–6023, 2001.

[47] R. Kronig and J. C. Brink. On the theory of extraction from falling droplets. *Appl. Science Research*, **A2**:142–154, 1950.

[48] D. Lakehal, M. Meier, and M. Fulgosi. Interface tracking towards the direct simulation of heat and mass transfer in multiphase flows. *International Journal of Heat and Fluid Flow*, **23**:242–257, 2002.

[49] V. G. Levich. *Physicochemical hydrodynamics*. Prentice-Hall, 1962.

[50] Z. Liu and C. Ma. A new method fr numerical treatment of diffusion coefficients at control-volume surfaces. *Numerical Heat Transfer B*, **47**(5):491–505, 2005.

[51] T. R. Marrero and E. A. Mason. Gaseous diffusion coefficients. *Journal of Physical and Chemical Reference Data*, **1**:3–118, 1972.

[52] K. Mühlfriedel and K. H. Baumann. Concentration measurements during mass transfer across liquid-phase boundaries using laser induced fluorescence (PLIF). *Experiments in Fluids*, **28**:279–281, 2000.

[53] T. Münsterer and B. Jähne. LIF measurements of concentration profiles in the aqueous mass boundary layer. *Experiments in Fluids*, **25**:190–196, 1998.

[54] J. A. Ochoa-Tapia, J. A. del Río, and S. Whitaker. Bulk and surface diffusion in porous media: an application of the surface-averaging theorem. *Chemical Engineering Science*, **48**(11):2061–2082, 1993.

[55] M. Ohta and M. Suzuki. Numerical analysis of mass transfer from a free motion drop in a solvent extraction process. *Solvent Extraction Research and Development*, **3**:138–149, 1996.

[56] S. Osher and J. A. Sethian. Fronts propagating with curvature-dependent speed: Algorithms based on Hamilton-Jacobi formulations. *Journal of Computational Physics*, **79**(1):12–49, 1988.

[57] A. R. Paschedag, W. H. Piarah, and M. Kraume. Treatment of limits for mass transfer at single droplets - validation of numerical results. *Chemical Engineering and Technology*, **25**(10):953–956, 2002.

[58] A. R. Paschedag, W. H. Piarah, and M. Kraume. Sensitivity study for the mass transfer at a single droplet. *International Journal of Heat and Mass Transfer*, **48**(16):3402–3410, 2005.

[59] S. V. Patankar. *Numerical heat transfer and fluid flow*. Taylor & Francis, 1980.

[60] R. H. Perry and D. Green. *Perry's chemical engineers' handbook*. McGraw-Hill, 6th edition, 1987.

[61] J. Petera and L. R. Weatherley. Modelling of mass transfer from falling droplets. *Chemical Engineering Science*, **56**(16):4929–4947, 2001.

[62] P. Pfeifer, A. Wenka, K. Schubert, M. A. Liauw, and G. Emig. Characterization of flow distribution in microchannel reactors. *A.I.Ch.E. Journal*, **50**(2):418–425, 2004.

[63] A. D. Polyanin. *Handbook of linear partial differential equations for engineers and scientists*. Chapman & Hall/CRC, 2002.

[64] F. Raymond and J.-M. Rosant. A numerical and experimental study of the terminal velocity and shape of bubbles in viscous liquids. *Chemical Engineering Science*, **55**(5):943–955, 2000.

[65] S. Roy and S. R. Duke. Laser induced fluorescence measurements of dissolved oxygen concentration fields near air bubble surfaces. *Review of scientific instruments*, **71**(9):3494–3501, 2000.

[66] S. Roy and S. R. Duke. Visualization of oxygen concentration fields and measurement of concentration gradients at bubble surfaces in surfactant-contaminated water. *Experiments in Fluids*, **36**(4):654–662, 2004.

[67] E. Ruckenstein. Mass transfer between a single drop and a continuous phase. *International Journal of Heat and Mass Transfer*, **10**:1785–1792, 1967.

[68] W. Sabisch. *Dreidimensionale numerische Simulation der Dynamik von aufsteigenden Einzelblasen und Blasenschwärmen mit einer Volume-of-Fluid-Methode.* PhD thesis, Universität Karlsruhe, Forschungszentrum Karlsruhe, Wissenschaftliche Berichte, FZKA 6478, 2000.

[69] R. Sander. Modeling atmospheric chemistry: interactions between gas-phase species and liquid cloud/aerosol particles. *Surveys in Geophysics*, **20**:1–31, 1999.

[70] R. Scardovelli and S. Zaleski. Direct numerical simulation of free-surface and interfacial flow. *Annu. Rev. Fluid Mech.*, **31**:567–603, 1999.

[71] R. W. Schrage. *A theoretical study of interphase mass transfer.* Columbia University Press, New York, 1953.

[72] K. Schubert, J. Brandner, M. Fichtner, G. Linder, U. Schygulla, and A. Wenka. Microstructure devices for applications in thermal and chemical process engineering. *Microscale Thermophysical Engineering*, **5**:17–39, 2001.

[73] U. Schumann. *Ein Verfahren zur direkten numerischen Simulation turbulenten Strmungen in Platten- und Ringspaltkanälen und über seine Anwendung zur Untersuchung von Turbulenzmodellen.* PhD thesis, Universität Karlsruhe, KfK 1854, 1973.

[74] J. A. Sethian. *Level set methods and fast marching methods. Evolving interfaces in computational geometry, fluid mechanics, computer vision, and materials science.* Cambridge University Press, 1999.

[75] T. K. Sherwood and R. L. Pigford. *Absorption and extraction.* McGraw Hill, 1952.

[76] T. K. Sherwood, R. L. Pigford, and C. R Wilke. *Mass transfer.* McGraw-Hill, 1975.

[77] C.-W. Shu and S. Osher. Efficient implementation of essentially non-oscilatory shock-capturing schemes. *Journal of Computational Physics*, **77**:439–471, 1988.

[78] C.-W. Shu and S. Osher. Efficient implementation of essentially non-oscilatory shock-capturing schemes II. *Journal of Computational Physics*, **83**:32–78, 1989.

[79] J. C. Slattery. *Interfacial transport phenomena.* Springer - Verlag, 1990.

[80] T.C. Thulasidas, M.A. Abraham, and R.L. Cerro. Bubble-train flow in capillaries of circular and square cross section. *Chemical Engineering Science*, **50**(2):183–199, 1995.

[81] H. L. Toor and J. M. Marchello. Film-penetration model for mass and heat transfer. *A.I.Ch.E.Journal*, **4**(1):97–101, 1958.

[82] P. Tortopidis and V. Bontozoglou. Mass transfer in gas-liquid flow in small-diameter tubes. *Chemical Engineering Science*, **52**:2231–2237, 1997.

[83] R. E. Treybal. *Liquid extraction*. McGraw-Hill Book Company, 2nd edition, 1963.

[84] R. E. Treybal. *Mass-transfer operations*. McGraw-Hill Book Company, 3rd edition, 1980.

[85] S. O. Unverdi and G. Tryggvasson. A front-tracking method for viscous, incompressible, multi-fluid flows. *Journal of Computational Physics*, **100**(1):25–37, 1992.

[86] A. R. Uribe-Ramírez and W. J. Korchinsky. Fundamental theory for prediction of single-component mass transfer in liquid drops at intermediate Reynolds numbers $(10 \leq Re \leq 250)$. *Chemical Engineering Science*, **55**(16):3305–3318, 2000.

[87] J.M. van Baten and R. Krishna. CFD simulations of mass transfer from Taylor bubbles rising in circular capillaries. *Chemical Engineering Science*, **59**(12):2535–2545, 2004.

[88] J.M. van Baten and R. Krishna. CFD simulations of wall mass transfer for Taylor flow in circular capillaries. *Chemical Engineering Science*, **60**(4):1117–1126, 2005.

[89] V.R. Voller. Numerical treatment of rapidly changing and discontinuous conductivities. *International Journal of Heat and Mass Transfer*, **44**(23):4553–4556, 2001.

[90] V.R. Voller and C.R. Swaminathan. Treatment of discontinuous thermal conductivity in control-volume solutions of phase-change problems. *Numerical Heat Transfer B*, **24**:161–180, 1993.

[91] J.R. Welty, W.E. Charles, and W.E. Robert. *Fundamentals of Momentum, Heat and Mass Transfer*. John Wiley & Sons, 3rd edition, 1984.

[92] S. Whitaker. A simple geometrical derivation of the spatial averaging theorem. *Chemical Engineering Education*, Winter 1985:18–21, 50–52.

[93] S. Whitaker. Diffusion and dispersion in porous media. *A.I.Ch.E. Journal*, **13**(3):420–427, 1967.

[94] S. Whitaker. Advances in theory of fluid motion in porous media. *Industrial Engineering and Chemistry*, **61**(12):14–28, 1969.

[95] S. Whitaker. On the functional dependence of the dispersion vector for scalar transport in porous media. *Chemical Engineering Science*, **26**:1893–1899, 1971.

[96] S. Whitaker. The transport equations for multi-phase systems. *Chemical Engineering Science*, **28**:139–147, 1973.

[97] S. Whitaker. *The method of volume averaging*. Kluwer Academic Publishers, 1999.

[98] W.G. Whitman. The two-film theory of gas absorption. *Chem. and Met. Eng.*, **29**(4):146–148, 1923.

[99] M. Wörner. The influence of gas-liquid density ratio on shape and rise velocity of an ellipsoidal bubble: a numerical study by 3D Volume-of-Fluid computations. In F.-P. Schindler, editor, *Proceedings of the First International Berlin Workshop on Transport Phenomena with Moving Boundaries, October 11-12, 2001, Berlin, Germany*, pages 67–84.

[100] M. Wörner. *Direkte Simulation turbulenter Rayleigh-Bénard Konvektion in flüssigem Natrium*. PhD thesis, Universität Karlsruhe, KfK 5228, 1994.

[101] M. Wörner. A compact introduction to the numerical modeling of multiphase flow. Technical Report Forschungszentrum Karlsruhe, Wissenschaftliche Berichte, FZKA 6932, http://bibliothek.fzk.de/zb/berichte/FZKA6932.pdf, 2003.

[102] M. Wörner, B. Ghidersa, and A. Onea. A model for the residence time distribution of bubble-train flow in a square mini-channel based on direct numerical simulation results. *International Journal of Heat and Fluid Flow*, 28(1):83–94, 2007.

[103] M. Wörner, B.E. Ghidersa, and A.F. Shahab. Numerical study of bubble train flow in a square vertical mini-channel: influence of length of the flow unit cell. In Y. Matsumoto, editor, *Fifth International Conference on Multiphase Flow, ICMF*, Yokohama, Japan, May 30 - June 4, 2004, CD-ROM Paper no. 154.

[104] M. Wörner, W. Sabisch, G. Grötzbach, and D.G. Cacuci. Volume-averaged conservation equations for volume-of-fluid interface tracking. In *Fourth International Conference on Multiphase Flow, ICMF*, pages 67–84, New-Orleans, Louisiana, U.S.A., May 27 - June 1, 2001.

[105] C. Yang and Z.-S. Mao. Numerical simulation of interphase mass transfer with the level set approach. *Chemical Engineering Science*, **60**(10):2643–2660, 2005.

APPENDIX

Appendix A

Analysis of the volume averaged convective term

Three definitions [95] of the average of parameter ψ have been employed throughout this study:

spatial average

$$\overline{\psi}^V \equiv \frac{1}{V} \int_V \psi \mathrm{d}V \tag{A.1}$$

phase (superficial) average

$$\overline{\psi_k}^V \equiv \frac{1}{V} \int_{V_k(t)} \psi_k \mathrm{d}V \tag{A.2}$$

intrinsic phase average

$$\overline{\psi_k}^k \equiv \frac{1}{V_k(t)} \int_{V_k(t)} \psi_k \mathrm{d}V \tag{A.3}$$

For a constant concentration, one can observe from equation (A.2) that the phase average does not equal that constant value. Therefore, for the analysis of mass transfer with chemical reactions it is more convenient to work with the intrinsic phase average [92]. Since these values are also not known, relative terms will be further introduced.

In order to analyze the volume averaged convective term $\nabla \cdot \overline{X_k c_k^\alpha \mathbf{v}_k}^V$, the deviations from the mean values for concentration of species α and phase velocity are considered [25, 96]:

$$
\begin{aligned}
c_k^{\alpha\prime} &\equiv c_k^\alpha - \overline{c_k^\alpha}^k \\
\mathbf{v}_k' &\equiv \mathbf{v}_k - \overline{\mathbf{v}_k}^k
\end{aligned}
\tag{A.4}
$$

These terms, designated as sub-grid scale terms, depend on the quality of the grid used in computation. They describes processes having a characteristic length smaller than the smallest mesh cell employed. Proper sub-grid scale models have to be considered when the mesh used is not sufficiently refined. Since the present study is based on the direct numerical simulation of two phase flows, we assume that the magnitude of the sub-grid

scale terms is smaller than the error of the numerical scheme. Therefore, no sub-grid scale model is considered.

Although Whitaker [93] considers the velocity deviation relative to the volume average velocity $\overline{\mathbf{v}_k}^V$, defining the deviation relative to the phase average $\overline{\mathbf{v}_k}^k$ is more appropriate for two-phase problems. This issue proves to be meaningful and numerically more accurate. Figure A.1 illustrates the volume average parameters, $\bar{p}_1^V$ and $\bar{p}_2^V$, and the phase average parameters $\bar{p}_1^1$ and $\bar{p}_2^2$.
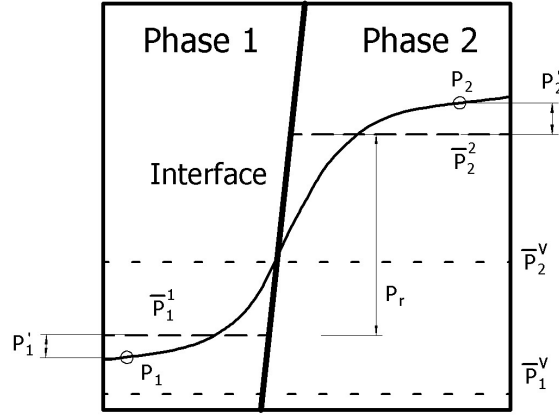
Figure A.1: Parameters averaged over phase and over volume (case of unresolved boundary layer, i.e. $\mathrm{P}_r \neq 0$)

A relative velocity is introduced to relate the velocities of phases at interface:

$$\mathbf{v}_r = \overline{\mathbf{v}_2}^2 - \overline{\mathbf{v}_1}^1 \tag{A.5}$$

Using relations (A.4) the averaged convective term in equation (3.20) becomes:

$$
\begin{aligned}
\overline{X_k c_k^\alpha \mathbf{v}_k}^V &= \overline{X_k (\overline{c_k^\alpha}^k + c_k^{\alpha\prime})(\overline{\mathbf{v}_k}^k + \mathbf{v}_k^\prime)}^V \\
&= \overline{X_k \overline{c_k^\alpha}^k \overline{\mathbf{v}_k}^k - X_k \overline{c_k^\alpha}^k \mathbf{v}_k + X_k \overline{c_k^\alpha}^k \mathbf{v}_k + X_k c_k^{\alpha\prime} \overline{\mathbf{v}_k}^k + X_k \overline{c_k^\alpha}^k \mathbf{v}_k^\prime + X_k c_k^{\alpha\prime} \mathbf{v}_k^\prime}^V \tag{A.6} \\
&= \overline{X_k \overline{c_k^\alpha}^k \mathbf{v}_k}^V + \mathbf{T}_k^{\mathrm{sgs}},
\end{aligned}
$$

Due to the presence of the phase indicator function, the term $\overline{X_k \overline{c_k^\alpha}^k \mathbf{v}_k}^V$ represents the averaged value over all phases and therefore a spatial average can be applied. Eliminating $\overline{X_k}^V$ from the integral allows further for a phase average. Accordingly, the first term in the r.h.s. of equation (A.6) can be further developed as:

$$\overline{X_k \overline{c_k^\alpha}^k \mathbf{v}_k}^V = \frac{1}{V} \int_V X_k \overline{c_k^\alpha}^k \mathbf{v}_k \mathrm{d}V = \frac{V_k}{V} \frac{\overline{c_k^\alpha}^k}{V_k} \int_{V_k} \mathbf{v}_k \mathrm{d}V = \alpha_k \overline{c_k^\alpha}^k \overline{\mathbf{v}_k}^k \tag{A.7}$$

while the sub-grid scale term $\mathbf{T}^{\text{sgs}}$ is expressed as:

$$\mathbf{T}_k^{\text{sgs}} = \overline{X_k \overline{c_k^{\alpha}}^k \overline{\mathbf{v}_k}^k}^V - \overline{X_k \overline{c_k^{\alpha}}^k \mathbf{v}_k}^V + \overline{X_k c_k^{\alpha\,\prime} \overline{\mathbf{v}_k}^k}^V + \overline{X_k \overline{c_k^{\alpha}}^k \mathbf{v}_k'}^V + \overline{X_k c_k^{\alpha\,\prime} \mathbf{v}_k'}^V, \tag{A.8}$$

where:

$$\overline{X_k \overline{c_k^{\alpha}}^k \overline{\mathbf{v}_k}^k}^V = \frac{1}{V} \int_V X_k \overline{c_k^{\alpha}}^k \overline{\mathbf{v}_k}^k \mathrm{d}V = \frac{V_k}{V} \frac{1}{V_k} \int_{V_k} \overline{c_k^{\alpha}}^k \overline{\mathbf{v}_k}^k \mathrm{d}V = \alpha_k \overline{\overline{c_k^{\alpha}}^k \overline{\mathbf{v}_k}^k}^k \tag{A.9}$$

Similar one can write:

$$\begin{aligned}
\overline{X_k \overline{c_k^{\alpha}}^k \mathbf{v}_k}^V &= \alpha_k \overline{\overline{c_k^{\alpha}}^k \mathbf{v}_k}^k = \alpha_k \overline{c_k^{\alpha}}^k \overline{\mathbf{v}_k}^k & \overline{X_k c_k^{\alpha\,\prime} \overline{\mathbf{v}_k}^k}^V &= \alpha_k \overline{c_k^{\alpha\,\prime} \overline{\mathbf{v}_k}^k}^k \\
\overline{X_k c_k^{\alpha\,\prime} \mathbf{v}_k'}^V &= \alpha_k \overline{c_k^{\alpha\,\prime} \mathbf{v}_k'}^k & \overline{X_k \overline{c_k^{\alpha}}^k \mathbf{v}_k'}^V &= \alpha_k \overline{\overline{c_k^{\alpha}}^k \mathbf{v}_k'}^k
\end{aligned} \tag{A.10}$$

Using relations (A.9) and (A.10) the sub-grid scale term (A.8) can be further written as:

$$\mathbf{T}_k^{\text{sgs}} = \underbrace{\alpha_k \left(\overline{\overline{c_k^{\alpha}}^k \overline{\mathbf{v}_k}^k}^k - \overline{c_k^{\alpha}}^k \overline{\mathbf{v}_k}^k \right)}_{\mathbf{L}_k^c} + \underbrace{\alpha_k \left(\overline{c_k^{\alpha\,\prime} \overline{\mathbf{v}_k}^k}^k + \overline{\overline{c_k^{\alpha}}^k \mathbf{v}_k'}^k \right)}_{\mathbf{C}_k^c} + \underbrace{\alpha_k \overline{c_k^{\alpha\,\prime} \mathbf{v}_k'}^k}_{\mathbf{R}_k^c} \tag{A.11}$$

In analogy with the analysis of the volume averaged momentum equation for individual phases [101], the vectors $\mathbf{L}_k^c$, $\mathbf{C}_k^c$ and $\mathbf{R}_k^c$ are designated as Leonard-like term, cross-like term and respectively sub-grid scale Reynolds-like stress term. Whitaker [93] refers to the sub-grid scale Reynolds-like stress term as the dispersion vector. The appearance of these terms is due to the non-linear behaviour of the convective term.

The averages applied is well behaved [94], i.e. applying the volume averaging for equations (A.4) one obtains:

$$\begin{aligned}
\overline{c_k^{\alpha}}^k &\equiv \overline{\overline{c_k^{\alpha}}^k}^k + \overline{c_k^{\alpha\,\prime}}^k &= \overline{c_k^{\alpha}}^k + \overline{c_k^{\alpha\,\prime}}^k \\
\overline{\mathbf{v}_k}^k &\equiv \overline{\overline{\mathbf{v}_k}^k}^k + \overline{\mathbf{v}_k'}^k &= \overline{\mathbf{v}_k}^k - \overline{\mathbf{v}_k'}^k
\end{aligned} \tag{A.12}$$

and therefore:

$$\overline{c^{\alpha\,\prime}}^k = \overline{\mathbf{v}'}^k = 0 \tag{A.13}$$

Accordingly, relation (A.8) simplifies to:

$$\mathbf{T}_k^{\text{sgs}} = \alpha_k \left(\overline{\overline{c_k^{\alpha}}^k \overline{\mathbf{v}_k}^k}^k - \overline{c_k^{\alpha}}^k \overline{\mathbf{v}_k}^k \right) + \alpha_k \overline{c_k^{\alpha\,\prime} \mathbf{v}_k'}^k = \alpha_k \overline{c_k^{\alpha\,\prime} \mathbf{v}_k'}^k \tag{A.14}$$

Whitaker [95] represents the dispersion vector by means of diffusion model. This model uses the truncated Taylor series expansion of the velocity and of the spatial derivative of the concentration. It is reported that the dispersion coefficient, which is a parameter

similar to the mass diffusivity, is a function of time and strongly dependent on the concentration gradient. Still, unsatisfactorily results are obtained in case of dispersion at short times or high concentration gradient.

In `TURBIT-VoF` the dispersion vector will be assumed null.

Summing up the convective term for case of two-phase will result in:

$$\sum_{k=1}^{2} \nabla \cdot \overline{X_k c_k^\alpha \mathbf{v}_k}^V = \nabla \cdot (\alpha_1 \overline{c_1^\alpha}^1 \overline{\mathbf{v}_1}^1 + \alpha_2 \overline{c_2^\alpha}^2 \overline{\mathbf{v}_2}^2) + \nabla \cdot \underbrace{(\alpha_1 \mathbf{T}_1^{\mathrm{sgs}} + \alpha_2 \mathbf{T}_2^{\mathrm{sgs}})}_{\mathbf{T}_{\mathrm{m}}^{\mathrm{sgs}}}, \qquad (A.15)$$

where $\mathbf{T}_{\mathrm{m}}^{\mathrm{sgs}}$ designates the two-phase mixture sub-grid scale term. Further, one can consider the expression of the convective term using the center-of-mass velocity, relative velocity and mixture density:

$$
\begin{aligned}
\nabla \cdot \alpha_1 \overline{c_1^\alpha}^1 \overline{\mathbf{v}_1}^1 &= \nabla \cdot \frac{\alpha_1 \overline{c_1^\alpha}^1 \overline{\mathbf{v}_1}^1 (\alpha_1 \overline{\rho_1}^1 + \alpha_2 \overline{\rho_2}^2)}{\rho_{\mathrm{m}}} \\
&= \nabla \cdot \frac{\alpha_1 \overline{c_1^\alpha}^1 \alpha_1 \overline{\rho_1}^1 \overline{\mathbf{v}_1}^1 + \alpha_1 \overline{c_1^\alpha}^1 \alpha_2 \overline{\rho_2}^2 \overline{\mathbf{v}_1}^1 + \alpha_1 \overline{c_1^\alpha}^1 \alpha_2 \overline{\rho_2}^2 \overline{\mathbf{v}_2}^2 - \alpha_1 \overline{c_1^\alpha}^1 \alpha_2 \overline{\rho_2}^2 \overline{\mathbf{v}_2}^2}{\rho_{\mathrm{m}}} \\
&= \nabla \cdot \left[\frac{\alpha_1 \overline{c_1^\alpha}^1 (\alpha_1 \overline{\rho_1}^1 \overline{\mathbf{v}_1}^1 + \alpha_2 \overline{\rho_2}^2 \overline{\mathbf{v}_2}^2)}{\rho_{\mathrm{m}}} + \frac{\alpha_1 \overline{c_1^\alpha}^1 \alpha_2 \overline{\rho_2}^2 (\overline{\mathbf{v}_1}^1 - \overline{\mathbf{v}_2}^2)}{\rho_{\mathrm{m}}} \right] \\
&= \nabla \cdot \left(\alpha_1 \overline{c_1^\alpha}^1 \mathbf{v}_{\mathrm{m}} - \frac{\alpha_1 \overline{c_1^\alpha}^1 \alpha_2 \overline{\rho_2}^2}{\rho_{\mathrm{m}}} \mathbf{v}_r \right)
\end{aligned}
$$

$$(A.16)$$

Similar, one can write:

$$\nabla \cdot \alpha_2 \overline{c_2^\alpha}^2 \overline{\mathbf{v}_2}^2 = \nabla \cdot \left(\alpha_2 \overline{c_2^\alpha}^2 \mathbf{v}_{\mathrm{m}} + \frac{\alpha_1 \overline{\rho_1}^1 \alpha_2 \overline{c_2^\alpha}^2}{\rho_{\mathrm{m}}} \mathbf{v}_r \right) \qquad (A.17)$$

and therefore relation (A.15) becomes:

$$
\begin{aligned}
\sum_{k=1}^{2} \nabla \cdot \overline{X_k c_k^\alpha \mathbf{v}_k}^V &= \nabla \cdot (\alpha_1 \overline{c_1^\alpha}^1 + \alpha_2 \overline{c_2^\alpha}^2) \mathbf{v}_{\mathrm{m}} + \nabla \cdot \alpha_1 \alpha_2 \frac{\overline{\rho_1}^1 \overline{c_2^\alpha}^2 - \overline{\rho_2}^2 \overline{c_1^\alpha}^1}{\rho_{\mathrm{m}}} \mathbf{v}_r + \nabla \cdot \mathbf{T}_{\mathrm{m}}^{\mathrm{sgs}} \\
&= \nabla \cdot c_{\mathrm{m}}^\alpha \mathbf{v}_{\mathrm{m}} + \nabla \cdot \underbrace{\alpha_1 \alpha_2 \frac{\overline{\rho_1}^1 \overline{c_2^\alpha}^2 - \overline{\rho_2}^2 \overline{c_1^\alpha}^1}{\rho_{\mathrm{m}}} \mathbf{v}_r}_{\mathbf{D}_{\mathrm{int}}^c} + \nabla \cdot \mathbf{T}_{\mathrm{m}}^{\mathrm{sgs}}
\end{aligned}
$$

$$(A.18)$$

The term $\mathbf{D}_{\mathrm{int}}^c$ resembles with the drift-flux tensor term from the momentum equation [101]. It expresses the difference between the resolved convective flux (calculated with very fine mesh size) and the averaged convective flux due to non-zero relative velocity between phases. Since this study is concerned with direct numerical simulation, it is assumed that the cell mesh size is very small and therefore the homogeneous model is employed to relate

the phase velocities at interface (i.e. $\mathbf{v}_r = 0$). As a consequence, the drift-like term $\mathbf{D}_{\text{int}}^c$ is annulled and relation (A.15) becomes:

$$\sum_{k=1}^{2} \nabla \cdot \overline{X_k c_k^\alpha \mathbf{v}_k}^V = \nabla \cdot c_{\text{m}}^\alpha \mathbf{v}_{\text{m}} + \nabla \cdot \mathbf{T}_{\text{m}}^{\text{sgs}} \tag{A.19}$$

Since the sub-grid scale terms are neglected, i.e.:

$$\mathbf{T}_1^{\text{sgs}} = \mathbf{T}_2^{\text{sgs}} = \mathbf{T}_{\text{m}}^{\text{sgs}} = 0 \tag{A.20}$$

the volume averaged convective term in equation (3.24) becomes:

$$\sum_{k=1}^{2} \nabla \cdot \overline{X_k c_k^\alpha \mathbf{v}_k}^V = \nabla \cdot c_{\text{m}}^\alpha \mathbf{v}_{\text{m}} \tag{A.21}$$

Appendix B

Analysis of the volume averaged interfacial transport term

The interfacial transport term in equation (3.20) is designated by the area integral:

$$\overline{\mathbf{j}_{ki}^\alpha \cdot \nabla X_k}^V = \frac{1}{V} \int_{S_i} \mathbf{j}_{ki}^\alpha \cdot \mathbf{n}_k \, \mathrm{d}S, \tag{B.1}$$

where $\mathbf{j}_{ki}^\alpha$ is the interfacial flux.

The integral form is further developed by Whitaker [96] as:

$$\frac{1}{V} \int_{S_i} \mathbf{j}_{ki}^\alpha \cdot \mathbf{n}_k \, \mathrm{d}S \equiv \frac{S_i(t)}{V} \alpha_k K \left(\overline{c_k^\alpha}^k - \overline{c_{k,\mathrm{eq}}^\alpha}^k \right), \tag{B.2}$$

where K is an overall mass transfer coefficient and the driving force considered is the difference between intrinsic phase average concentration $\overline{c_k^\alpha}^k$ and the intrinsic phase average concentration $\overline{c_{k,\mathrm{eq}}^\alpha}^k$ which will be in equilibrium with the intrinsic phase average concentration in the other phase (i.e. $\overline{c_{1,\mathrm{eq}}^\alpha}^1 = f(\overline{c_2^\alpha}^2)$). The r.h.s of equation (B.2) is referred to as diffusive interphase transport term [96].

Considering the interfacial boundary condition (3.11) for the case where no heterogeneous chemical reaction occurs at interface one can evaluate the sum of the volume averaged interfacial transport term as:

$$\int_{S_i} \mathbf{j}_{1i}^\alpha \cdot \mathbf{n}_1 \mathrm{d}S = -\frac{1}{H^\alpha} \int_{S_i} \mathbf{j}_{2i}^\alpha \cdot \mathbf{n}_2 \mathrm{d}S \implies$$

$$\int_{S_i} \mathbf{j}_{1i}^\alpha \cdot \mathbf{n}_1 \mathrm{d}S + \int_{S_i} \mathbf{j}_{2i}^\alpha \cdot \mathbf{n}_2 \mathrm{d}S = -\frac{1}{H^\alpha} \int_{S_i} \mathbf{j}_{2i}^\alpha \cdot \mathbf{n}_2 \mathrm{d}S + \int_{S_i} \mathbf{j}_{2i}^\alpha \cdot \mathbf{n}_2 \mathrm{d}S \implies \tag{B.3}$$

$$\int_{S_i} \mathbf{j}_{1i}^\alpha \cdot \mathbf{n}_1 \mathrm{d}S + \int_{S_i} \mathbf{j}_{2i}^\alpha \cdot \mathbf{n}_2 \mathrm{d}S = \left(1 - \frac{1}{H^\alpha} \right) \int_{S_i} \mathbf{j}_{2i}^\alpha \cdot \mathbf{n}_2 \mathrm{d}S$$

and therefore the sum of the volume averaged interfacial transport term in equation (3.20)

is:

$$\sum_{k=1}^{2} \frac{1}{V} \int_{S_i} \mathbf{j}_{ki}^{\alpha} \cdot \mathbf{n}_k \mathrm{d}S = \frac{H^{\alpha} - 1}{H^{\alpha}} \frac{1}{V} \int_{S_i} \mathbf{j}_{2i}^{\alpha} \cdot \mathbf{n}_2 \mathrm{d}S \qquad (B.4)$$

Using the continuous interfacial concentration approach, as definition (3.10) implies, leads to the appearance of an interfacial diffusive flux term that has to be evaluated on the gas side of the interface.

One can notice that for the particulate case where $H^{\alpha} = 1$, e.g. equal interfacial concentrations, the sum of the interfacial transport term will be null.

Appendix C

Influence of number of nodes on one-dimensional analytical solution

This appendix investigates the influence of the number of nodes used to evaluate the one-dimensional analytical concentration profile proposed by Crank [10] on the accuracy of interfacial concentration jump representation. The analytical solution is used to validate the one-dimensional diffusion term (see section 4.1.1).

The analytical test has the following relevant parameters: $D_1^\star = D_2^\star = 1\mathrm{m}^2/\mathrm{s}, H = 5$ (see Fig. D.3 b). The interface is placed in the center of the cell, as displayed in Figure 4.2 b. In Table C.1 are presented the interfacial concentrations at time step 500 and in table C.2 at time step 1000. The fourth column in tables C.1 and C.2 represents the concentration on the liquid side of the interface, while the fifth column represents the gas concentration. The last column represents the analytical calculated value of Henry's constant.

As expected, increasing the number of nodes used to evaluate the analytical solution increases the accuracy of the interfacial concentrations evaluation. Comparing the liquid and gas side concentrations shown in tables C.1 and C.2, it can be also concluded that, as diffusion proceeds in time, the interfacial concentrations determined analytically remain constant, as predicted by equations (4.2). This is a consequence of the assumption of instantaneous established equilibrium at interface.

Solution	Test	Nr. nodes	$\mathbf{c}_L$	$\mathbf{c}_G$	$H = \mathbf{c}_L/\mathbf{c}_G$
	1	500	0.77394	0.16667	4.64355
	2	1 000	0.81847	0.18153	4.50873
	3	5 000	0.83036	0.16964	4.89484
	4	10 000	0.83185	0.16815	4.94707
Analytical	5	30 000	0.83284	0.16716	4.98229
	6	60 000	0.83309	0.16691	4.99125
	7	90 000	0.83317	0.16683	4.99413
	8	150 000	0.83323	0.16677	4.99629
Numerical	-	100	0.95742	0.26596	3.59987

Table C.1: Interfacial concentrations (time step 500)

Solution	Test	Nr. nodes	$\mathbf{c}_L$	$\mathbf{c}_G$	$H = \mathbf{c}_L/\mathbf{c}_G$
	1	500	0.79131	0.16667	4.74777
	2	1 000	0.82282	0.17718	4.64398
	3	5 000	0.83123	0.16877	4.92522
	4	10 000	0.83228	0.16772	4.96231
Analytical	5	30 000	0.83298	0.16702	4.98731
	6	60 000	0.83316	0.16684	4.99377
	7	90 000	0.83322	0.16678	4.99592
	8	150 000	0.83326	0.16674	4.99736
Numerical	-	100	0.94731	0.23684	3.99979

Table C.2: Interfacial concentrations (time step 1000)

Appendix D

Numerical and analytical solutions for 1D and 2D diffusion tests

(a)   (b)
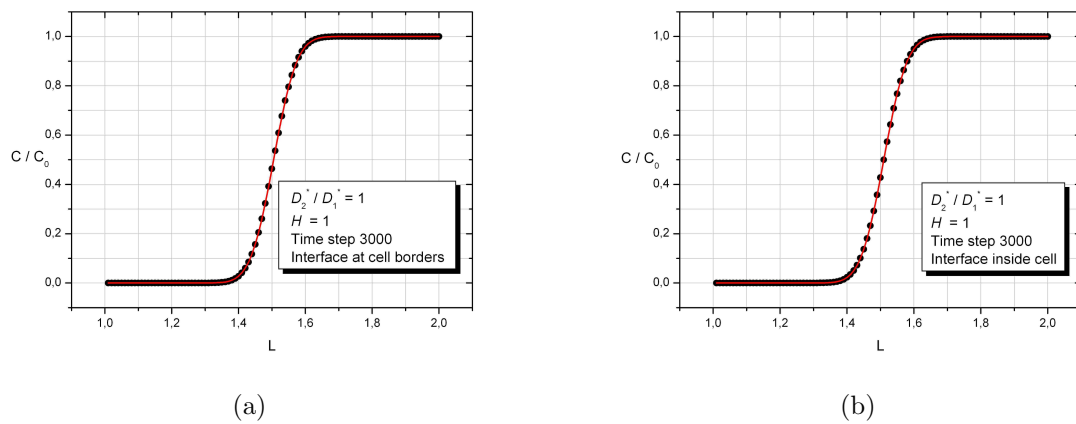
Figure D.1: **Case 1** - Numerical and analytical concentration profiles at time step 3000 - interface at cell borders (a) and interface inside cell (b)

(a)   (b)
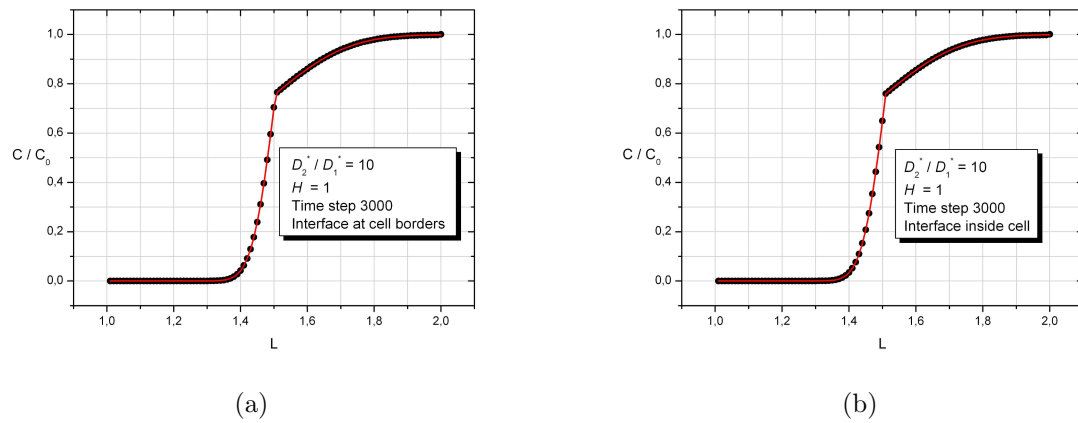
Figure D.2: **Case 2** - Numerical and analytical concentration profiles at time step 3000 - interface at cell borders (a) and interface inside cell (b)

(a)   (b)
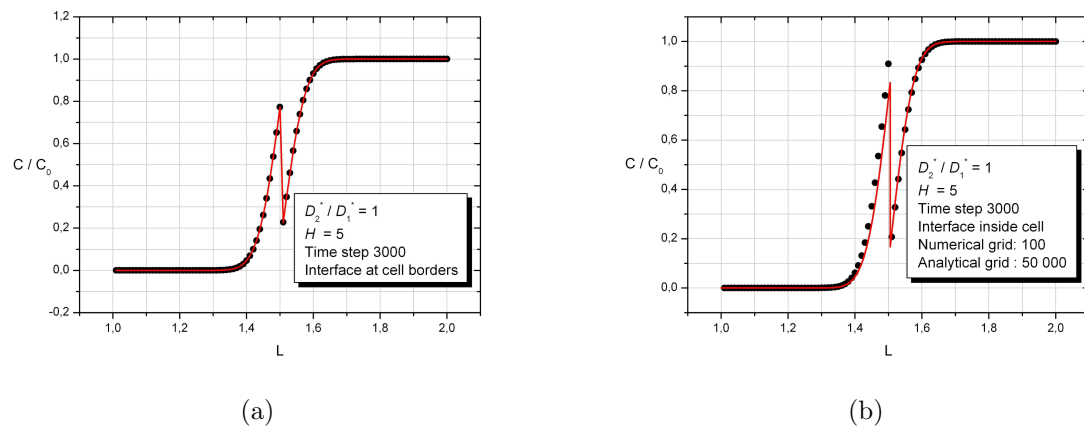
Figure D.3: **Case 3** - Numerical and analytical concentration profiles at time step 3000 - interface at cell borders (a) and interface inside cell (b)
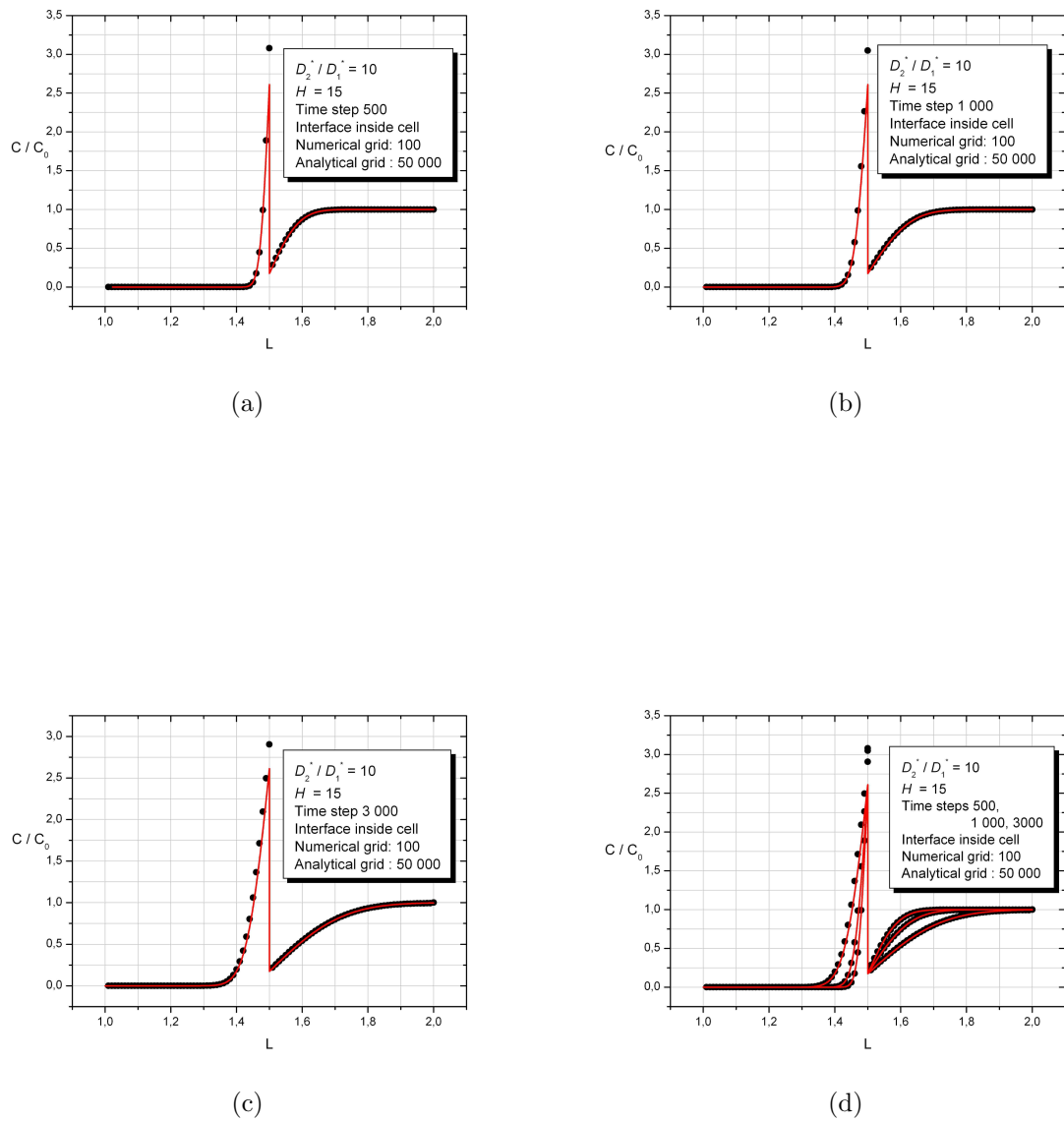
Figure D.4: **Case 4** - Numerical and analytical concentration profiles at time step 500 (a), 1000 (b) and 3000 (c) - case of interface inside cell. (d) Profiles displayed simultaneously

(a)

(b)

(c)

(d)
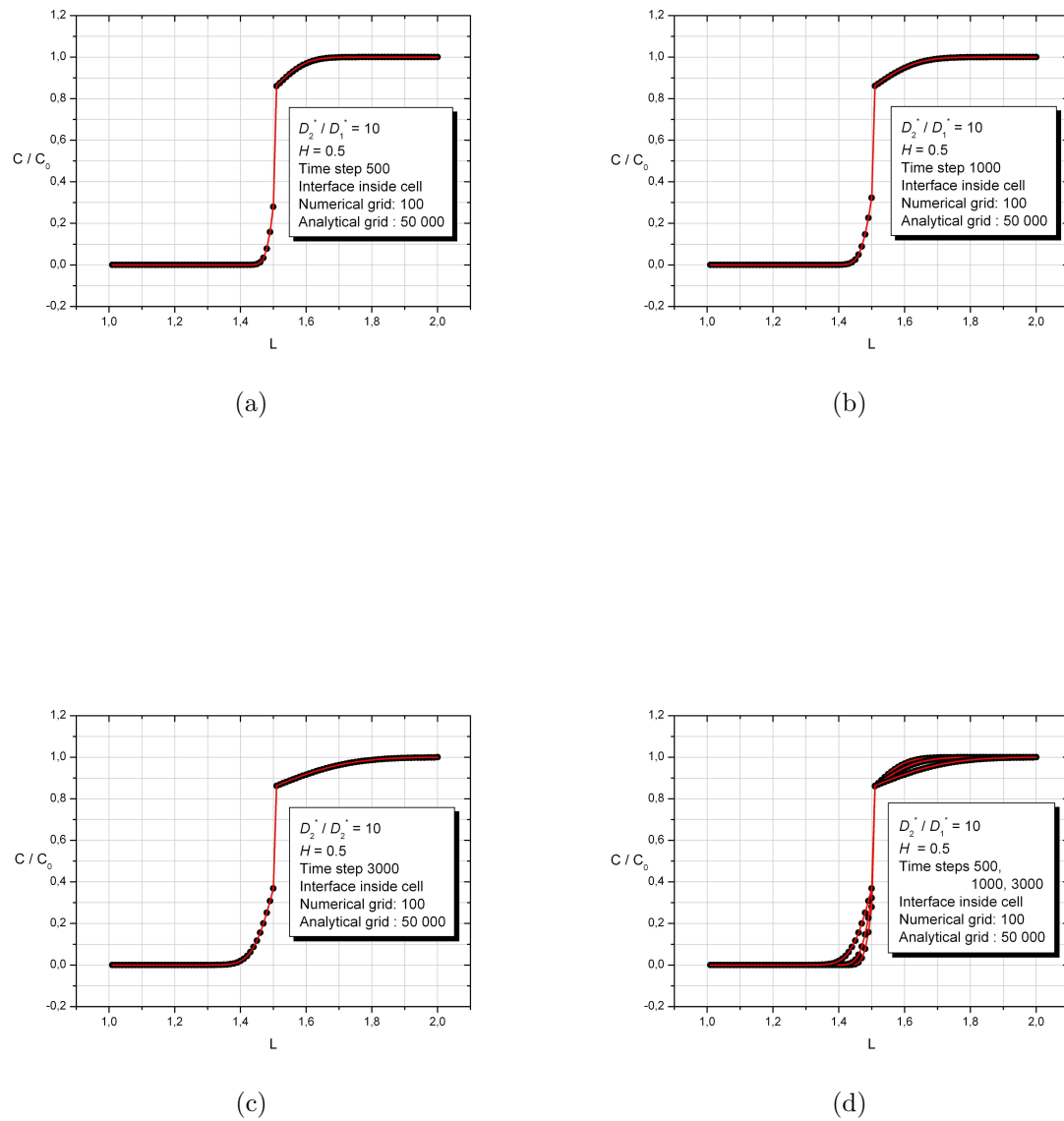
Figure D.5: **Case 5** - Numerical and analytical concentration profiles at time step 500 (a), 1000 (b) and 3000 (c) - case of interface inside cell. (d) Profiles displayed simultaneously
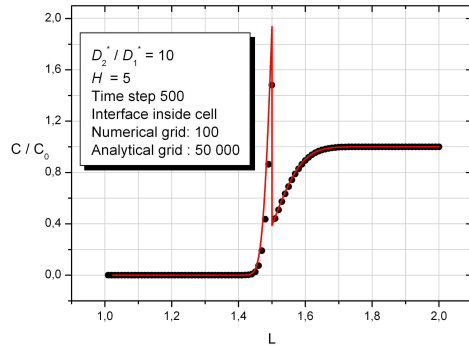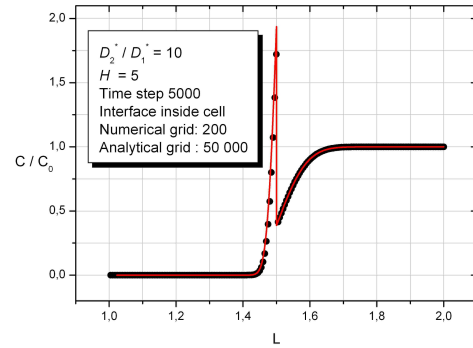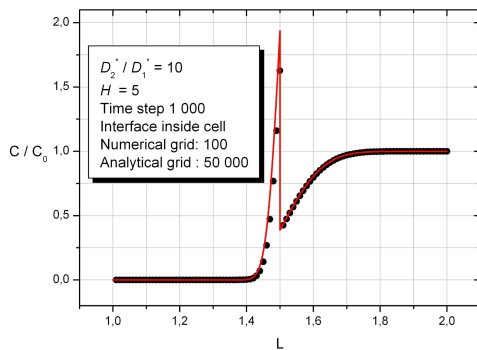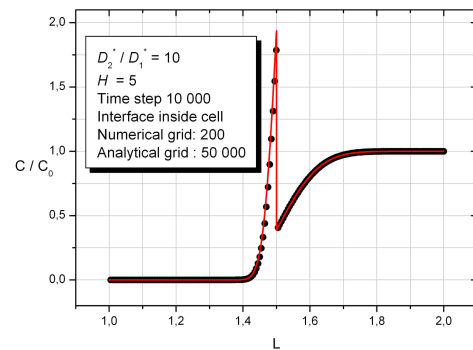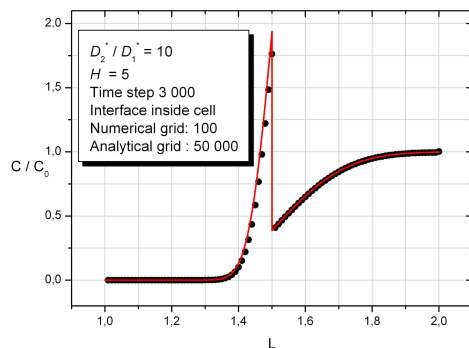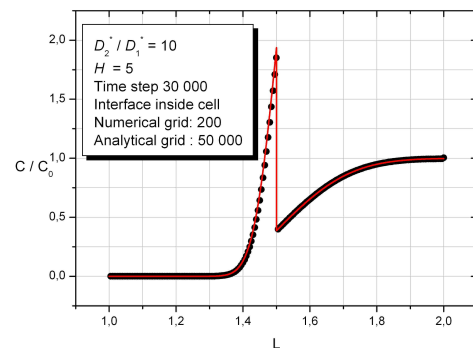
Figure D.6: **Case 6** - Numerical and analytical concentration profiles for coarse grid (a, c, e) and refined grid (b, d, f)

(a)

(b)

(c)

(d)
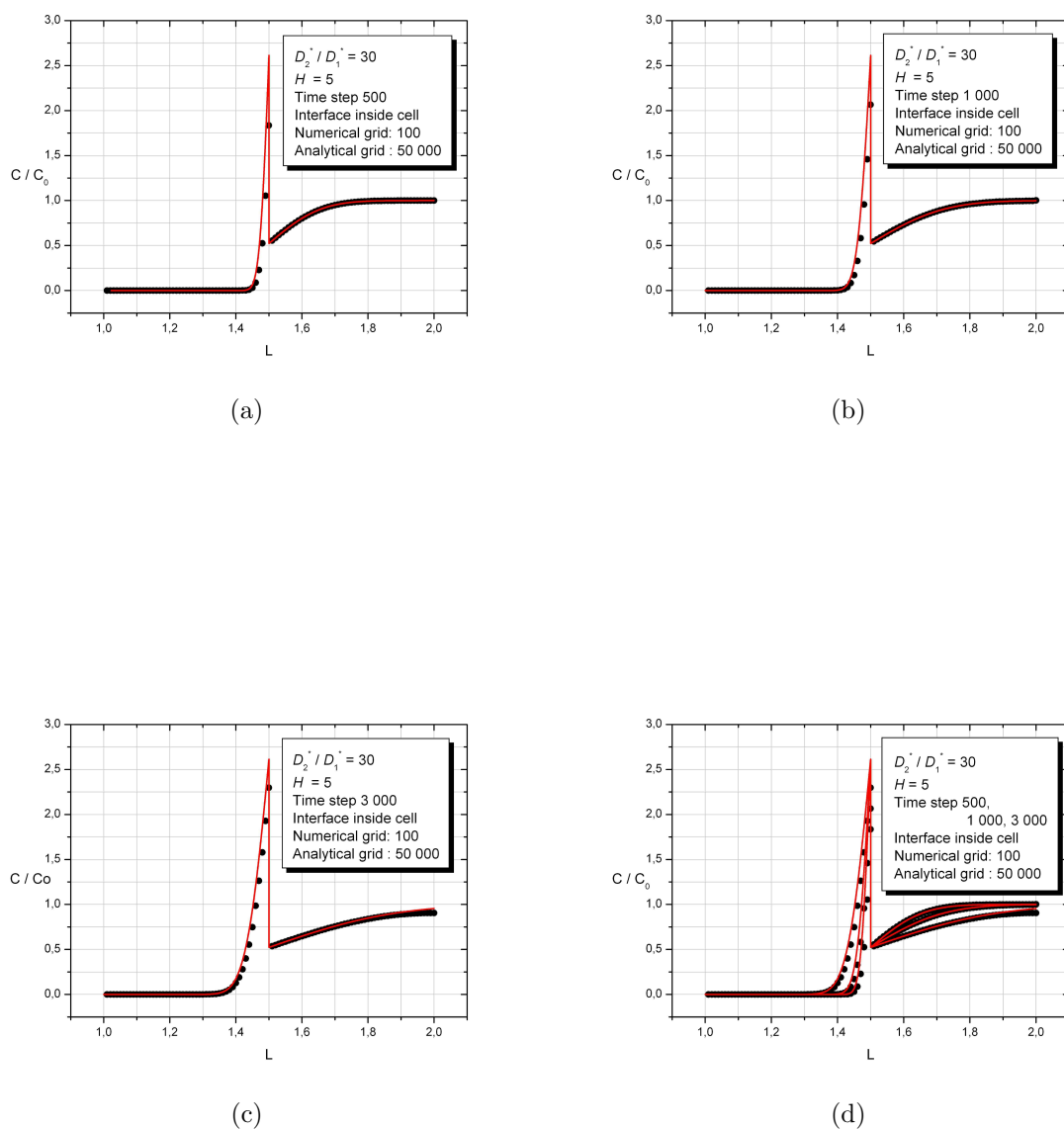
Figure D.7: **Case 7** - Numerical and analytical concentration profiles at time step 500 (a), 1000 (b) and 3000 (c) - case of interface inside cell. (d) Profiles displayed simultaneously
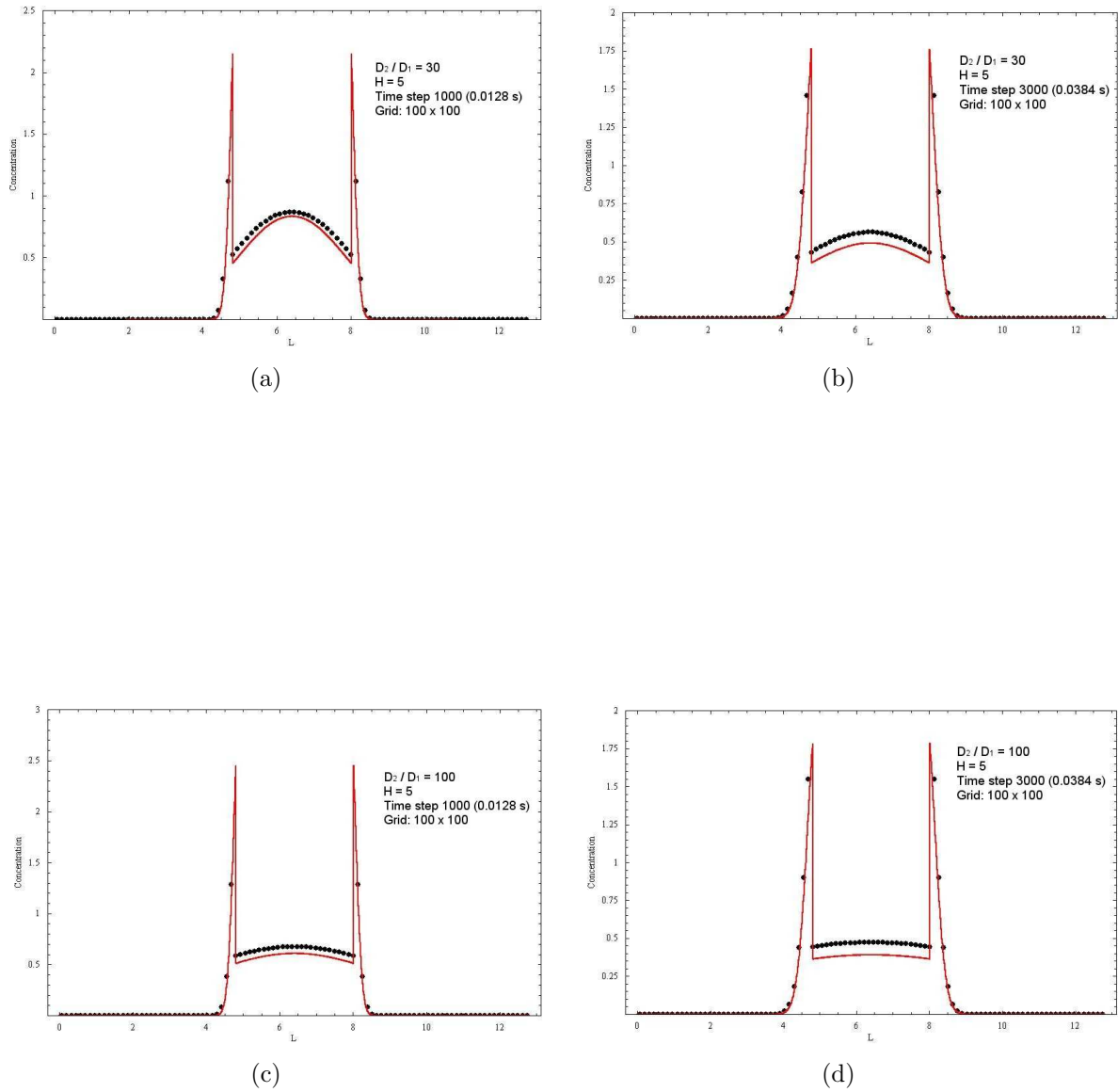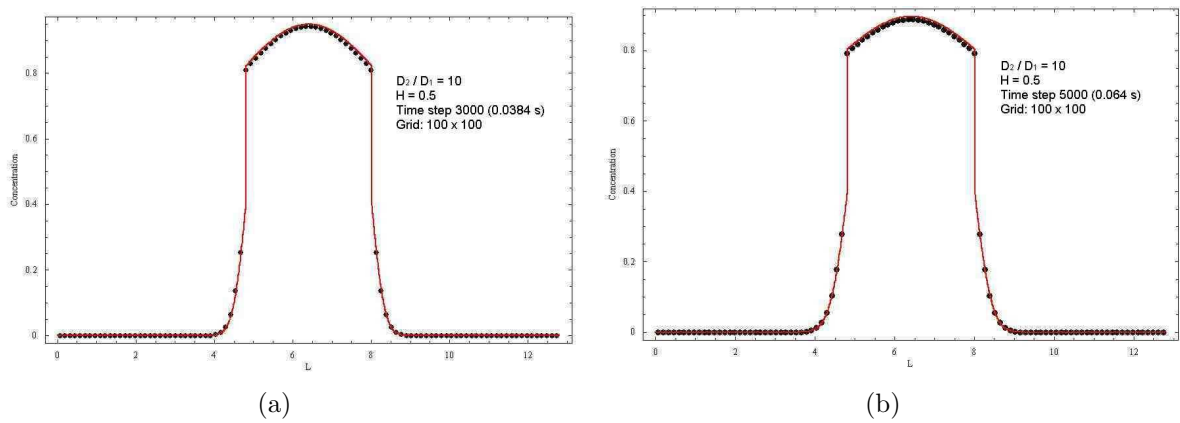
Figure D.8: Numerical and analytical concentration profiles at time step 3000 and 5000 for system $H = 5$, $D_2^\star/D_1^\star = 30$ m^2/s (a, b) and $D_2^\star/D_1^\star = 100$ m^2/s (c, d)
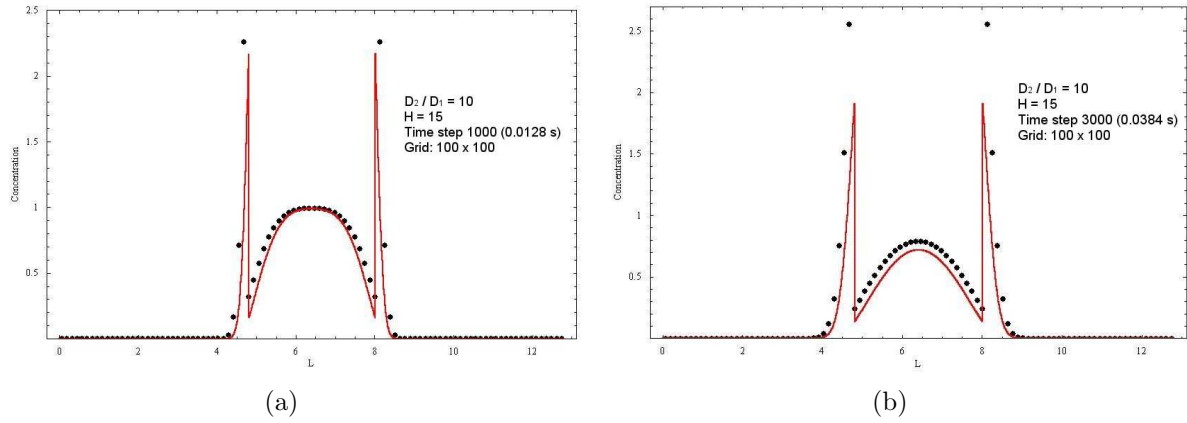
Figure D.9: Numerical and analytical concentration profiles at time step 1000 (a) and 3000 (b) for system $H = 15$, $D_2^\star/D_1^\star = 10$ m^2/s

Figure D.10: Comparison between numerical and analytical concentration profiles at time step 3000 (a) and 5000 (b) for system $H = 0.5$, $D_2^\star/D_1^\star = 10$ m^2/s

Appendix E

Derivation of the mass transfer coefficient

The mass balance at the interface is [88, 105]:

$$\frac{dc_L^{\alpha \star}}{dt^\star} = k_L^{\alpha \star} \frac{A^\star}{V^\star} \Delta c^{\alpha \star} \tag{E.1}$$

As discussed in section 4.2, several approaches exist for expressing the concentration gradient $\Delta c^{\alpha \star}$. In this study, the concentration gradient has been considered based on averaged concentrations (4.11). Therefore, the above relation can be rewritten as:

$$\frac{dc_L^{\alpha\,\mathrm{av}\,\star}}{dt^\star} = k_L^{\alpha \star} \frac{A^\star}{V^\star} \left(\frac{c_G^{\alpha\,\mathrm{av}\,\star}}{H^\alpha} - c_L^{\alpha\,\mathrm{av}\,\star} \right) \tag{E.2}$$

The difficulty in deriving this relation is the treatment of the concentration "driving force" $\Delta c^{\alpha \star} = c_G^{\alpha\,\mathrm{av}\,\star}/H^\alpha - c_L^{\alpha\,\mathrm{av}\,\star}$, since the averaged gas concentration $c_G^{\alpha\,\mathrm{av}\,\star}$ is not constant, but depends on the liquid averaged concentration $c_L^{\alpha\,\mathrm{av}\,\star}$.

This study is based on the assumption of mass conservation:

$$\frac{d\rho^{\alpha\,\mathrm{m}\,\star}}{dt^\star} = 0 \tag{E.3}$$

Therefore, the mean density at a certain time level $t^\star$ equals the initial mean density:

$$\rho^{\alpha\,\mathrm{m}\,\star}(t^\star) = \rho^{\alpha\,\mathrm{m}\,\star}(0), \tag{E.4}$$

where, according to relation (3.26), the mean densities at time level $t^\star$ and $t^\star = 0$ for a system containing initially the species only in the dispersed phase are:

$$\rho^{\alpha\,\mathrm{m}\,\star}(t^\star) = \varepsilon \rho_G^{\alpha\,\mathrm{m}\,\star}(t^\star) + (1 - \varepsilon)\rho_L^{\alpha\,\mathrm{m}\,\star}(t^\star) \qquad \rho^{\alpha\,\mathrm{m}\,\star}(0) = \varepsilon \rho_G^{\alpha\,\mathrm{m}\,\star}(0), \tag{E.5}$$

where $\rho_G^{\alpha\,\mathrm{m}\,\star}(0)$ is a constant. Since the fluids are considered incompressible, the averaged densities are equal to the mean densities:

$$\rho_G^{\alpha\,\mathrm{av}\,\star} = \frac{\sum_i^{\mathrm{NC}_G} \rho_G^{\alpha\,\mathrm{m}\,\star}}{\mathrm{NC}_G} = \rho_G^{\alpha\,\mathrm{m}\,\star} \qquad \rho_L^{\alpha\,\mathrm{av}\,\star} = \frac{\sum_i^{\mathrm{NC}_L} \rho_L^{\alpha\,\mathrm{m}\,\star}}{\mathrm{NC}_L} = \rho_L^{\alpha\,\mathrm{m}\,\star} \tag{E.6}$$

Based on relations (E.4),(E.5) and (E.6) it can be written that:

$$\varepsilon \rho_G^{\alpha\,\mathrm{av}\,\star}(t^\star) + (1-\varepsilon)\rho_L^{\alpha\,\mathrm{av}\,\star}(t^\star) = \varepsilon \rho_G^{\alpha\,\mathrm{av}\,\star}(0) \tag{E.7}$$

Dividing the above equation with the molecular weight M^α one obtains the following relation:

$$\varepsilon \frac{c_G^{\alpha\,\mathrm{av}\,\star}(t^\star)}{H^\alpha} + (1-\varepsilon)c_L^{\alpha\,\mathrm{av}\,\star}(t^\star) = \varepsilon \frac{c_G^{\alpha\,\mathrm{av}\,\star}(0)}{H^\alpha} \tag{E.8}$$

Therefore, the averaged gas concentration can be obtained as:

$$\frac{c_G^{\alpha\,\mathrm{av}\,\star}(t^\star)}{H^\alpha} = \frac{c_G^{\alpha\,\mathrm{av}\,\star}(0)}{H^\alpha} - \frac{1-\varepsilon}{\varepsilon}c_L^{\alpha\,\mathrm{av}\,\star}(t^\star) \tag{E.9}$$

Introducing relation (E.9) in (E.2), rearranging the terms and considering the mass transfer coefficient and the interfacial area concentration $V^\star/A^\star$ to be constant between two time steps, one can integrate (E.2) as follows:

$$\int_{c^{\alpha\,\mathrm{av}\,\star}(t^\star-\Delta t^\star)}^{c^{\alpha\,\mathrm{av}\,\star}(t^\star)} \frac{1}{\dfrac{c_G^{\alpha\,\mathrm{av}\,\star}(0)}{H^\alpha} - \dfrac{1}{\varepsilon}c_L^{\alpha\,\mathrm{av}\,\star}} \mathrm{d}c_L^{\alpha\,\mathrm{av}\,\star} = k_L^{\alpha\,\star} \frac{A^\star}{V^\star} \int_{t^\star-\Delta t^\star}^{t} \mathrm{d}t^\star \tag{E.10}$$

Performing the integration leads to the following expression of the mass transfer coefficient:

$$\begin{aligned}
k_L^{\alpha\,\star} &= -\frac{V^\star}{A^\star}\frac{\varepsilon}{\Delta t^\star}\ln\frac{\dfrac{c^{\alpha\,\mathrm{av}\,\star}(0)}{H^\alpha} - \dfrac{1}{\varepsilon}c_L^{\alpha\,\mathrm{av}\,\star}(t^\star)}{\dfrac{c^{\alpha\,\mathrm{av}\,\star}(0)}{H^\alpha} - \dfrac{1}{\varepsilon}c_L^{\alpha\,\mathrm{av}\,\star}(t^\star-\Delta t^\star)} \\[2ex]
&= \frac{V^\star}{A^\star}\frac{\varepsilon}{\Delta t^\star}\ln\frac{\dfrac{c_G^{\alpha\,\mathrm{av}\,\star}(t^\star-\Delta t^\star)}{H^\alpha} - c_L^{\alpha\,\mathrm{av}\,\star}(t^\star-\Delta t^\star)}{\dfrac{c_G^{\alpha\,\mathrm{av}\,\star}(t^\star)}{H^\alpha} - c_L^{\alpha\,\mathrm{av}\,\star}(t^\star)}
\end{aligned} \tag{E.11}$$

Acknowledgements

LEBENSLAUF

Persönliche Daten

Name und Vorname:	Onea, Alexandru Aurelian
Geburtsdatum, -ort:	24. Juni 1977, Bukarest, Rumänien
Familienstand:	Verheiratet
Anschrift:	Karlstr. 93, 76317 Karlsruhe
Telefon:	07247-82-2949
E-mail:	onea@irs.fzk.de
Staatsangehörigkeit:	Rumänisch

Schulausbildung

1993-1996:	Mittelschule für Informatik Nr.1, Bukarest, Rumänien Abschluss: Abitur (9.62 von maximal 10)
1996-2001:	Technische Universität "Politehnica" Bukarest, Fakultät für Luft-und Raumfahrttechnik, Abteilung Antriebssysteme, Abschluss: Diplom-Ingenieur Diplomprüfung: 10 von maximal 10 Gesamtnote der Studienjahre: 9.16 von maximal 10
2001-2002:	Technische Universität "Politehnica" Bukarest, Fakultät für Luft-und Raumfahrttechnik, Vertiefungsstudium in der Abteilung für Antriebssysteme, Dissertationsprüfung: 10 von maximal 10 Gesamtnote: 9.50 von maximal 10
2003-2006:	Fakultät für Maschinenbau der Universität Karlsruhe (TH) Institut für Reaktorsicherheit, Forschungszentrum Karlsruhe Wissenschaftlicher Mithilfe - Doktorand

Berufstätigkeit

02.2006-07.2006:	Wissenschaftlicher Mitarbeiter Institut für Reaktorsicherheit, Forschungszentrum Karlsruhe
ab 11.2006:	Wissenschaftlicher Mitarbeiter Institut für Reaktorsicherheit, Forschungszentrum Karlsruhe
Sprachen	Rumänisch (Muttersprache), Englisch (sehr gut), Deutsch (gut), Französisch (Grundkenntnisse)